Defense Threat Reduction Agency
8725 John J. Kingman Road, MS
6201 Fort Belvoir, VA 22060-6201

DTRA-TR-19-3

TECHNICAL REPORT

Fragmentation of Solid Materials Using Shock Tubes. Part 3: Second Test Series in a Small Diameter Shock Tube

October 2018

HDTRA1-14-C-0001

Bryan Bewick et al.

Prepared by:
Protection Engineering Consultants
P.O. Box 781607
San Antonio, TX 78278

DESTRUCTION NOTICE:

Destroy this report when it is no longer needed.
Do not return to sender.

PLEASE NOTIFY THE DEFENSE THREAT REDUCTION AGENCY, ATTN: DTRIAC/RD-NTF, 8725 JOHN J. KINGMAN ROAD, MS-6201, FORT BELVOIR, VA 22060-6201, IF YOUR ADDRESS IS INCORRECT, IF YOU WISH THAT IT BE DELETED FROM THE DISTRIBUTION LIST, OR IF THE ADDRESSEE IS NO LONGER EMPLOYED BY YOUR ORGANIZATION.

REPORT DOCUMENTATION PAGE

Form Approved
OMB No. 0704-0188

1. REPORT DATE *(DD-MM-YYYY)*	2. REPORT TYPE	3. DATES COVERED *(From - To)*
00-10-2018	Technical	

4. TITLE AND SUBTITLE
Fragmentation of Solid Materials Using Shock Tubes. Part 3: Second Test Series in a Small Diameter Shock Tube.

5a. CONTRACT NUMBER
HDTRA1-14-C-0001

5b. GRANT NUMBER

5c. PROGRAM ELEMENT NUMBER

6. AUTHOR(S)
Bryan Bewick (a), Greg Rolater (a), Kirk Marchand (a), Adam Ziemba (b), Mohsen Sanai (b), and Culbert B. Laney (c)

5d. PROJECT NUMBER

5e. TASK NUMBER

5f. WORK UNIT NUMBER

7. PERFORMING ORGANIZATION NAME(S) AND ADDRESS(ES)
(a) Protection Engineering Consultants (PEC), PO Box 781607, San Antonio, TX 78278
(b) SRI International, 333 Ravenswood Ave., Menlo Park, CA 94025
(c) Engility Corporation, 8211 Terminal Road, Suite 1000, Lorton, VA 22079

8. PERFORMING ORGANIZATION REPORT NUMBER

9. SPONSORING / MONITORING AGENCY NAME(S) AND ADDRESS(ES)
Defense Threat Reduction Agency (DTRA)
8725 John J. Kingman Road, STOP 6201
Fort Belvoir, VA 22060

10. SPONSOR/MONITOR'S ACRONYM(S)
DTRA

11. SPONSOR/MONITOR'S REPORT NUMBER(S)
DTRA-TR-19-3

12. DISTRIBUTION / AVAILABILITY STATEMENT
Distribution Statement A. Approved for public release; distribution is unlimited.

13. SUPPLEMENTARY NOTES

14. ABSTRACT
This report describes a series of tests that used an explosively-driven small-diameter shock tube to shatter simply-supported plates with relatively high-pressure, long-duration blast loads. To determine how the fragment size distribution changed with time due to, e.g., collisions between fragments, the fragment size distribution was measured at two different times. These tests varied the load, sample material, sample thickness, sample strength, and the volumetric density of fragments impinging on the collection device. As a result, these tests obtained a range of different fragment size distributions. By contrast, an earlier test series with fewer variables obtained only a single fragment size distribution.

15. SUBJECT TERMS
fragmentation, size distributions, Weibull distributions, shock tubes

16. SECURITY CLASSIFICATION OF:			17. LIMITATION OF ABSTRACT	18. NUMBER OF PAGES	19a. NAME OF RESPONSIBLE PERSON
a. REPORT	b. ABSTRACT	c. THIS PAGE			MAJ David Matters
Unclassified	Unclassified	Unclassified	UU	73	19b. TELEPHONE NUMBER *(include area code)* 571-616-5217

UNIT CONVERSION TABLE

U.S. customary units to and from international units of measurement*

U.S. Customary Units	Multiply by → / ← Divide by†		International Units
Length/Area/Volume			
inch (in)	2.54	$\times 10^{-2}$	meter (m)
foot (ft)	3.048	$\times 10^{-1}$	meter (m)
yard (yd)	9.144	$\times 10^{-1}$	meter (m)
mile (mi, international)	1.609 344	$\times 10^{3}$	meter (m)
mile (nmi, nautical, U.S.)	1.852	$\times 10^{3}$	meter (m)
barn (b)	1	$\times 10^{-28}$	square meter (m^2)
gallon (gal, U.S. liquid)	3.785 412	$\times 10^{-3}$	cubic meter (m^3)
cubic foot (ft^3)	2.831 685	$\times 10^{-2}$	cubic meter (m^3)
Mass/Density			
pound (lb)	4.535 924	$\times 10^{-1}$	kilogram (kg)
unified atomic mass unit (amu)	1.660 539	$\times 10^{-27}$	kilogram (kg)
pound-mass per cubic foot (lb ft^{-3})	1.601 846	$\times 10^{1}$	kilogram per cubic meter (kg m^{-3})
pound-force (lbf avoirdupois)	4.448 222		newton (N)
Energy/Work/Power			
electron volt (eV)	1.602 177	$\times 10^{-19}$	joule (J)
erg	1	$\times 10^{-7}$	joule (J)
kiloton (kt) (TNT equivalent)	4.184	$\times 10^{12}$	joule (J)
British thermal unit (Btu) (thermochemical)	1.054 350	$\times 10^{3}$	joule (J)
foot-pound-force (ft lbf)	1.355 818		joule (J)
calorie (cal) (thermochemical)	4.184		joule (J)
Pressure			
atmosphere (atm)	1.013 250	$\times 10^{5}$	pascal (Pa)
pound force per square inch (psi)	6.984 757	$\times 10^{3}$	pascal (Pa)
Temperature			
degree Fahrenheit (^oF)	$[T(^oF) - 32]/1.8$		degree Celsius (^oC)
degree Fahrenheit (^oF)	$[T(^oF) + 459.67]/1.8$		kelvin (K)
Radiation			
curie (Ci) [activity of radionuclides]	3.7	$\times 10^{10}$	per second (s^{-1}) [becquerel (Bq)]
roentgen (R) [air exposure]	2.579 760	$\times 10^{-4}$	coulomb per kilogram (C kg^{-1})
rad [absorbed dose]	1	$\times 10^{-2}$	joule per kilogram (J kg^{-1}) [gray (Gy)]
rem [equivalent and effective dose]	1	$\times 10^{-2}$	joule per kilogram (J kg^{-1}) [sievert (Sv)]

*Specific details regarding the implementation of SI units may be viewed at http://www.bipm.org/en/si/.

†Multiply the U.S. customary unit by the factor to get the international unit. Divide the international unit by the factor to get the U.S. customary unit.

EXECUTIVE SUMMARY

The report describes the third of four test series designed to help develop a probabilistic, physics-based model for the fragmentation of building components subjected to airblast. Similar to the first series, this test series used a small-diameter, explosively-driven shock tube to shatter simply-supported plates made of glass, concrete, and masonry.

Prior to this work, shock tubes were rarely, if ever, used to study fragmentation. When driven by extended cylindrical explosive charges, shock tubes can achieve relatively large, steady, and uniform loads, typical of certain real-world events.

The main limitation of shock tubes is a tradeoff between overpressure, size, and duration (steadiness). Like the first test series, this third test series favors high overpressures, while the second and fourth test series favor size and duration. Placing test articles inside small shock tubes risks ejecting the test articles whole, almost regardless of support technique, rather than fragmenting them. This test series used a novel 'punch out' technique, wherein the test article was mounted outside the shock tube. The test articles were made deliberately larger than the shock tube diameter, to allow for a simple support structure.

This test series focused on four main effects: loading, strength, thickness, and volumetric density of fragments. In terms of loading, this test series imposed peak static reflected overpressures of up to 2,000 psi on glass (four times higher than in the first test series), 4,600 psi on concrete (50% higher than in the first test series), and 4,400 psi on CMU (15% higher than in the first test series). These peak pressures were the upper limit of that the shock tube could support. In terms of strength, this test series compared tempered and annealed glass. The first tests series studied only tempered glass. In terms of thickness, this test series compared 1-in vs. 2-in-thick specimens of precast concrete and 1.5-in vs. 2-in-thick specimens of CMU. The first test series studied only 2-in-thick specimens of precast concrete and CMU. In terms volumetric density, this test series eliminated the fragment stripper used in the first test series, which increased the number and mass of physically collected fragments by factors of 5 to 15, which substantially increased both the number of off-axis fragments and the number of shattering collisions between fragments

The tests were performed in SRI's 6.5-in-diameter 37-ft long shock tube. The test specimens were 16-in. x 16-in. squares of tempered and annealed glass (¼-in.-thick), precast concrete (1-in. or 2-in.-thick), and concrete masonry unit (CMU) material (1.5-in. or 2-in.-thick). The glass specimens were subjected to three pressure-histories with peak reflected static overpressures ranging from approximately 250-psi to 2,500-psi. The precast concrete and CMU were subjected to three different pressure-histories with peak reflected static overpressures ranging from approximately 500-psi to 4,500-psi.

Two measurement techniques were used to characterize the fragment size distribution. First, in the glass tests, a rear-view high speed video (HSV) camera was used to capture the initial fragment size distribution. Second, in all of the tests, the fragments were physically collected with soft-catch device and analyzed. Because this test series collected over 50,000 fragments, it was not possible to measure the fragments by hand. Instead, a new technique was used, which combines sieving, shadowgraphy, and digital image processing.

Contents

Figures

Tables

1 BACKGROUND

This report is the third in a four part series:

- Part 1 / Test Series 1. Measured fragment size distributions, velocity size distributions, and the time-dependency of fragment size distributions in a large number of different small-scale tests involving glass, concrete, and concrete masonry unit (CMU) test articles [1]. The first test series included a fragment stripper that confined fragments to a single focal plane. This allowed for measurements of mid-air fragment size and velocities using a single side-view camera. However, it dramatically reduced the number of fragments captured in a soft-catch collection device; thus the fragment stripper was removed from all subsequent tests.
- Part 2 / Test Series 2. Measured fragment size distributions in a small number of different large-scale tests involving plate glass windows, concrete panels, and CMU walls. These tests showed that, for plate glass and perhaps other materials, the size distributions obtained at small scales in Part 1 also occur at large scales [2].
- Part 3 / Test Series 3 *(this report)*. Measured fragment size distributions in a large number of different small-scale tests involving glass, concrete, and CMU test articles. Compared to the first test series, the third test series explored a wider range of loads, sample strengths, and sample thicknesses. In addition, because the fragment stripper was removed, the third test series captured a much large number of fragments in the soft-catch collection device. The soft-catch collection device had to be redesigned to survive the high overpressures used in this test series.
- Part 4 / Test Series 4. Measured fragment size distributions in a small number of different large-scale tests involving brick walls, concrete panels, and clay tile roofs. Building on Part 2, this test series provided further evidence that the size distributions obtained at small scales in Parts 1 and 3 may also occur at large scales.

All of these tests used explosively-driven shock tubes. Shock tubes have rarely, if ever, been used to systematically study fragmentation prior to this work. When driven by extended cylindrical explosive charges, shock tubes can achieve relatively large, steady, and uniform loads, typical of certain real-world events. By contrast, open-air compact high-explosive charges tend to produce rapidly-decaying non-uniform loads.

The main limitation of shock tubes is a tradeoff between overpressure, size, and duration. The first and third series favored high overpressures, while the second and fourth test series favored size and duration. More specifically, Test Series 1 and 3 used a small (6.5-in diameter) shock tube to load square plates with relatively short-duration high-overpressure airblast, creating conditions where material properties (e.g., strength, density) dominate structural response (e.g., bending, flexing). By contrast, Test Series 2 and 4 used a large (8-ft. diameter) shock tube to load realistic building façade panels and roofing sections with relatively long-duration low-overpressure air blast, creating conditions where structural response and material properties both contribute to fragmentation.

1.1 PURPOSE AND SCOPE

This third test series is a continuation of the first test series [1]. Both Test Series 1 and 3 were performed in SRI International's 6.5-in-diameter 37-ft long shock tube, where the effects of material type were studied by comparing test articles composed of glass, precast concrete, and concrete masonry unit (CMU). Placing test articles inside small shock tubes risks ejecting them whole, almost regardless of support technique, rather than fragmenting them. Thus Test Series 1 and 3 used a novel 'punch out' technique, wherein the test article was mounted outside the shock tube. The test articles were made deliberately larger than the shock tube exit diameter, to allow for a simple support structure.

The fragment size distribution was measured at three different times using three different techniques. More specifically, a high-speed video (HSV) camera was used to record the initial crack pattern on the rear face of each sample, a second HSV camera was used to capture the fragment sizes and velocities in-flight at intermediate times, and, finally, the late-time at-rest fragments were physically collected and analyzed post-test.

Test Series 1 and 3 differed in the following ways:

- Loading. Test Series 3 used the maximum possible loads that the shock tube could produce. More specifically:
    - Glass. Test Series 1 studied peak reflected static overpressures of ~250 to 500 psi while Test Series 3 studied peak static overpressures of ~250 to 2,500 psi.
    - Concrete. Test Series 1 studied peak reflected static overpressures of ~1,500 to 3,000 psi while Test Series 3 studied peak static overpressures of ~500 to 4,500 psi.
    - CMU. Test Series 1 studied peak reflected static overpressures of ~1,200 to 3,600 psi while Test Series 3 studied peak static overpressures of ~600 to 4,200 psi.
- Sample strength. Test Series 1 studied tempered glass. Test Series 3 studied both tempered and annealed glass. Tempered glass is approximately four times stronger than annealed glass.
- Sample thickness.
    - Test Series 1 studied only 2-in-thick specimens of precast concrete. By contrast, Tests Series 3 studied both 1-in- and 2-in-thick specimens of precast concrete.
    - Test Series 1 studied only 2-in-thick specimens of CMU. By contrast, Test Series 3 studied both 1.5-in and 2-in-thick specimens of CMU.
- Number, mass, and volumetric density of fragments.

The higher loadings used in the third test series required two significant changes to the test setup. First, Test Series 1 used a moderate-duty soft-catch fragment capture system involving layers of Kevlar and carpet, while Test Series 3 used this plus a new heavy-duty soft-catch capture system involving layers of Kevlar, heavy-duty tarp, and rubber mounted on a stronger frame and located farther away from the shock tube exit.

Second, in Test Series 1, a fragment stripper was used to ensure that the fragments captured using a side-view high-speed video (HSV) camera were confined to a single focal plane at a known fixed distance from the camera, so that fragment masses and velocities could be accurately estimated. Unfortunately, due to the limited resolution of the HSV cameras employed, only the largest fragments were visible. The higher loads used in Test Series 3 resulted in even smaller fragments, further reducing the number of visible fragments in the rear-view HSV. To increase the number of visible fragments, the fragment stripper was not used in Test Series 3.

In Test Series 1, the fragment stripper preferentially selected fragments originating on or near the uniformly-loaded circular portion of the target directly in contact with the shock tube exit. By contrast, in Test Series 3, with the fragment stripper removed, the results included more of the slow late-forming fragments from the perimeter of the sample. In other words, while the first test series tended to capture fragments formed under identical steady uniform conditions, the third test series captured a greater diversity of fragments formed under varying unsteady non-uniform conditions.

1.2 TEST OVERVIEW

Table 1 summarizes the 18 tests conducted during Test Series 3. Tests 22 to 28 were conducted in May 2015 with a moderate-duty soft-catch fragment collection system. The original fragment collection system was heavily damaged in Test 25. Various alternative designs for the fragment collection system were used in Tests 26, 27, and 28. No data was collected in these tests and thus they are omitted from Table 1. Tests 29 to 39 where conducted in June 2015 with a redesigned heavy-duty soft-catch fragment collection system. Notice that Tests 1 to 16 took place in Test Series 1 [1] while Tests 17 to 21 took place in the Test Series 2 [2].

Table 1. Small diameter shock tube experiment parameters.

Test	Sample	Sample Thickness[1] (in)	Sample Weight[1] (lb)	Charge Type	Charge Length (in)	Charge Mass (g)	Peak Reflected Overpressure (psi)		Approximate Duration (ms)		Impulse (psi-ms)	
							East[2]	West[2]	East[2]	West[2]	East[2]	West[2]
22	Tempered glass	0.25	5.15	4x200 gr/ft Primacord	24	104.4	226	220	12	12	395	394
23	Tempered glass	0.25	5.15	7x200 gr/ft Primacord	24	181.6	416	398	12	12	648	633
24	Tempered glass	0.25	5.15	7x200 gr/ft Primacord	24	181.6	441	439	12	12	634	626
25	Tempered glass	0.25	5.15	6 Unigel; 2x200 gr/ft Primacord	24	3178	2492	2392	20	20	5326	5800
29	Concrete	2.0	40.95	8x200 gr/ft Primacord	24	208.8	553	530	15	15	1112	1093
30	Concrete	2.0	42.25	8x200 gr/ft Primacord	24	208.8	528	534	15	15	1103	1091
31	CMU	2.0	38.15	8x200 gr/ft Primacord	24	208.8	550	564	15	15	1083	1074
32	CMU	2.0	36.4	8x200 gr/ft Primacord	24	208.8	575	598	15	15	1123	1109
33	Annealed glass	0.226	5.3	7x200 gr/ft Primacord	24	181.6	434	436	13	13	687	660
34	Annealed glass	0.233	5.3	7x200 gr/ft Primacord	24	181.6	427	415	13	13	710	672
35	CMU	1.5	28.2	6 Unigel; 2x400 gr/ft Primacord	24	3178	4115	4012	18	18	7255	7877
36	Concrete	0.99	21.05	6 Unigel; 2x400 gr/ft Primacord	24	3178	3955	3756	18	18	7583	7292
37	CMU	1.5	27.9	6 Unigel; 2x400 gr/ft Primacord	24	3178	3918	4378	16	16	7200	7100
38	Concrete	1.0	21.65	6 Unigel; 2x400 gr/ft Primacord	24	3178	4354	4571	16	16	6500	7000
39	Tempered Glass	0.25	5.1	6 Unigel; 2x400 gr/ft Primacord	24	3178	1979	1822	20	20	5720	5860

[1] All test sample were 16-in x 16-in plates with varying thickness
[2] Gages located 1.5-in from the samples inside the shock tube on the East or West

1.3 TEST SAMPLES

Table 2 shows the material properties of the test sample. The compressive strengths of concrete and CMU were measured specifically for this test series. The other properties were not specifically measured but are typical; see, e.g., [3].

Table 2. Test sample material properties.

Material Type	Density (pcf)	Compressive Strength (psi)	Elastic Modulus (psi)	Tensile Strength (psi)	G_f (lbs/in)
FT Glass	161	13,500	10.0×10^6	13,500	0.047
AN Glass	161	3,380	10.0×10^6	3,380	0.047
Concrete	145	4,820	4.00×10^6	521	0.43
CMU	130	3,830	3.03×10^6	464	0.35

The glass samples, both fully tempered (FT) and annealed (AN), were off-the-shelf single panes produced by C.R. Laurence, CO. and cut to size by a local glass shop in Livermore, CA [4]. Table 2 assumes that annealed glass has exactly 25% of the compressive and tensile strengths of fully-tempered glass.

The concrete samples were produced by a local concrete contractor. While they supposedly used a standard 3,500-psi mix, the concrete samples actually obtained a substantially higher compressive strength of 4,820-psi; see Appendix B. By comparison, similar concrete samples produced for the first test series obtained a compressive strength of 3,120-psi, more in line with expectations [1].

The CMU samples were also produced by a local contractor, Pacific Supply. Using an off-the-shelf 3,000-psi masonry mix, the CMU material samples obtained a compressive strength of 3,830-psi; see Appendix B.

1.4 TEST SETUP

1.4.1 HIGH-PRESSURE SHOCK TUBE

Figure 1 shows the High-Pressure Shock Tube (HPST) located at SRI's privately-owned Corral Hollow Experiment Site (CHES). The HPST was constructed from multiple sections of 6.5-in.-diameter, 1-in.-thick steel pipe, totaling 37-ft in length.

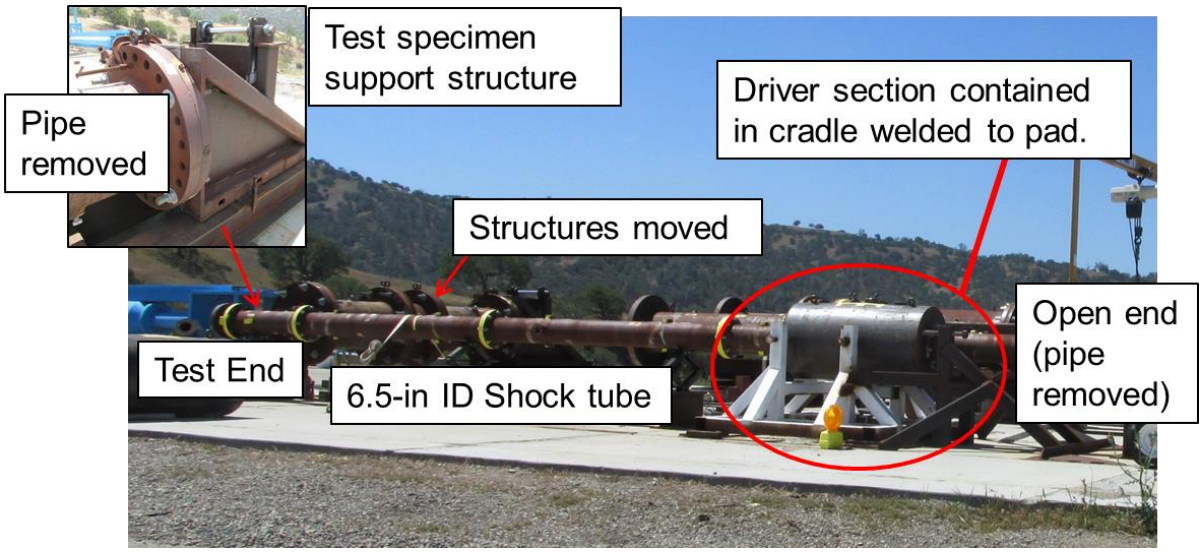

Figure 1. High-Pressure Shock Tube (HPST) located at SRI's Corral Hollow Experiment Site.

The HPST was attached to a 3-ft-long, 4-in.-thick driver section. Figure 2 shows the explosives used in the driver section. For the lower-pressure shots (<1,000 psi), the HPST was driven by multiple 2-ft-long strands of Primacord. For the higher-pressure shots (>1,000-psi), the HPST was driven by six 2-in.-diameter by 8-in.-long packets of Unigel taped onto two 2-ft-long Primacord strands and side-detonated with Primacord. In either case, the driver charges were placed on a foam sheet and centered in the driver-section of the shock tube.

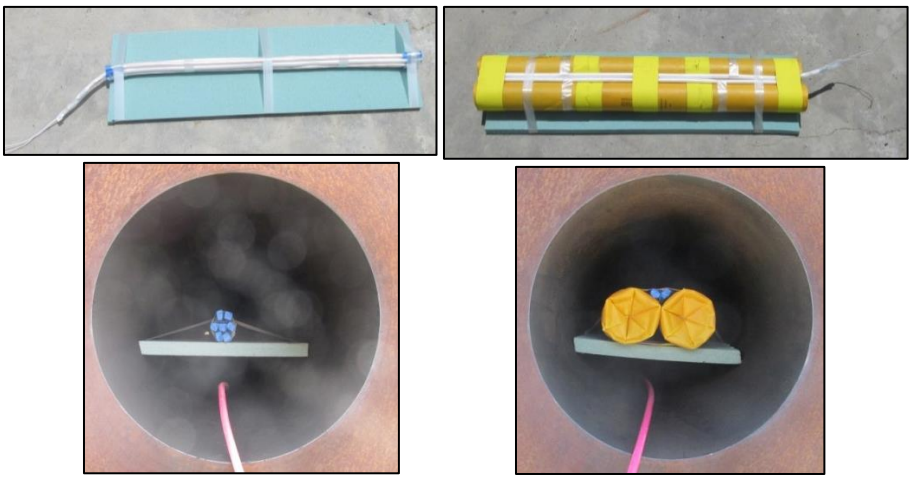

(a) Primacord driver (low-pressure) (b) Unigel driver (high pressure)

Figure 2. High-explosives shock tube drivers for (a.) low pressure tests and (b.) high pressure tests.

Figure 3 shows the exit end of the HPST including the support structure for the test specimens. Like the rest of the shock tube, the exit was 6.5-in diameter. The test samples were flush-mounted on a shelf and centered on the shock tube exit. The rear of the samples was simply supported by a 2-in.-thick steel plate with a 14-in.-diameter hole. Figure 4 shows three rear views of as-mounted test samples.

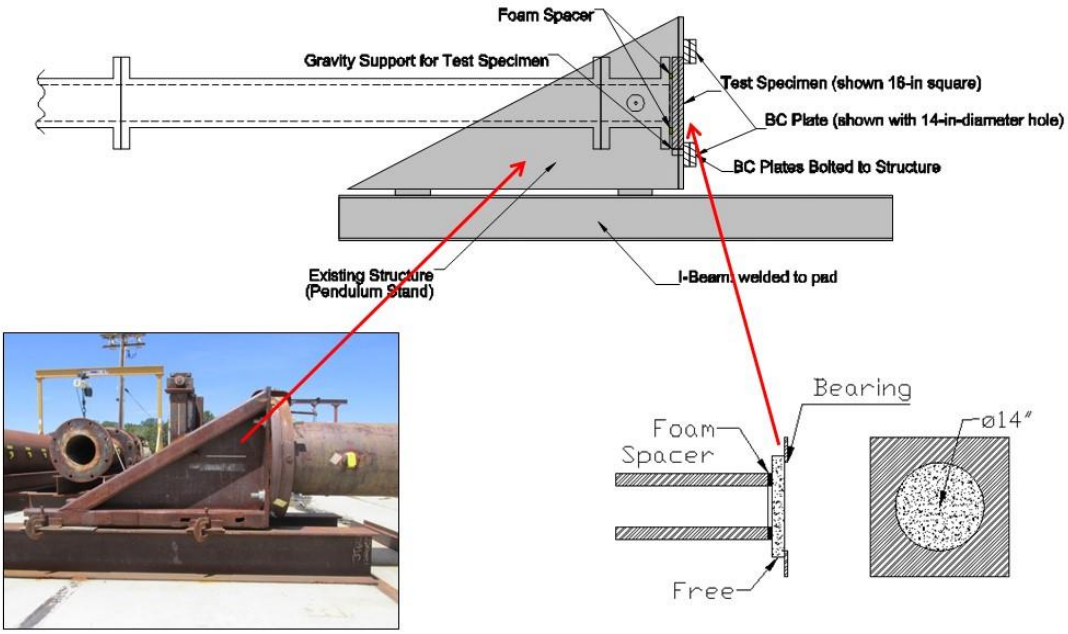

Figure 3. Exit end of the HPST including the support structure for the test specimens.

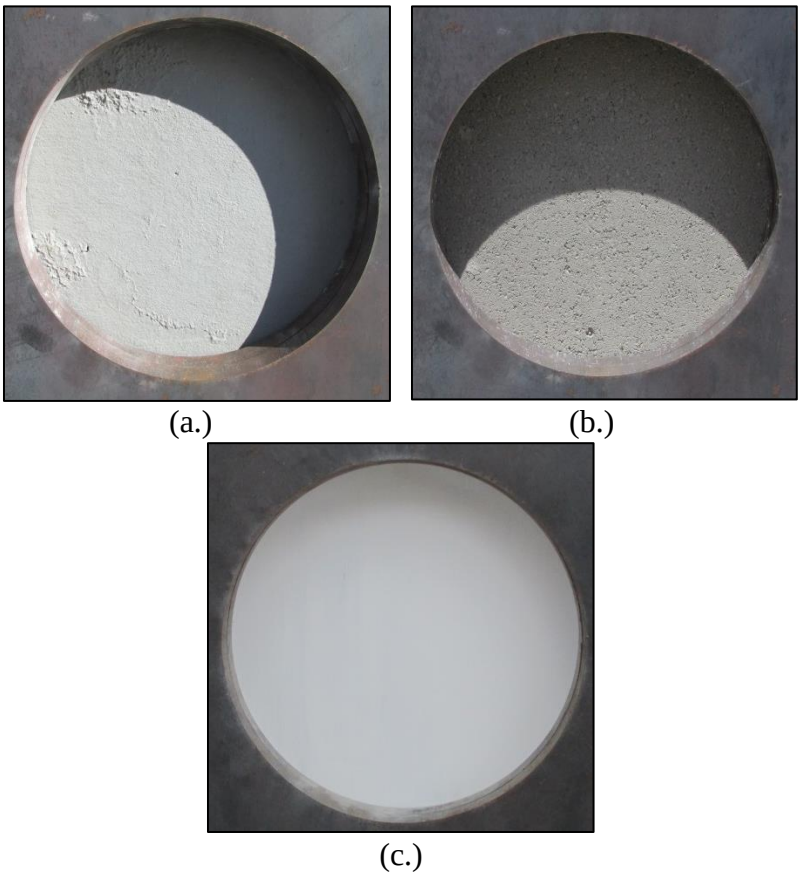

(a) Concrete sample (b) CMU sample (c) Glass sample

Figure 4. Rear view of as-mounted test samples.

1.4.2 Pressure Gages

Four Kulite strain-gaged-diaphragm pressure transducers were installed inside the shock tube to measure pressure-histories of the shock wave as it traveled toward the test specimen. More specifically, one gage was located 192 in., one gage was located 56 in., and two gages were located 3.25 in. from the leading edge of the test specimen. The latter two gages, designated P1E and P1W, were located on opposite sides of the shock tube and placed as close to the test specimen as the shock tube geometry allowed. The Kulite strain-gaged-diaphragm pressure transducers had 60 ksi maximum pressure range for the higher-pressure shots (>1,000 psi) and a 5 ksi maximum pressure range for the lower-pressure shots (<1,000 psi). Data from the four pressure gages was collected using two high-resolution Nicolet Odyssey digital recording units. One unit was set to record at 10^7 samples/s for 130 ms and the other to record at 10^6 samples/s for 1.3 s. All results were filtered using a 10-kHZ low-pass filter.

1.4.3 Fragment Collection System

Figure 5 shows a photograph of the setup used for Tests 22 to 25 conducted in May 2015. Figure 6 shows a design schematic for the original soft-capture fragment collection system used in Tests 22 to 25.

Figure 5. Photograph of the high-pressure shock tube and the original soft-capture fragment collection system used in Tests 22 to 25 conducted in May 2015.

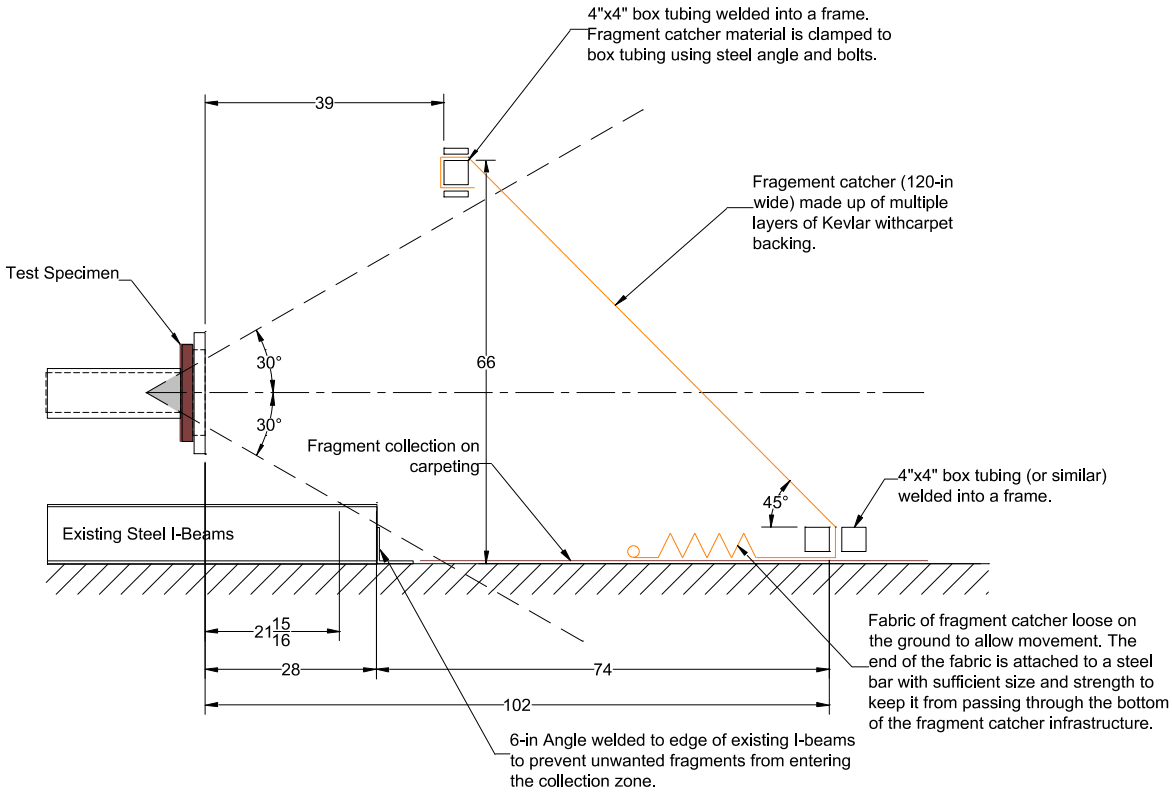

Figure 6. Design schematic for the original soft-capture fragment collection system used in Tests 22 to 25 conducted in May 2015.

Just as in the first test series [1], the original fragment collection system performed well in Tests 22, 23 and 24, where the peak reflected overpressures ranged from 250 to 400psi. However, as seen in Figure 7, the original fragment collection system was heavily damaged in Test 25, where the peak reflected overpressure was approximately 2,250 psi. The failures originated from the three bolts used to attach the Kevlar to the steel frame.

Figure 7. Photograph of damage to the original soft-capture collection system following Test 25.

Immediately following Test 25, three additional Unigel driver tests were done to determine the peak reflected overpressures impinging on 2 ft^3 steel boxes filled with concrete, positioned side-on at distances of 7 ft and 14 ft downstream of the shock tube exit. The 7-ft location represents the position of the original fragment collection system. The 14-ft location represents a possible alternative location for the revised fragment collection system. Figure 8 shows a photograph of the setup used for Tests 26, 27, and 28 conducted in May 2015. Figure 9 shows pressure-histories at the 7-ft and 14-ft locations in Test 28.

Figure 8. Photograph of the high-pressure shock tube and pressure gages mounted on concrete-filled steel blocks used in Test 26, 27, and 28.

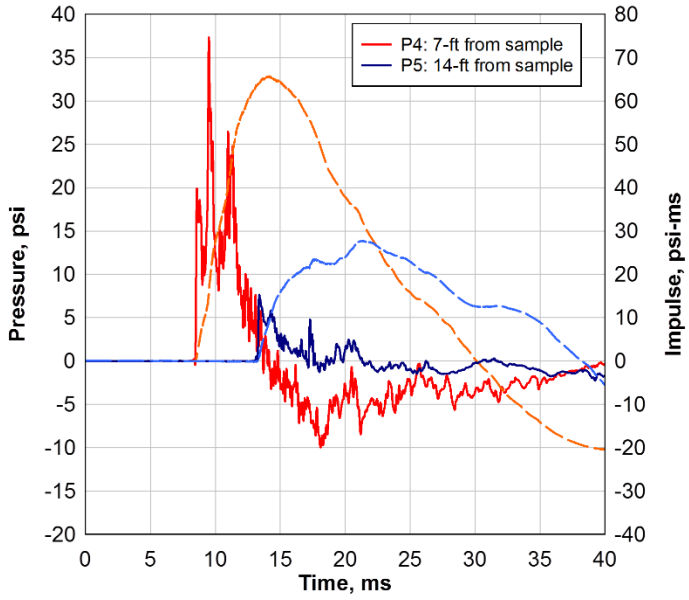

Figure 9. Pressure-histories measured by the pressure gages mounted on concrete-filled steel blocks in Test 28.

As seen in Figure 10, Figure 11, and Figure 12, the fragment collection system was redesigned and relocated based on the results of Tests 22 to 28. The original fragment collection system consisted of layers of Kevlar and carpets mounted on a steel A-frame structure. The new fragment

collection system consisted of layers of Kevlar, heavy-duty canvas tarps (15 oz), and ¼-in.-thick rubber sheets mounted on a steel A-frame structure. Considerably more Kevlar was used in the new fragment collection system than in the old fragment collection system. In addition, the Kevlar was folded over the top bars rather than bolted to the steel A-frame structure. As a result, in the new fragment collection system, the Kevlar would have to rip completely across its width to break free of the frame. By contrast, in the old fragment collection system, the Kevlar could break free by simply detaching from the bolts.

The new fragment collection system was located 5-ft further away from the test sample than the old fragment collection system. To ensure the same subtended angle, a second section was added to the top of the new fragment collection system. More specifically, according to high-speed video (HSV), nearly all of the fragment trajectories lay within a 30 degree cone. The original fragment collection system in the original location obtained full coverage of this 30 degree cone. The new fragment collection system in the new location, but without the second top section, obtained 30 degrees of coverage on the bottom but only 21 degrees of coverage on the sides and top. The new fragment collection system in the new location, with the second top section, obtained a full 30 degrees of coverage of the top and bottom.

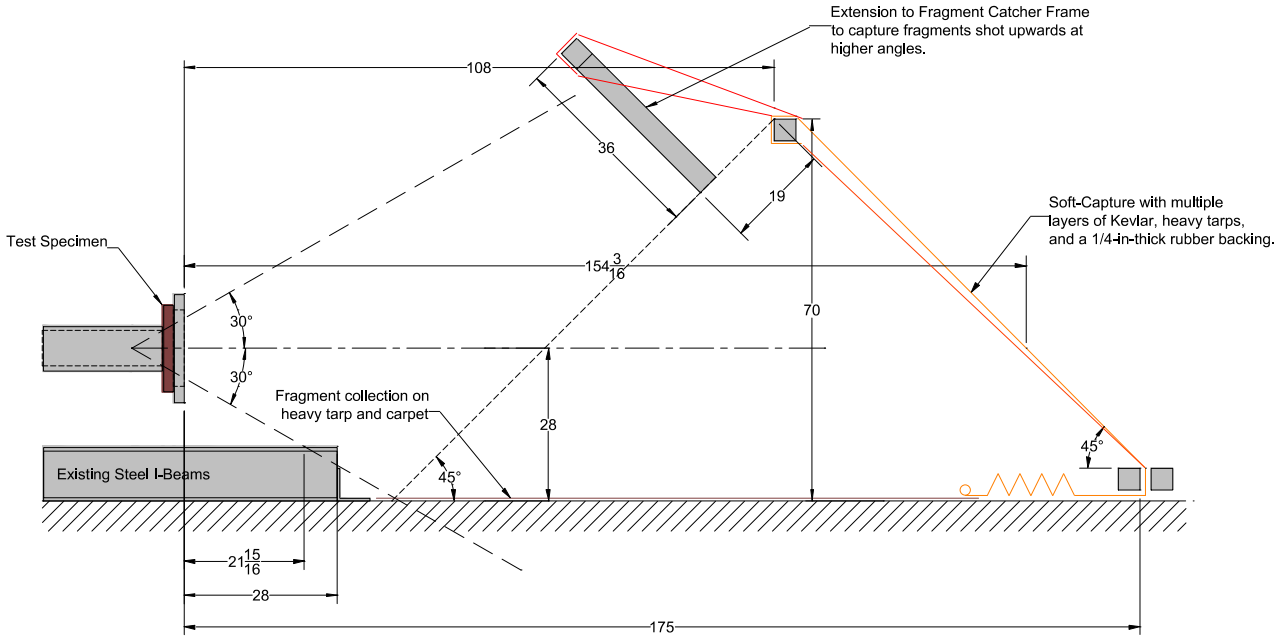

Figure 10. Design schematic for the new soft-capture fragment collection system used in Tests29 to39 conducted in June 2015.

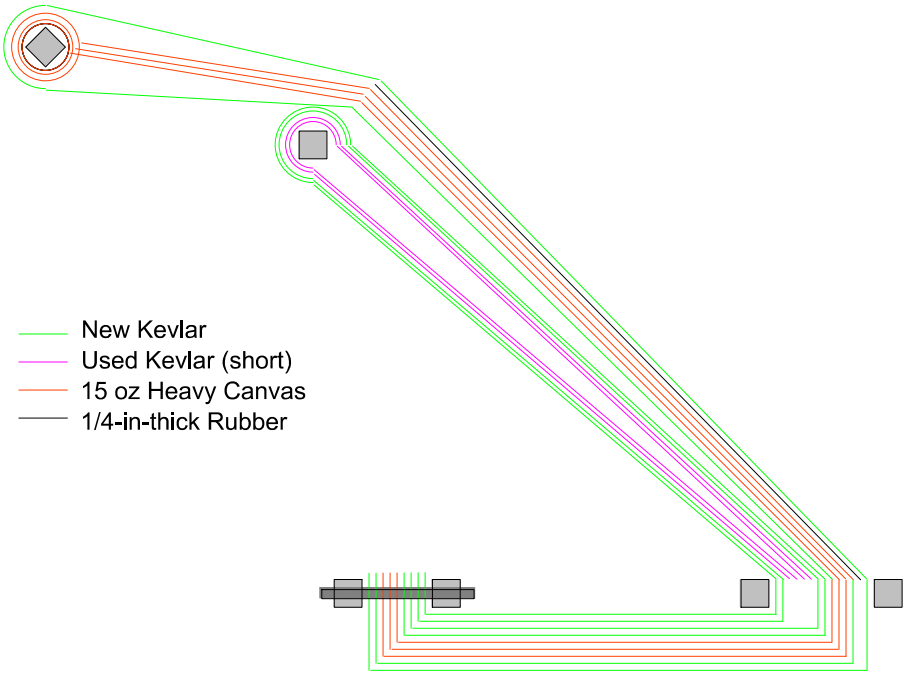

Figure 11. Design schematic for the material layers in the new soft-capture fragment collection system used in Tests29 to 39 conducted in June 2015.

Figure 12. Photograph of the high-pressure shock tube and the new soft-capture fragment collection system used in Tests 29 to 39 conducted in June 2015.

Figure 13 and Figure 14 show the new soft-capture fragment collection system after a low pressure and a high-pressure test, respectively.

Figure 13. Post-test picture of the new soft-capture fragment collection system after a low-pressure test (Test 29)

Figure 14. Post-test picture of new soft-capture fragment collection system after high-pressure test (Test 36).

Prior to each test, the soft-capture fragment collection system and the surrounding pad were cleaned using a leaf blower to remove any debris that had deposited in the area since the prior test.

The soft-capture fabrics were repaired as required and reset to their original positions. After each test, fragments were collected in three separate regions:

- From the soft-capture fragment collection system. More specifically, fragments located on the pad under or in front of the A-frame structure were collected using a broom, while fragments lodged in the soft-capture fabrics were collected using a cleaned-out shop vacuum.
- To the sides of the soft-capture fragment collection system. These fragments were collected using a broom.
- From the steel structure used to support the test sample. These fragments were collected using a cleaned-out shop vacuum. These fragments were analyzed separately from the other fragments.

2 RESULTS OVERVIEW

Figure 15 shows the results from the P1E and P1W gages for a lower-pressure (<1,000-psi) and a higher-pressure (>1,000-psi) test. In this example and in general, the P1E and P1W gages were in good agreement. Thus all subsequent pressure traces in this section show the average of the P1E and P1W gages.

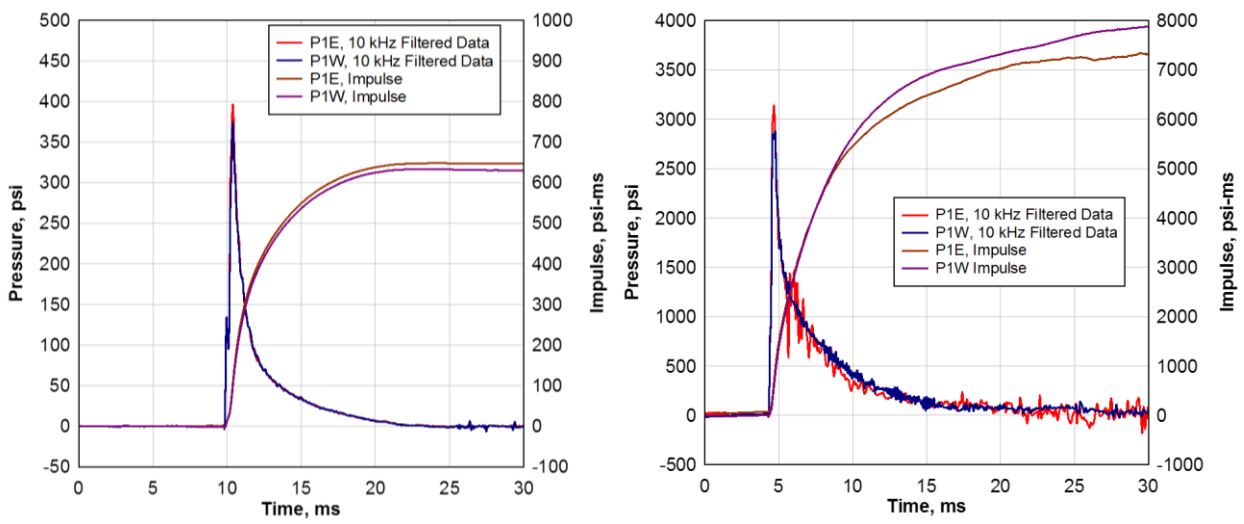

(a) Lower pressure glass test (Test 23). (b) Higher pressure CMU test (Test 35).

Figure 15. Two examples of pressure histories from pressure gages P1E and P1W, which were mounted opposite one another 3.25 in. upstream of test samples.

Figure 16 shows the pressure histories for the five lower-pressure (<1,000 psi) glass tests. Similarly, Figure 17 shows the pressure histories for the four lower-pressure (<1,000 psi) concrete and CMU tests. Figure 18 shows the pressure histories for the two higher-pressure glass tests, the two higher-pressure concrete tests, and the two higher-pressure CMU tests. Finally, Table 3 shows the peak incident static overpressure, peak reflected static overpressure, overpressure duration, and peak reflected impulses based on the results shown in Figure 16, Figure 17, and Figure 18.

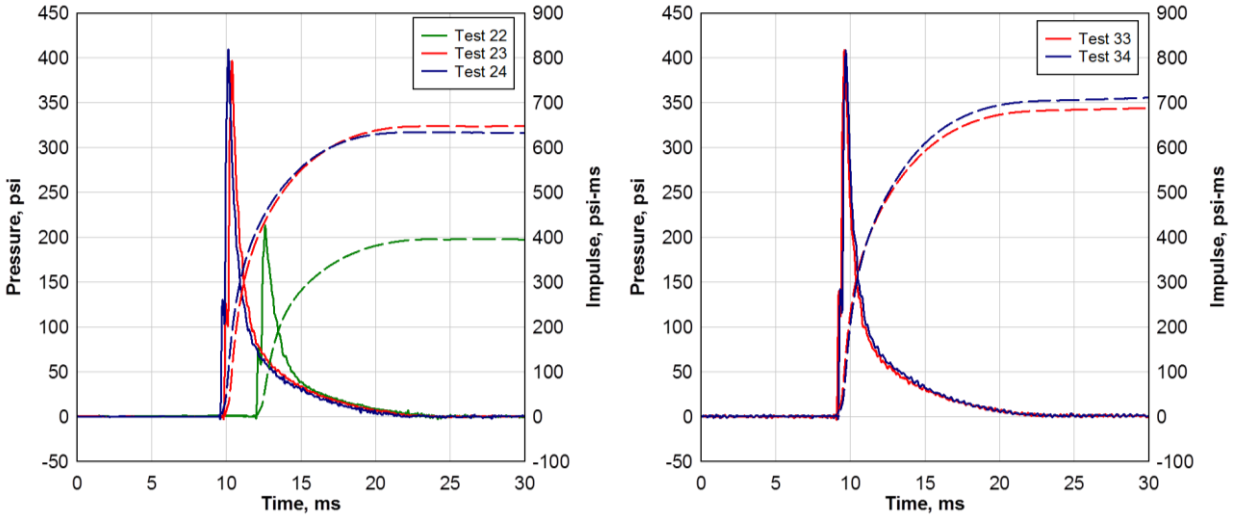

(a) Tempered Glass (b) Annealed Glass

Figure 16. Pressure-histories for five lower-pressure glass tests.

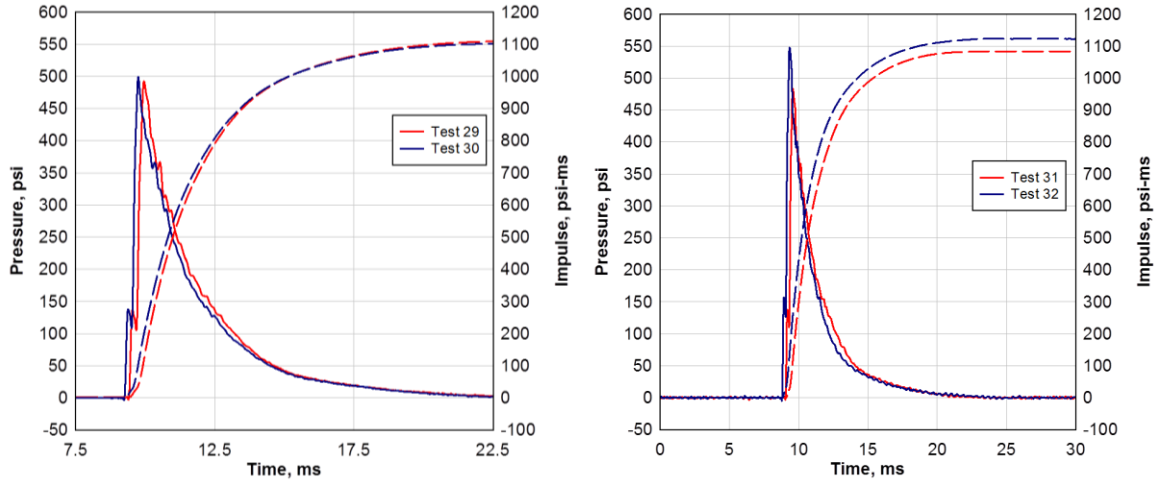

(a) Concrete (b) CMU

Figure 17. Pressure histories for four lower-pressure concrete and CMU tests.

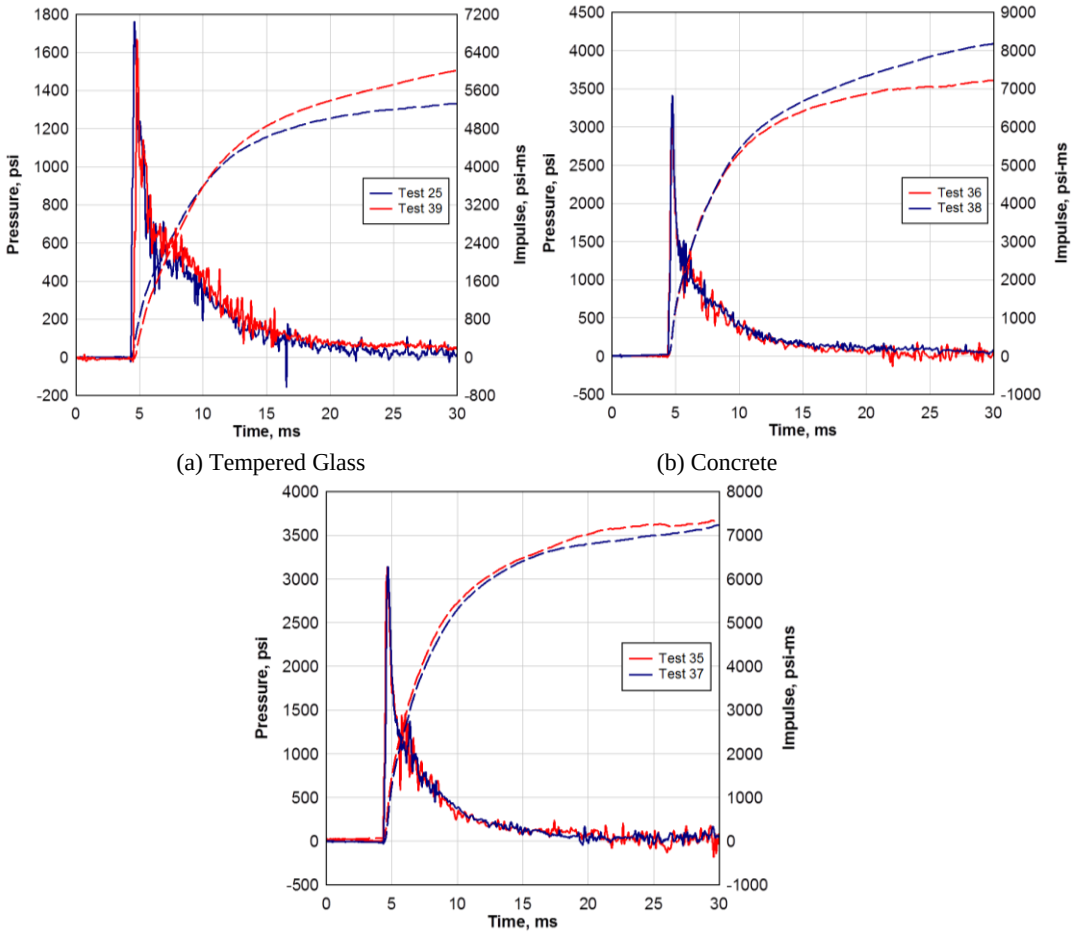

(a) Tempered Glass (b) Concrete

(c) CMU.

Figure 18. Pressure histories for six higher-pressure glass, concrete, and CMU tests.

Table 3. Peak overpressures, durations, and impulses at 3.25 in. up-tube from the leading edge of the test specimen.

Test	Sample	Incident Overpressure (psi)[1]			Reflected Overpressure (psi)[1]			Duration (ms)[1]		Peak Reflected Impulse (psi-ms)[1]		
		East	West	Avg.	East	West	Avg.	East	West	East	West	Avg.
22	Temp. Glass	87	89	88	226	220	223	12	12	395	394	395
23	Temp. Glass	147	154	151	416	398	407	12	12	648	633	641
24	Temp. Glass	158	158	158	441	439	440	12	12	634	626	630
25	Temp. Glass	1524	1780	1652	2492	2392	2442	20	20	5326	5800	5563
26	Prelim CMU	1530	1738	1634	5000	4732	4866	N/A[2]	N/A[2]	N/A[2]	N/A[2]	N/A[2]
27	Prelim CMU	Data was not obtained due to power failure.										
28	Prelim CMU	1613	2183	1898	4600	4200	4400	N/A[2]	N/A[2]	N/A[2]	N/A[2]	N/A[2]
29	Concrete	159	163	161	553	530	542	15	15	1112	1093	1103
30	Concrete	162	165	164	528	534	531	15	15	1103	1091	1097
31	CMU	159	172	166	550	564	557	15	15	1083	1074	1079
32	CMU	187	188	188	575	598	587	15	15	1123	1109	1116
33	Ann. Glass	172	172	172	434	436	435	13	13	687	660	674
34	Ann. Glass	166	167	167	427	415	421	13	13	710	672	691
35	CMU	1620	1690	1655	4115	4012	4064	18	18	7255	7877	7566
36	Concrete	1583	1931	1757	3955	3756	3856	18	18	7000	7583	7292
37	CMU	1700	1987	1844	3918	4378	4148	16	16	7000	7200	7100
38	Concrete	1589	1996	1793	4354	4571	4463	16	18	7500	6500	7000
39	Temp. Glass	1324	1578	1451	1979	1822	1901	20	20	6000	5720	5860

1. Measured at pressure gages located 3.25 in. up-tube from the leading edge of the test sample.
2. Data was not obtained due to gage failure (fragments cut cord).

A wide-angle side-view Phantom 7.1 HSV camera was used to look for fragments passing through, over, or around the fragment collection system. Few such fragments were observed. For example, Figure 19 shows four selected screen captures from Test 23, a lower-pressure (<1000 psi) test done using with the original fragment collection system. For another example, Figure 20 shows four selected screen captures from Test 36, a higher-pressure (>1000 psi) test done using the new fragment collection system. In these examples and in general, the old and new fragment collection systems appeared to be equally successful at capturing the full fragment spray.

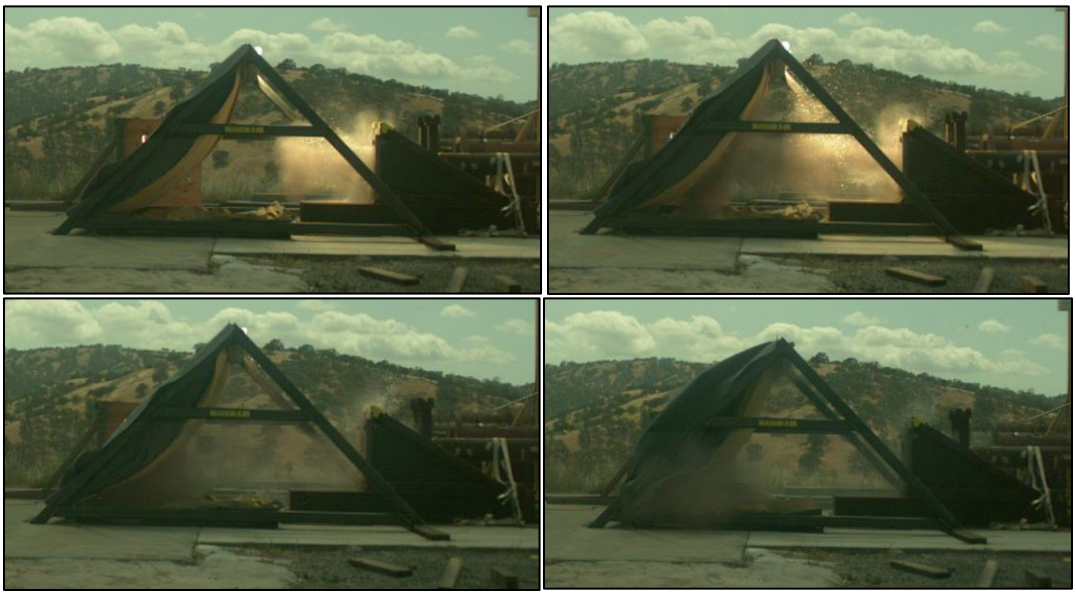

Figure 19. Screenshots from the overview HSV camera in Test 23 (May 2015).

Figure 20. Screenshots from the overview HSV camera in Test 36 (June 2015).

In order to estimate the initial fragment size distribution in the glass tests, a Phantom 7.2 HSV camera was used to record a mirror image of the sample's rear face with 320x240 pixels at 33,057

frames/sec. Only a single quadrant of the image was analyzed. Figure 21 shows the initial crack pattern for three of the four tempered glass tests, Figure 22 shows the initial crack pattern for the two annealed glass tests, Figure 23 shows the intial crack pattern for the three of the five concrete tests, and Figure 24 shows the initial crack pattern for the four CMU tests. In several of the high-pressure cases, the rear-view HSV was obscured by the fireball; these cases are omitted.

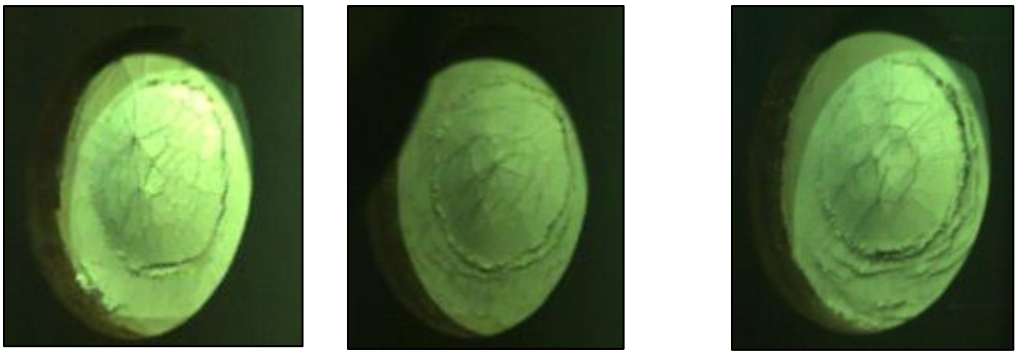

(a) Test 22 (225 psi) (b) Test 23 (350 psi) (c) Test 24 (350 psi)

Figure 21. Screenshots from the rear-view HSV showing the initial crack pattern of tempered glass specimens.

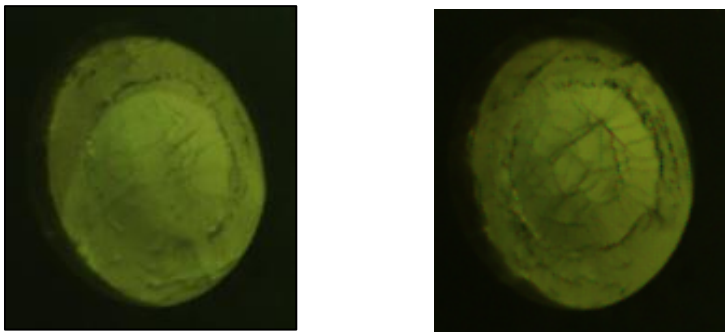

(a) Test 33 (350 psi) (b) Test 34 (350 psi)

Figure 22. Screenshots from the rear-view HSV showing the initial crack pattern of annealed glass specimens.

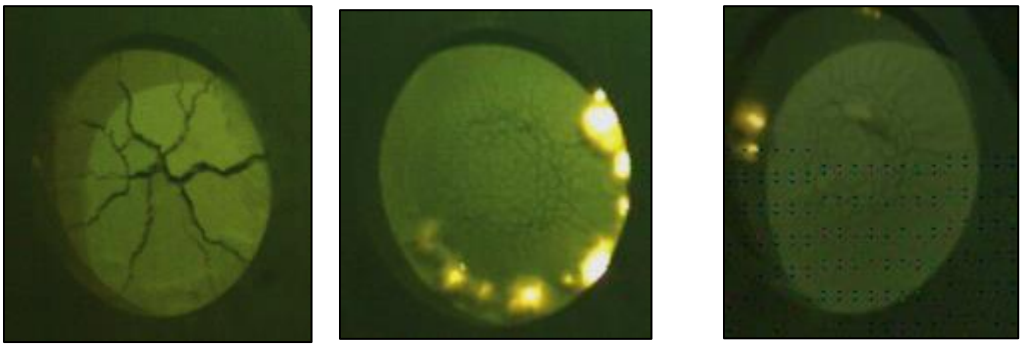

(a) Test 30 (500 psi) (b) Test 36 (4,000 psi) (c) Test 38 (4,000 psi)

Figure 23. Screenshots from the rear-view HSV showing the initial crack pattern of concrete specimens.

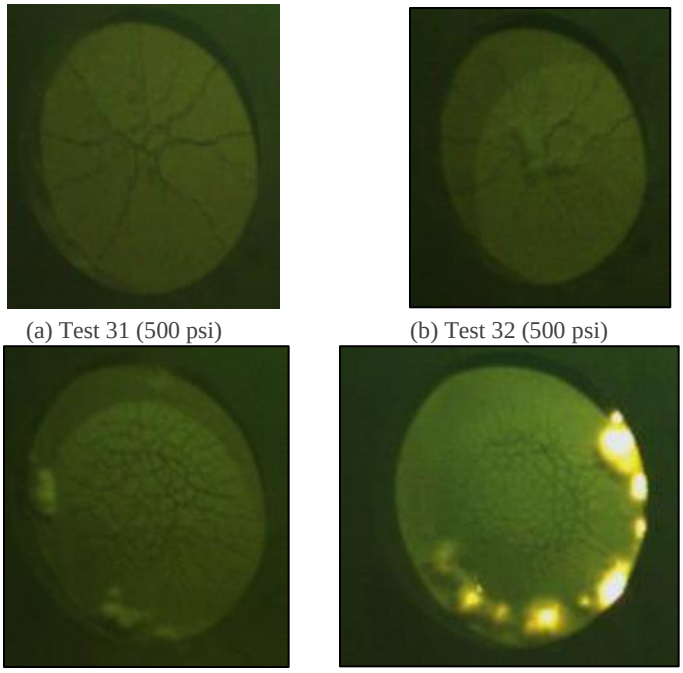

(a) Test 31 (500 psi) (b) Test 32 (500 psi)

(c) Test 35 (4,000 psi) (d) Test 37 (4,000 psi)

Figure 24. Screenshots from the rear-view HSV showing the initial crack pattern of CMU specimens.

Table 4 shows the total mass of physically-collected fragments, both in pounds and as a percentage of the original sample mass. Notice that nearly the entire sample was recovered in most of the lower-pressure tests and half to two-thirds of the sample was recovered in most of the higher-pressure tests. The mass percentages are much greater than those obtained in the first test series, where substantial numbers of fragments were excluded by the fragment stripper [1].

Table 4. Masses of physically-collected fragments.

Test	Sample Type	Reflected Over-Pressure[1] (psi)	Sample Mass (lb)	Collected Mass (lb)		Collected Amount (%)		
				On or Near Fragment Collection System	On or Near Sample Mount	On or Near Fragment Collection System	On or Near Sample Mount	Total
22	Tempered Glass	223	5.15	2.3	2.25	44.7%	43.7%	88.3%
23	Tempered Glass	407	5.15	2.2	2.35	42.7%	45.6%	88.3%
24	Tempered Glass	440	5.15	2.1	2.1	40.8%	40.8%	81.6%
25	Tempered Glass	2442	5.15	0.35	1.65	6.8%	32.0%	38.8%
29	Concrete	542	40.95	16.4	21.35	40.0%	52.1%	92.2%
30	Concrete	531	42.25	21.15	20.2	50.1%	47.8%	97.9%
31	CMU	557	38.15	17.35	14.85	45.5%	38.9%	84.4%
32	CMU	587	36.4	15.8	18.15	43.4%	49.9%	93.3%
33	Annealed Glass	435	5.3	2.55	2.25	48.1%	42.5%	90.6%
34	Annealed Glass	421	5.3	2.65	2.35	50.0%	44.3%	94.3%
35	CMU	4064	28.2	4.35	7.85	15.4%	27.8%	43.3%
36	Concrete	3856	21.05	5.9	7.8	28.0%	37.1%	65.1%
37	CMU	4148	27.9	6.6	8.55	23.7%	30.6%	54.3%
38	Concrete	4463	21.65	6.35	7.25	29.3%	33.5%	62.8%
39	Tempered Glass	1901	5.1	1.25	1.95	24.5%	38.2%	62.7%

[1] Average reflected peak pressure measured at 3.25-in up-tube from the leading edge of the sample.

3 ANALYSIS TECHNIQUES FOR FRAGMENT DISTRIBUTIONS

3.1 IMAGE ANALYSIS

Earlier reports fully described the techniques used to analyze the early-time rear-view HSV, the mid-time side-view HSV, and the late-time physical collection results; see and [2]. Instead of repeating all of the descriptions from the earlier reports, this section will review just the techniques used to analyze the physically-collected fragments.

The fragments collected in each test were passed through a series of increasingly finer sieves, in order to group them into rough size ranges. After the overall contents of each sieve were weighed, the fragments were manually laid out on a flat surface, being careful to separate them to avoid clusters that might appear to be a single fragment. A minimum fragment size of 0.005g was imposed because it was impractical to manually separate fragments smaller than that. The resulting display was photographed and analyzed using SigmaScan Pro, a well-known commercial image analysis package. To improve fragment characterization, SigmaScan Pro was used to convert the color images to high-contrast grayscale images. The resulting SigmaScan Pro images were inspected and lines were drawn manually between adjacent fragments as necessary to ensure that each fragment was counted individually. While this required extra effort, it eliminated the need to use special logic functions and VBA code, as described in Reference [1], to enforce the 0.005g lower limit. Starting from the high-contrast digital images, SigmaScan Pro was used to estimate the in-plane dimensions, cross-sectional areas, and other geometrical information for each fragment.

As an example, Figure 25 shows the original and processed image for Sieve No. 4 in Test 23. In addition, Figure 26 shows the in-plane dimensions, cross-sectional areas, and other geometrical information for Sieve No. 4 in Test 23, as estimated using SigmaScan Pro.

(a) Original full-color photograph (b.) High-contrast digital image produced by SigmaScan Pro.

Figure 25. Fragments captured by Sieve No. 4 in Test 23.

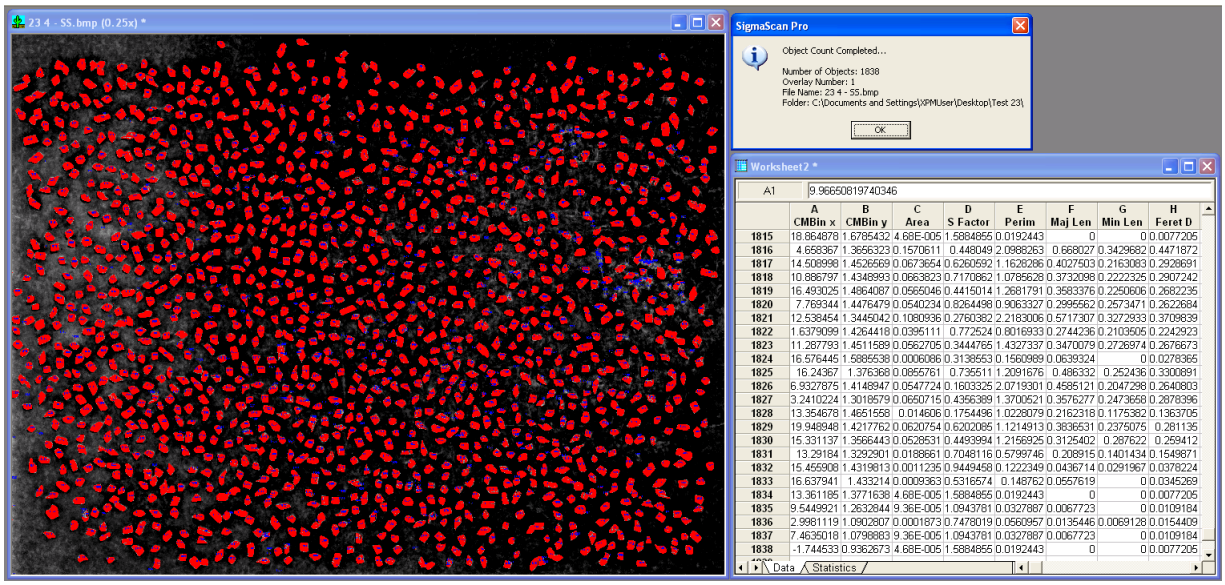

Figure 26. SigmaScan Pro results including a processed image (left) and a spreadsheet of geometrical information on each fragment (right) corresponding to Figure 25.

Finally, the SigmaScan Pro results for two-dimensional in-plane fragment dimensions and cross-sectional fragment areas were used to estimate three-dimensional fragment masses and diameters. More specifically, for thin enough samples and large enough fragments, fragments will inherit two smooth surfaces from the original sample. Then:

$$M_i = \rho t A_i$$

where M_i is the mass of fragment i, A_i is the cross-sectional area of fragment i as measured by SigmaScan Pro, ρ is the density, and t is the original sample thickness, e.g., $t = 0.25$ for the plate glass tests. For thicker samples and smaller fragments, the fragments will be rough on all sides, i.e., they will not inherit any smooth surfaces from the original sample. Then:

$$M_i \approx A_i \cdot \frac{\sum M_j}{\sum A_j}$$

where the sums refer to all of the fragments in a given size bin. In other words, the mass-to-area ratio of any individual fragment is assumed to be approximately equal to the cumulative mass to cumulative area ratio of all fragments in the same bin.

3.2 CURVE FITTING

Microsoft Excel was used to fit power law and Weibull size distributions to the experimental fragment masses. To define power law and Weibull size distributions, it is first necessary to define complementary cumulative distribution functions (CDFs) and probability density functions (PDFs). The complementary *cumulative distribution function* $F(M)$ is the number fraction of fragments with masses greater than or equal to *M*. Similarly, the *probability density function* $f(M)$ is the number fraction of fragments with masses in a range *dM* centered on *M* divided by *dM*.

Notice that $F(x)$ is monotone decreasing such that $F(0)=1$ and $F(\infty)=0$. In addition, notice that $f(x)$ is always non-negative such that:

$$\int_0^\infty f(x)dx = 1.$$

Finally notice that:

$$F(M) = -\int_M^\infty f(x)dx\,;\;\; f(M) = -\frac{dF}{dM}.$$

These definitions assume an infinite range of fragment sizes. However, experimental results always obtain a limited finite range of fragment sizes. The CDFs and PDFs over a limited range $M_{\min} \le M \le M_{\max}$ are related to the CDFs and PDFs over an infinite range as follows:

$$\tilde{F}(M) = \frac{F(x) - F(M_{\min})}{F(M_{\max}) - F(M_{\min})}$$

$$\tilde{f}(M) = \frac{f(M)}{F(M_{\max}) - F(M_{\min})}.$$

The *count mean mass* is defined as follows:

$$M_{avg} = \int_0^\infty Mf(M)dM$$

for an infinite range and:

$$\tilde{M}_{avg} = \int_{M_{\min}}^{M_{\max}} M\tilde{f}(M)dM = \frac{\int_{M_{\min}}^{M_{\max}} Mf(M)dM}{\int_{M_{\min}}^{M_{\max}} f(M)dM}$$

for a finite range.

Normalizing by the count mean mass, *Weibull size distributions* may be defined as follows:

$$F(M) = \exp\left[-c\left(\frac{M}{M_{avg}}\right)^r\right]$$

$$f(M) = \frac{c\,|r|}{M_{avg}} \left(\frac{M}{M_{avg}} \right)^{r-1} \exp\left[-c \left(\frac{M}{M_{avg}} \right)^{r} \right]$$

where r is a free parameter and where:

$$c = \Gamma\left(1 + \frac{1}{r} \right)^{r} .$$

Similarly, power law size distributions may be defined as follows:

$$F(M) = \begin{cases} 1 - (M / M_{\max})^{r} & r > 0 \\ (M / M_{\min})^{r} & r < 0 \end{cases}$$

$$f(M) = \begin{cases} \dfrac{r}{M_{\max}} \left(\dfrac{M}{M_{\max}} \right)^{r-1} & r > 0 \\ \dfrac{|r|}{M_{\min}} \left(\dfrac{M}{M_{\min}} \right)^{r-1} & r < 0 \end{cases} .$$

Notice that Weibull size distributions are approximately equal to power law size distributions for sufficiently large or small fragments, depending on the sign of r.

The initial curve fitting procedure used fixed bin widths. However, this resulted in overpopulated small bins, underpopulated large bins, and suboptimal fits overall. We thus used variable bin widths that minimized bin-to-bin variations in mass.

To further examine the effects of binning, three types of fits were considered: a coarse fit based on 10 sizes bins; a medium fit based on 35 size bins; and a fine fit based on 150 size bins. The medium fit tended to obtain the best results and was thus used in all cases reported here.

The rear-view and side-view HSV data tended to obtain a relatively narrow range of fragments, often only one or two orders-of-magnitude, which affected the perceived average fragment size. The average fragment size was thus based on the physically-collected data in all cases. For additional information on the curve fitting procedures used here see, e.g., Table 7 in Reference [1].

4 TEST RESULTS FOR FRAGMENT SIZE DISTRIBUTIONS

4.1 MASS DISTRIBUTIONS FROM EARLY-TIME REAR-VIEW HSV ANALYSIS

Rear-view HSV can be used to estimate early-time fragment size distributions for thin test articles, such as plate glass. However, rear-view HSV cannot be used to estimate early-time fragment size distributions for thick test objects, such as concrete and CMU, because most of the fragments form in the interior of the test object, out of view of the camera.

This effort analyzed the rear-review HSV results for one tempered glass test (Test 24) and two annealed glass tests (Tests 33 and 34). This effort did not analyze rear-view HSV results for the remaining tempered glass tests (Tests 22, 23, 25 and 39).

Table 5 and Table 6 summarize the outcome of the rear-view HSV analysis. For comparison, these tables also include results for three tempered glass tests (Tests 13, 15, and 16) from Test Series 1 [1]. These results indicate that tempered and annealed glass both obtain the same fragment size distribution, namely, a Weibull size distribution with $r = 0.66 \pm 0.03$.

Table 5. Statistical parameters for rear-view HSV mass in Tests 24, 33, and 34 involving plate glass test objects.

Material	Test	Peak Overpressure (psi)	# Frags Observed	Mass Frags Observed (g)	% Original Quadrant Mass	% Original Sample Mass
Tempered Glass	13 [1]	470	431	375	63.6%	15.9%
	15 [1]	227	414	541	91.7%	22.9%
	16 [1]	468	651	520	89.0%	22.3%
	24	441	354	459	78.6%	19.6%
Annealed Glass	33	436	208	277	46.1%	11.5%
	34	427	221	309	51.4%	12.95

Table 6. Best-fit Weibull parameters based on rear-view HSV mass in Tests 24, 33, and 34 involving plate glass test objects.

Material	Test	Weibull Parameters			
		r	M_{min} (g)	M_{max} (g)	$\widetilde{M}_{avg}$ (g)
Tempered Glass	13 [1]	1.06 (*)	0.003	10.65	0.866
	15 [1]	0.69	0.0004	71.35	1.250
	16 [1]	0.64	0.003	7.52	0.798
	24	0.79 (*)	0.005	15	1.31
Annealed Glass	33	0.70	0.005	15	1.33
	34	0.64	0.005	15	1.33
	Combined	0.67			

(*) Measured before the fragments were fully formed.

In general, the fragment size spread increases over time until it reaches a maximum. In other words, the best-fit Weibull exponent r decreases over time until it reaches a minimum. An attempt was made to choose a time after r reached a stable minimum but before transverse motions led to fragments in the front blocking views of fragments in the rear. However, because of the difficulty of selecting the ideal time, in two cases, the results were analyzed somewhat before r reached its stable minimum; these cases are noted by an asterisks in Table 6.

Figure 27, Figure 28, and Figure 29 show the best-fit Weibull size distributions for Test 24, Test 33, and Test 34, respectively.[1] In addition, Figure 30 shows the best-fit Weibull size distribution for the combination of Tests 33 and 34; because the test conditions were almost identical, the results should also be almost be almost identical, except for inherent random shot-to-shot variation, which preferentially affects the rarer, larger fragments.

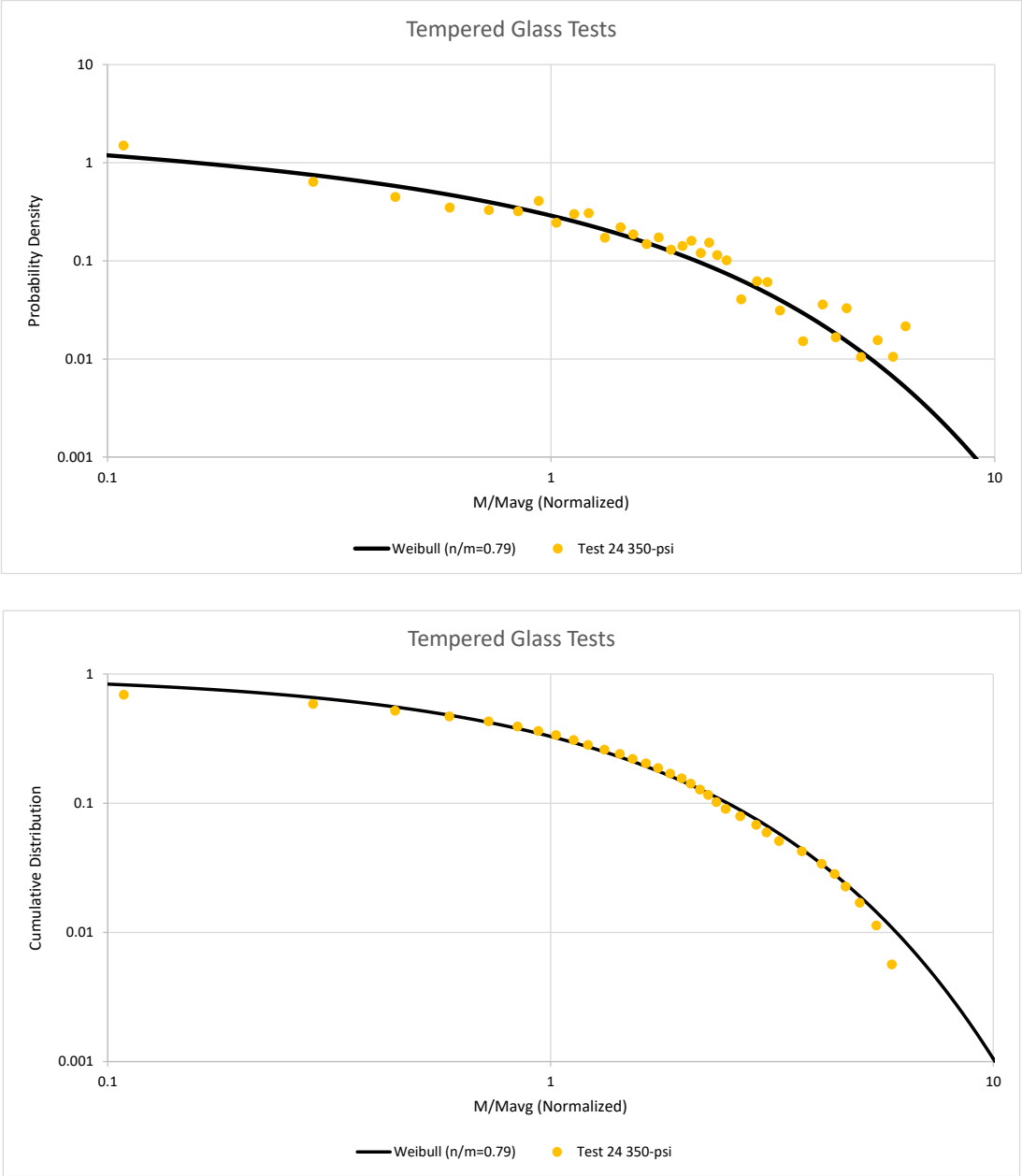

Figure 27. Best-fit Weibull mass distribution for rear-view HSV test data for PDF (top) and CDF (bottom) for Test 24 for tempered glass.

[1] In these and all subsequent figures, the label "Probability Density" on the vertical axis refers to the PDF *times the count mean mass*, i.e., it refers to $M_{avg} f(M)$.

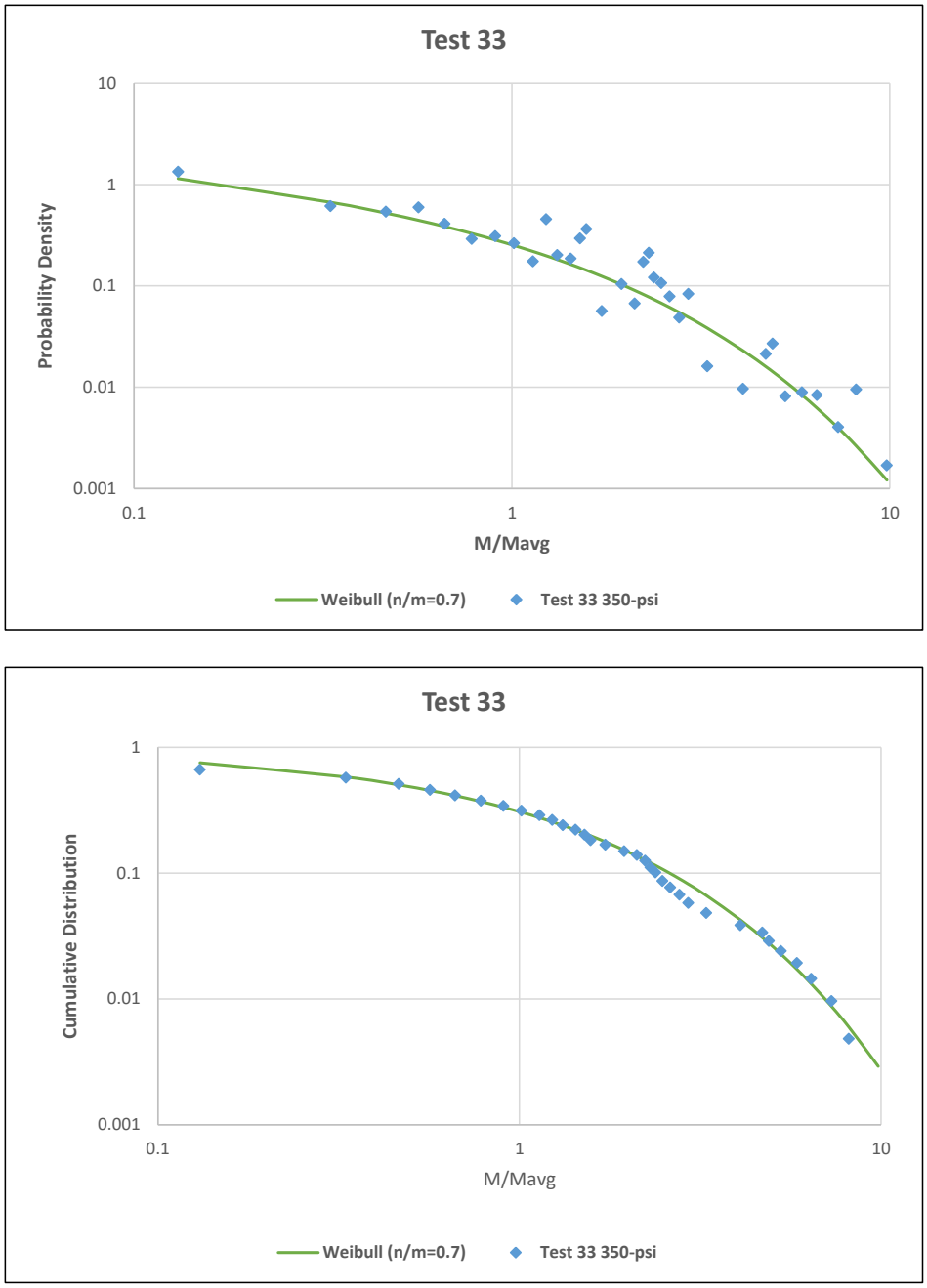

Figure 28. Best-fit Weibull mass distribution for rear-view HSV test data for PDF (top) and CDF (bottom) for Test 33 for annealed glass.

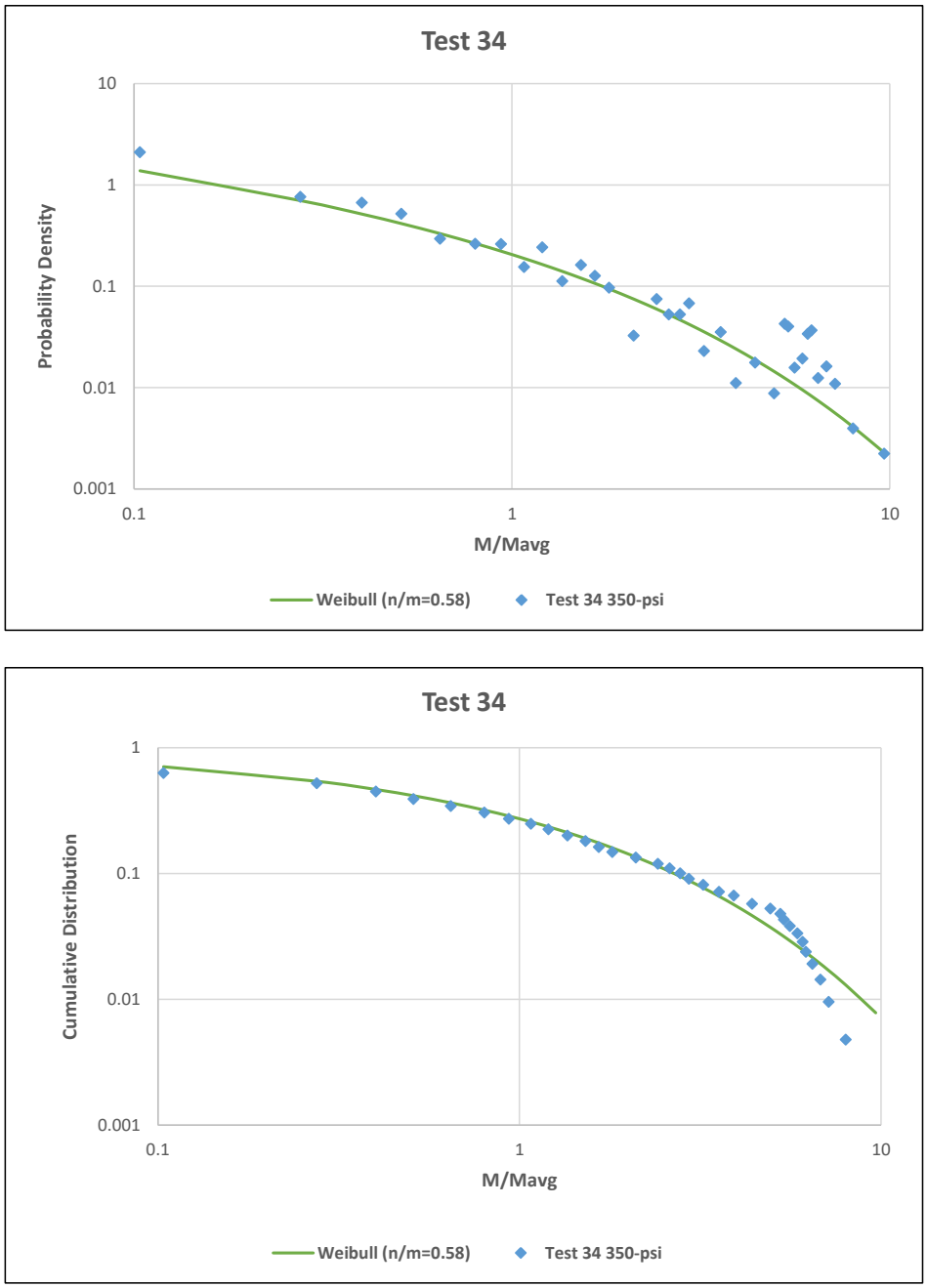

Figure 29. Best-fit Weibull mass distribution for rear-view HSV test data for PDF (top) and CDF (bottom) for Test 34 for annealed glass.

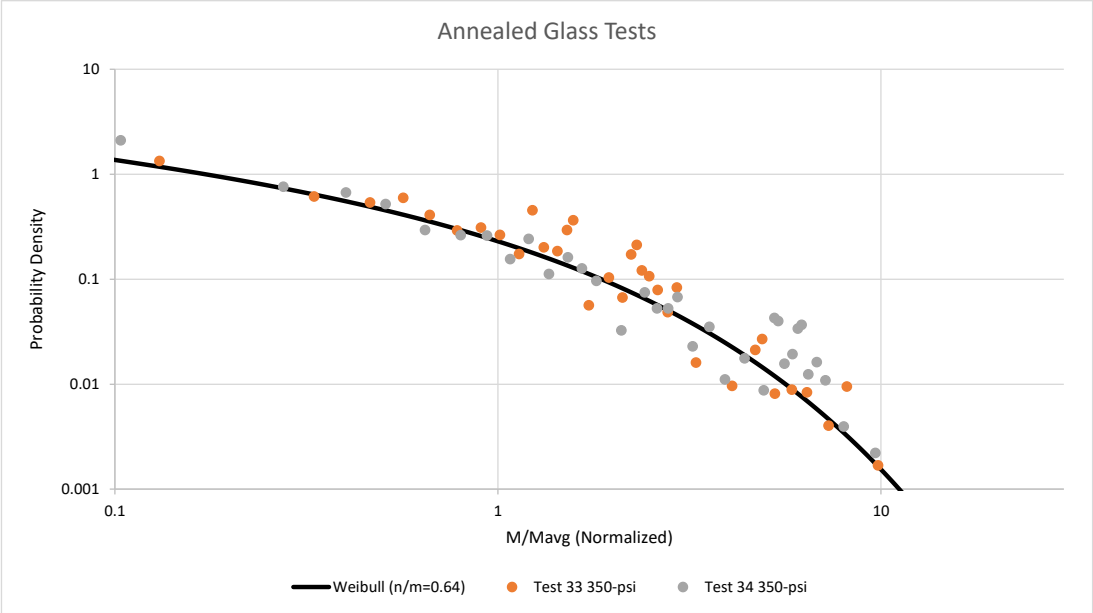

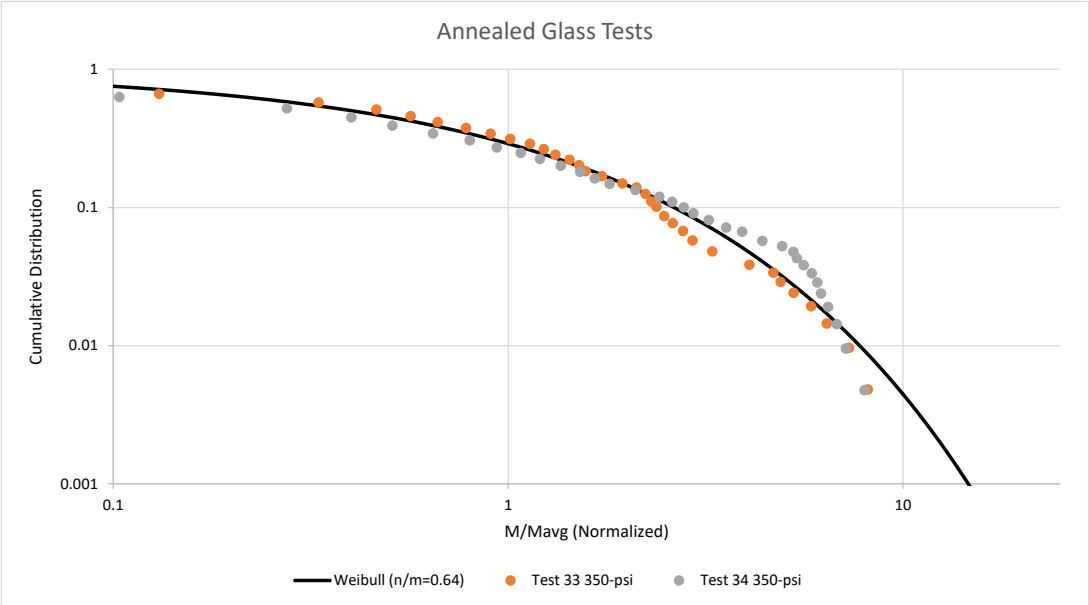

Figure 30. Best-fit Weibull mass distributions for rear-view HSV test data for PDF (top) and CDF (bottom) for Tests 33 and 34 for annealed glass.

4.2 MASS DISTRIBUTIONS FROM MID-TIME SIDE-VIEW HSV ANALYSIS

As noted in References [1] and [2], the technique used to measure in-flight fragments obtained unacceptable results. In the first test series, a fragment stripper was used to limit fragments to a single focal plane. This led to a simple technique for converting between apparent and real lengths, as observed by a single camera, based on a simple fiduciary video of a ruler. However, given the limited resolution of the HSV camera used, only a subset of the largest fragments was observed, which led to substantial errors in estimating the fragment size distribution [1]. In the second test series, in an attempt to increase the number of visible fragments, the fragment stripper was

removed [2]. Unfortunately, this meant that fragments located further or closer to the camera than the assumed plane appeared to be smaller or larger than they actually were, respectively. There was no obvious way to correct for this distortion. In some cases, this distortion was so severe that the apparent mass of the observed fragments exceeded the mass of the original test article.

In short, with or without the fragment stripper present, the single side-view camera results were unreliable and inconsistent with the rear-view and physically-collected results. Thus, while side-view HSV cameras were deployed in the third test series, the results were not analyzed.

A future test series will address these problems by using three higher-resolution HSV cameras to record the in-flight fragments, which should allow for three-dimensional characterization of fragment shapes and velocities, including substantially smaller fragments than before.

4.3 MASS DISTRIBUTIONS FROM PHYSICAL COLLECTION (SIEVE) ANALYSES

Table 7 and Table 8 summarize the outcome of the physical collection results. For comparison, these tables include results both from the first and third test series.

Table 7. Statistical parameters for physically-collected fragment mass distributions.

Material	Test	Peak Overpressure (psi)	# Frags Observed	Mass Frags Observed (g)	% Original Sample Mass
Tempered Glass	13 [1]	469	3,967	163	6.9%
	14 [1]	236	3,967	387	16.4%
	15 [1]	227	3,579	310	13.1%
	16 [1]	468	3,703	190	8.1%
	22	226	14,513	1,047	44.8%
	23	416	21,066	1,008	43.2%
	24	441	20,845	953	40.8%
	25	2,492	6,549	154	6.6%
	39	1,979	5,792	147	6.4%
Annealed Glass	33	436	13,924	992	41.2%
	34	427	11,977	1,096	45.6%
Concrete	5 [1]	1,424	4,831	2,286	12.5%
	6 [1]	~3,000	3,751	678	3.7%
	8 [1]	2,847	3,905	877	4.7%
	9 [1]	2,783	4,564	1,133	6.5%
	29	553	20,121	7,242	40.0%
	30	534	9,523	8,894	46.4%
	36	3,955	19,148	1,499	15.7%
	38	4,378	26,794	1,805	21.7%
CMU	3 [1]	1,250	4,520	1,661	9.0%
	4 [1]	3,710	7,481	491	2.7%
	7 [1]	1,353	8,367	1,611	8.9%
	10 [1]	3,008	6,779	649	3.6%
	12 [1]	2,845	6,576	649	3.5%
	31	564	20,730	7,563	43.7%
	32	598	26,450	6,677	40.4%
	35	4,115	32,126	1,255	9.8%
	37	3,955	33,796	1,699	13.4%

Table 8. Best-fit Weibull and power law parameters based on physically-collected fragment mass data

Material	Test	Fitting Parameters Method 2 – Jul 2018					Fitting Parameters Method 3 – September 2018				
		Weibull r	Power r	M_{min} (g)	M_{max} (g)	$\widetilde{M}_{avg}$ (g)	Weibull r	Power r	M_{min} (g)	M_{max} (g)	$\widetilde{M}_{avg}$ (g)
Tempered Glass	13 [1]	0.64	–0.84	0.005	1.5	0.046	0.61	–0.86	0.01	1.6	0.041
	14 [1]	0.65	–0.61	0.005	1.5	0.119	0.65	–0.64	0.01	3	0.098
	15 [1]	0.56	–0.66	0.005	1.5	0.109	0.50	–0.70	0.01	3	0.087
	16 [1]	0.57	–0.76	0.005	1.5	0.066	0.50	–0.79	0.01	3	0.051
	Avg	0.61	–0.72	0.005	1.5	0.085	0.57	–0.75	0.01	2.65	0.069
	22	0.60	–0.72	0.005	1.5	0.073	0.63	–0.75	0.01	3	0.072
	23	0.66	–0.79	0.005	1.5	0.048	0.69	–0.82	0.01	1	0.048
	24	0.68	–0.82	0.005	1.5	0.046	0.70	–0.87	0.01	2	0.046
	25	0.71	–1.14	0.005	1.5	0.025	0.67	–1.07	0.01	1	0.024
	39	0.68	–1.10	0.005	1.5	0.030	0.60	–1.02	0.01	1	0.025
	Avg	0.67	–0.91	0.005	1.5	0.044	0.66	–0.91	0.01	1.6	0.043
Annealed Glass	33	0.56	–0.84	0.005	1.5	0.058	0.51	–0.82	0.1	15	0.071
	34	0.54	–0.83	0.005	1.5	0.068	0.48	–0.82	0.01	10	0.092
	Avg	0.55	–0.83	0.005	1.5	0.063	0.495	–0.82	0.055	12.5	0.082
Concrete	5 [1]	0.65	–0.78	0.01	4	0.152	0.57	–0.82	0.01	16	0.209
	6 [1]	0.66	–0.82	0.01	5	0.124	0.60	–0.82	0.01	5	0.181
	8 [1]	0.63	–0.85	0.01	5	0.096	0.57	–0.85	0.01	5	0.164
	9 [1]	0.58	–0.75	0.01	4	0.148	0.52	–0.77	0.01	9	0.221
	Avg	0.63	–0.80	0.01	4.5	0.130	0.565	–0.82	0.01	8.75	0.194
	29	0.54	–1.00	0.01	5	0.078	0.52	–1.04	0.01	20	0.136
	30	0.55	–0.94	0.01	5	0.090	0.50	–0.94	0.01	8	0.165
	36	0.63	–1.06	0.01	5	0.075	0.54	–1.06	0.01	28	0.078
	38	0.60	–1.10	0.01	5	0.065	0.60	–1.13	0.01	9	0.067
	Avg	0.58	–1.02	0.01	5	0.077	0.54	–1.04	0.01	16.25	0.112
CMU	3 [1]	0.61	–0.82	0.01	5	0.123	0.59	–0.82	0.01	8	0.188
	4 [1]	0.64	–0.86	0.01	5	0.085	0.59	–0.86	0.01	5	0.066
	7 [1]	0.62	–0.85	0.01	5	0.135	0.58	–0.86	0.01	15	0.193
	10 [1]	0.67	–0.90	0.01	5	0.076	0.76	–0.90	0.01	5	0.096
	12 [1]	0.56	–0.86	0.01	12	0.102	0.73	–0.84	0.01	3	0.098
	Avg	0.62	–0.86	0.01	6.4	0.104	0.65	–0.86	0.01	7.2	0.620
	31	0.54	–1.10	0.01	5	0.060	0.47	–1.10	0.01	30	0.170
	32	0.55	–1.10	0.01	5	0.055	0.46	–1.13	0.01	30	0.209
	35	0.60	–1.30	0.01	5	0.039	0.72	–1.26	0.01	4	0.039
	37	0.61	–1.20	0.01	5	0.050	0.71	–1.24	0.01	6	0.050
	Avg	0.58	–1.17	0.01	5	0.051	0.59	–1.18	0.01	17.5	0.117

NOTE: The green shaded boxes indicate fits deemed to be acceptable. All other fits are substantially in error.

This effort compared three different automated fitting methods, which varied in terms of how the bin limits, the average fragment sizes, and so forth were chosen. For all three methods, for Weibull distributions, a $\chi 2$ approach was used to generate a single best fit for both PDFs and CDFs. In addition, for power law distributions, CDFs were fit first using $\chi 2$, then PDFs were fit.

In each case, the results of the automated fitting procedures were compared to the original experimental data. In most cases, at least one of three methods obtained an acceptable fit, either for a Weibull or a power law. In some cases, none of the three methods obtained an acceptable fit,

which implies that Weibull and power laws are not appropriate choices. In those cases, a piecewise (bi-linear) power law fit – where one power law is used for the smaller fragments and another power law is used for the larger fragments – often obtained an acceptable fit. Where a bi-linear power law fit was used, Table 8 shows the power law exponent only for the smaller fragments.

Table 8 indicates which fits were deemed acceptable using green shading. Table 8 shows the results only from Methods 2 and 3. The results for Method 1 are not shown. Where no acceptable fits were obtained with Methods 2 or 3, acceptable fits were usually obtained with Method 1.

Figure 31 to Figure 38 show Weibull, power law, and piecewise (bi-linear) power law curve fits for tempered glass obtained using Method 3. Figure 39 to Figure 43 show Weibull, power law, and piecewise (bi-linear) power law curve fits for annealed glass obtained using Method 3. Figure 44 to Figure 50 show Weibull, power law, and piecewise (bilinear) power law curve fits for concrete obtained using Method 3. Finally, Figure 51 to Figure 57 show Weibull, power law, and piecewise (bilinear) power law curve fits for CMU obtained using Method 3.

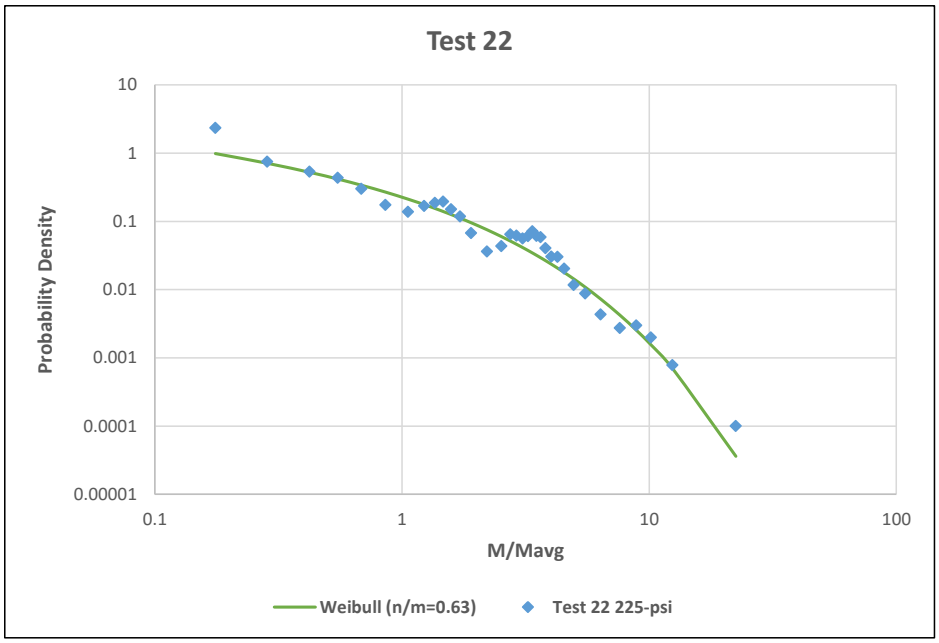

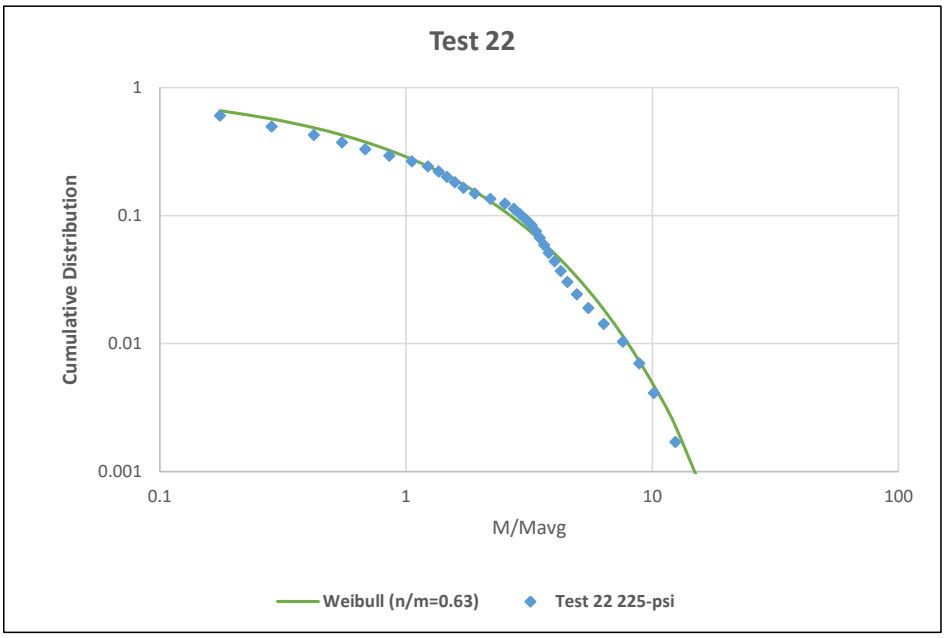

Figure 31. Best-fit Weibull mass distribution for physically-collected test data for PDF (top) and CDF (bottom) for Test 22 involving tempered glass.

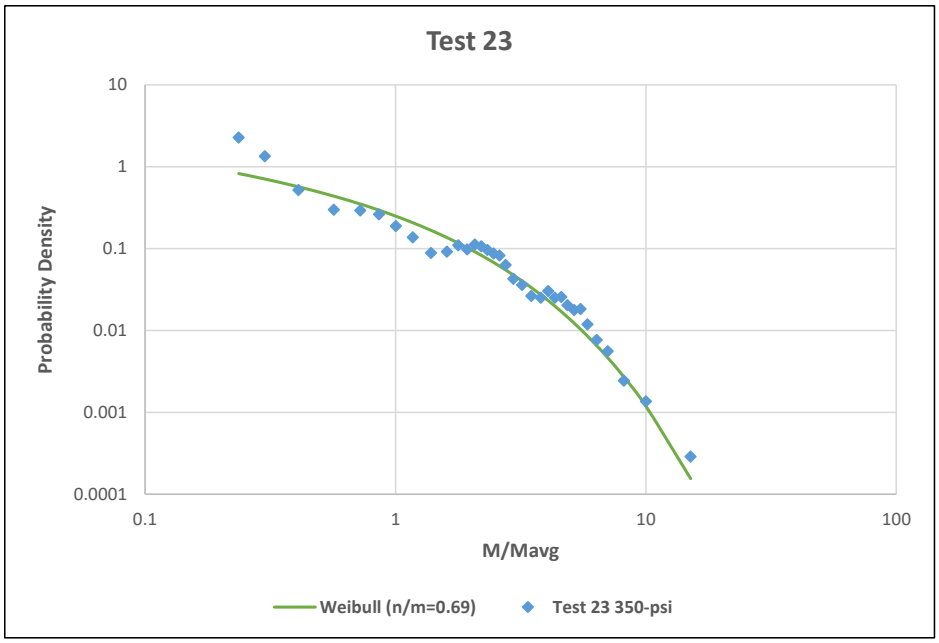

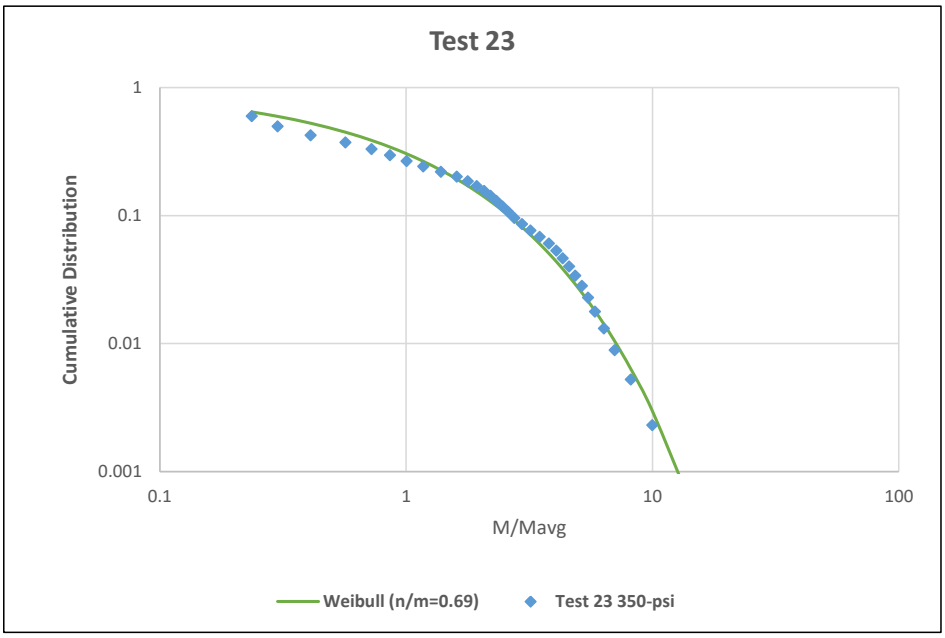

Figure 32. Best-fit Weibull mass distribution for physically-collected test data for PDF (top) and CDF (bottom) for Test 23 involving tempered glass.

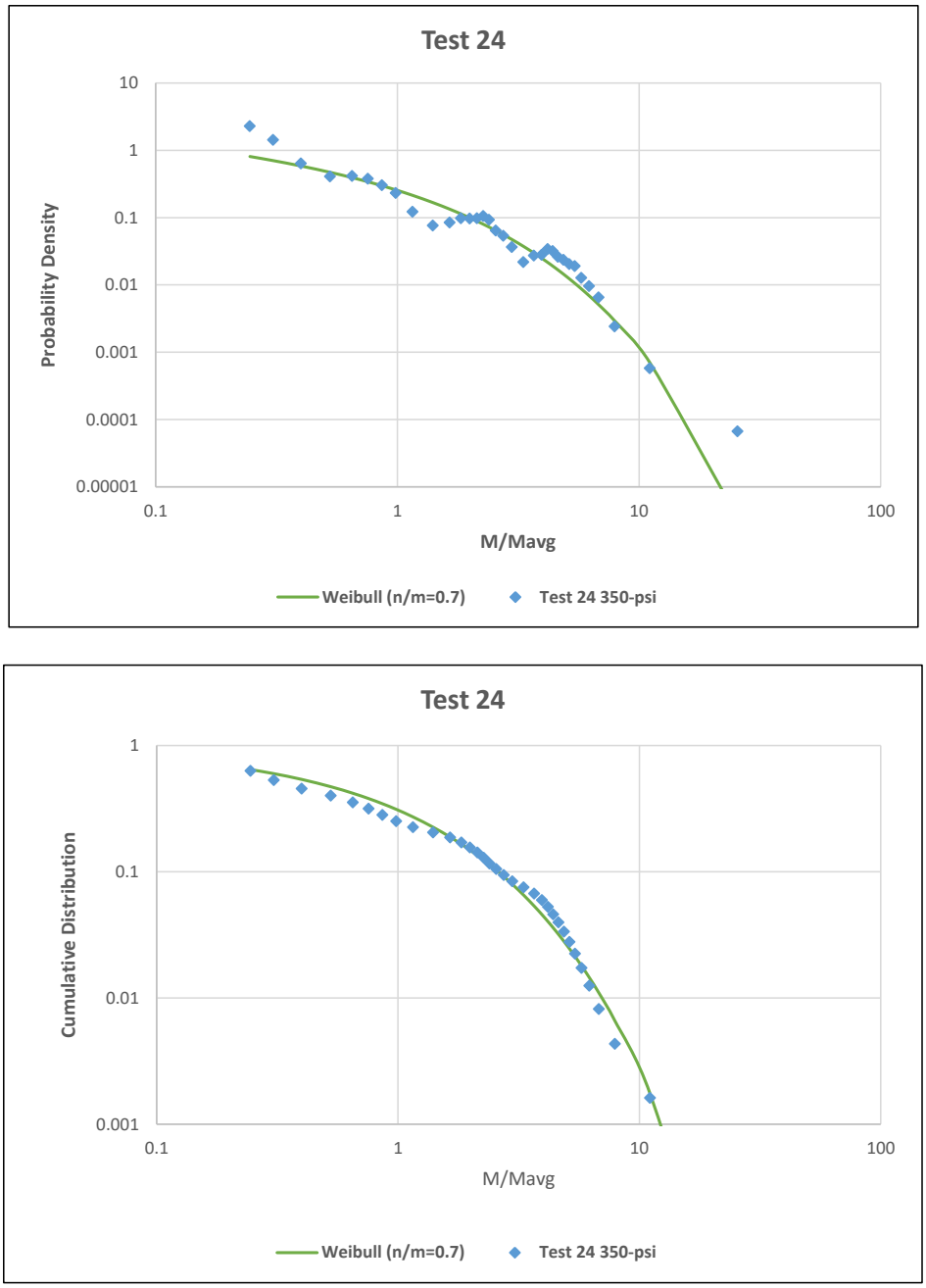

Figure 33. Best-fit Weibull mass distribution for physically-collected test data for PDF (top) and CDF (bottom) for Test 24 involving tempered glass.

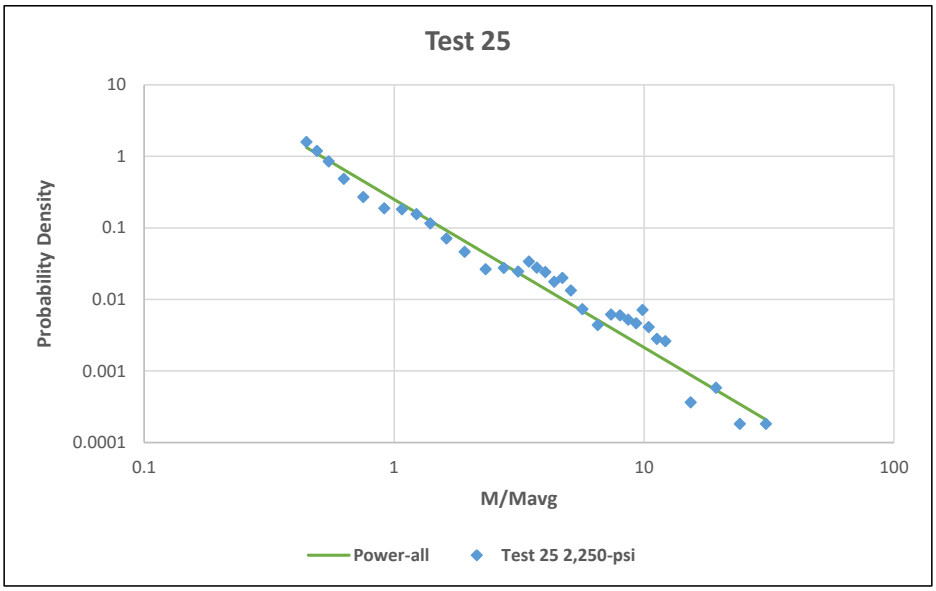

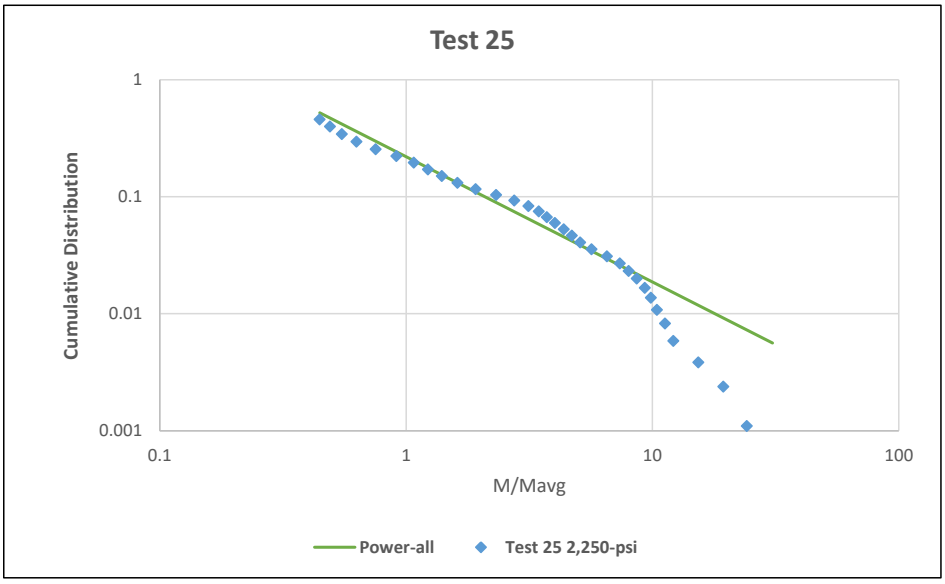

Figure 34. Best-fit power law mass distribution for physically-collected test data for PDF (top) and CDF (bottom) for Test 25 involving tempered glass.

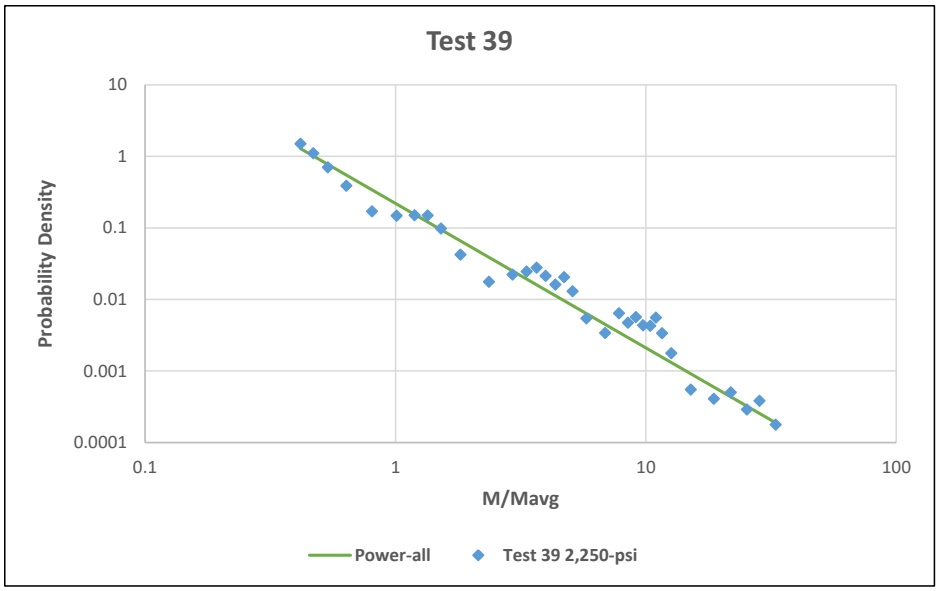

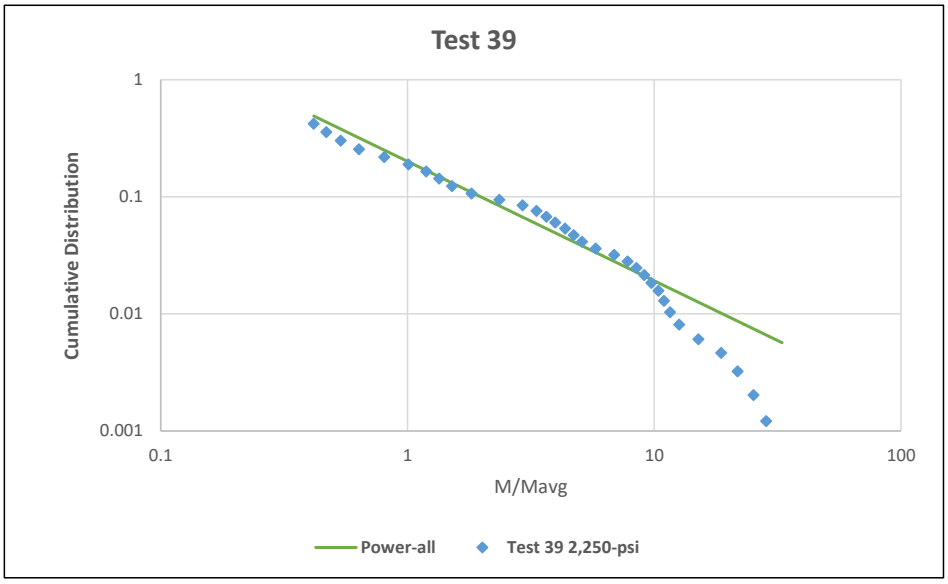

Figure 35. Best-fit power law mass distribution for physically-collected test data for PDF (top) and CDF (bottom) for Test 39 involving tempered glass.

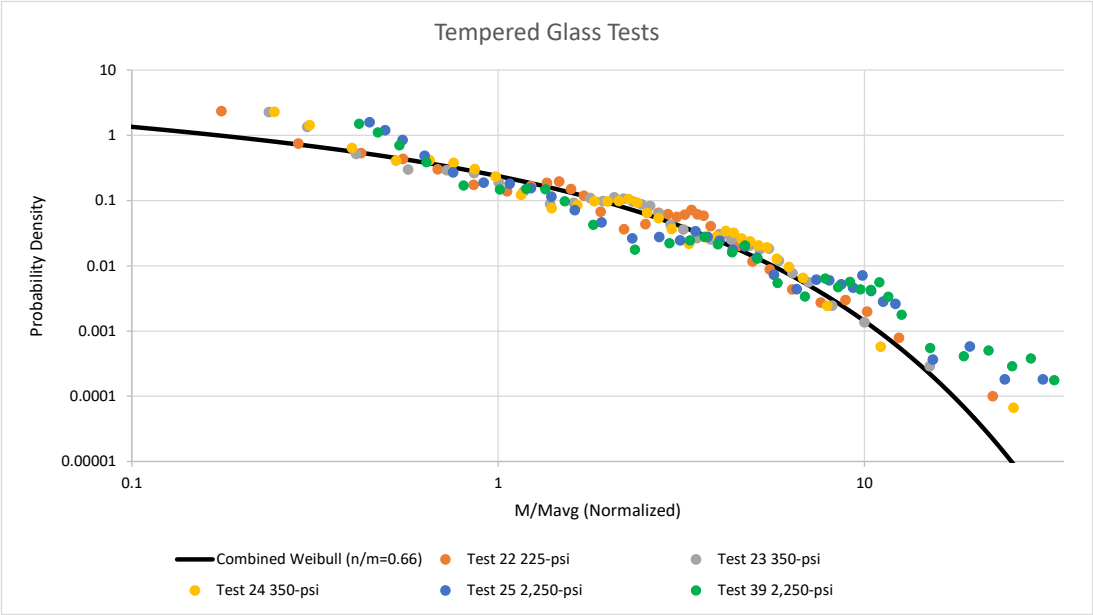

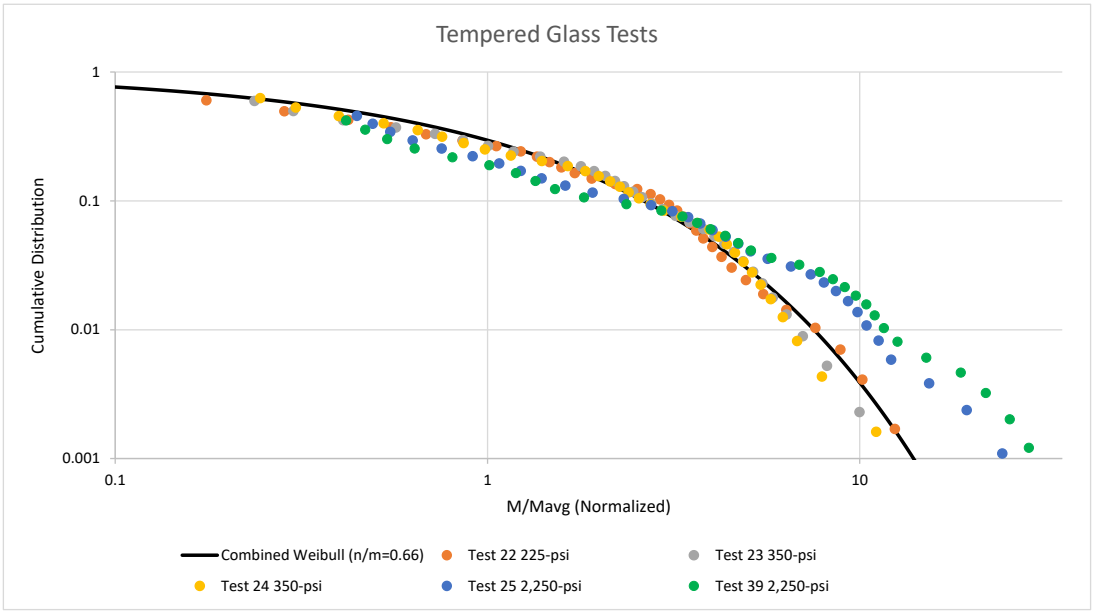

Figure 36. Best-fit Weibull mass distribution for physically-collected test data for PDF (top) and CDF (bottom) for Tests 22-25 and Test 39 involving tempered glass.

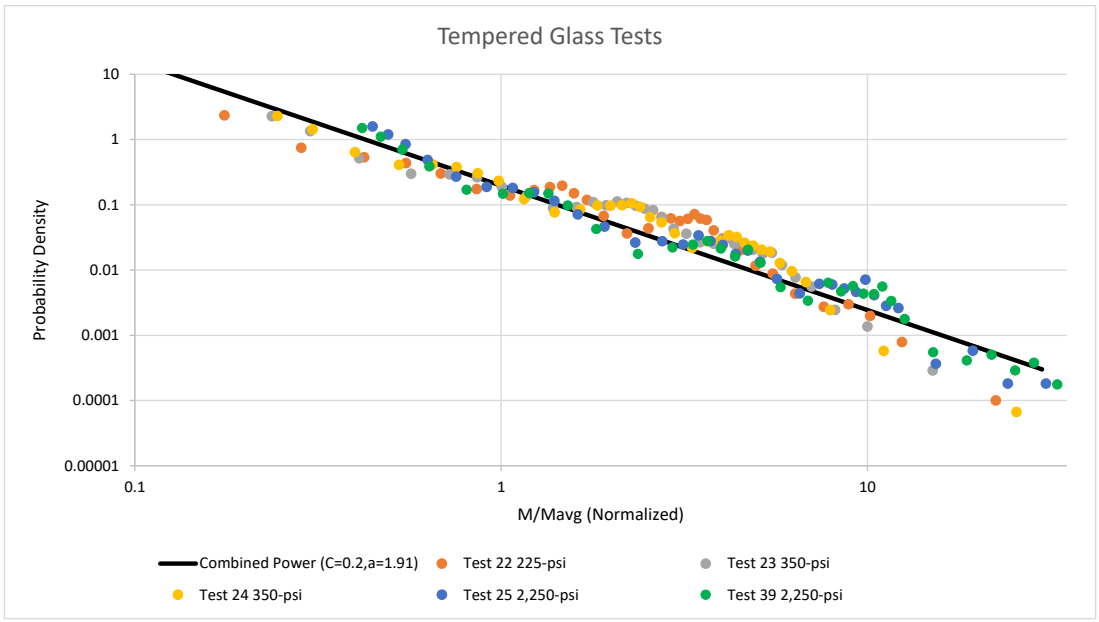

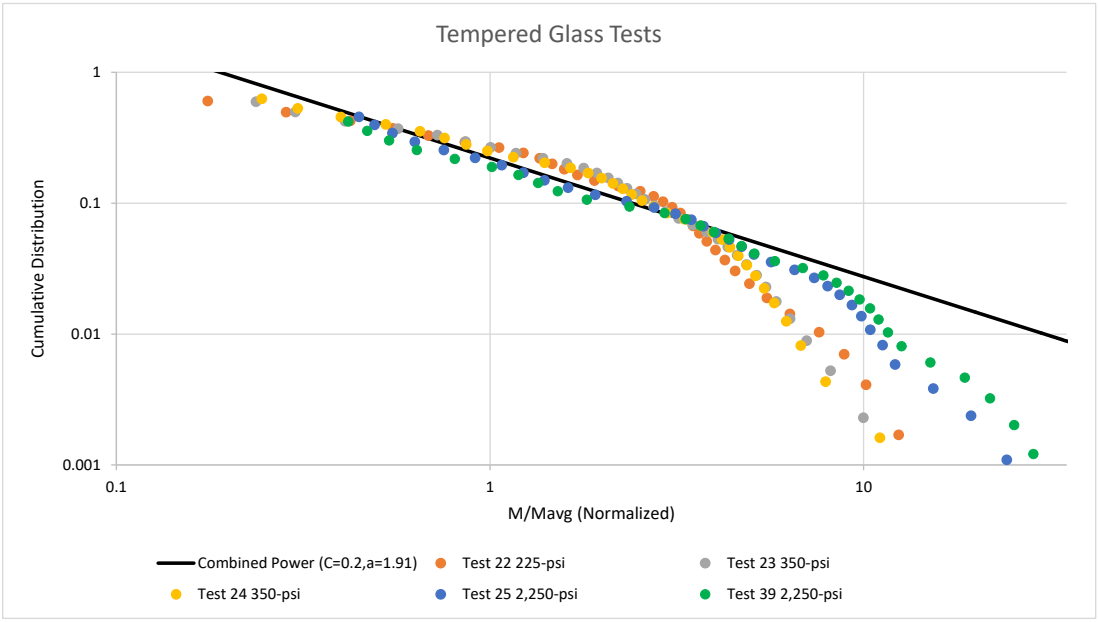

Figure 37. Best-fit power law mass distribution for physically-collected test data for PDF (top) and CDF (bottom) for Tests 22-25 and Test 39 involving tempered glass.

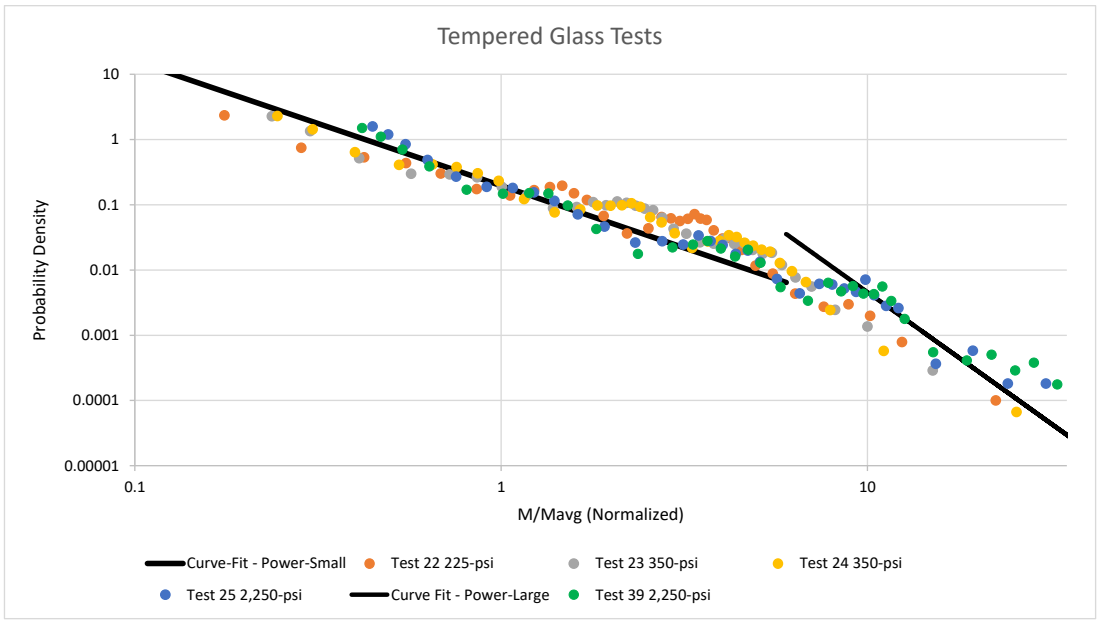

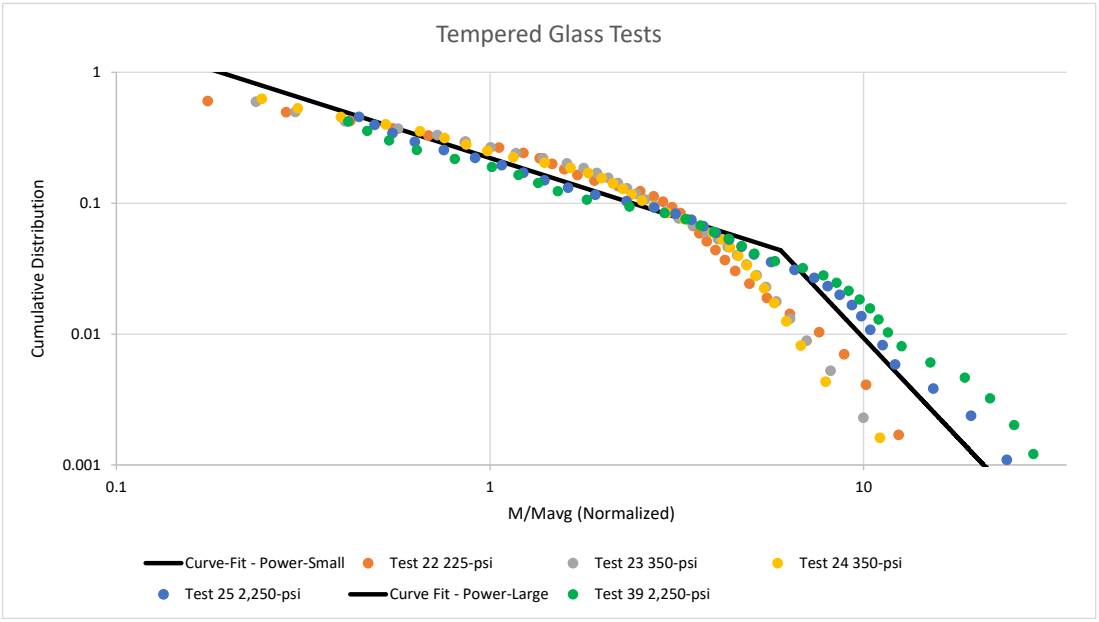

Figure 38. Best-fit bi-linear power law mass distribution for physically-collected test data for PDF (top) and CDF (bottom) for Tests 22-25 and Test 39 involving tempered glass.

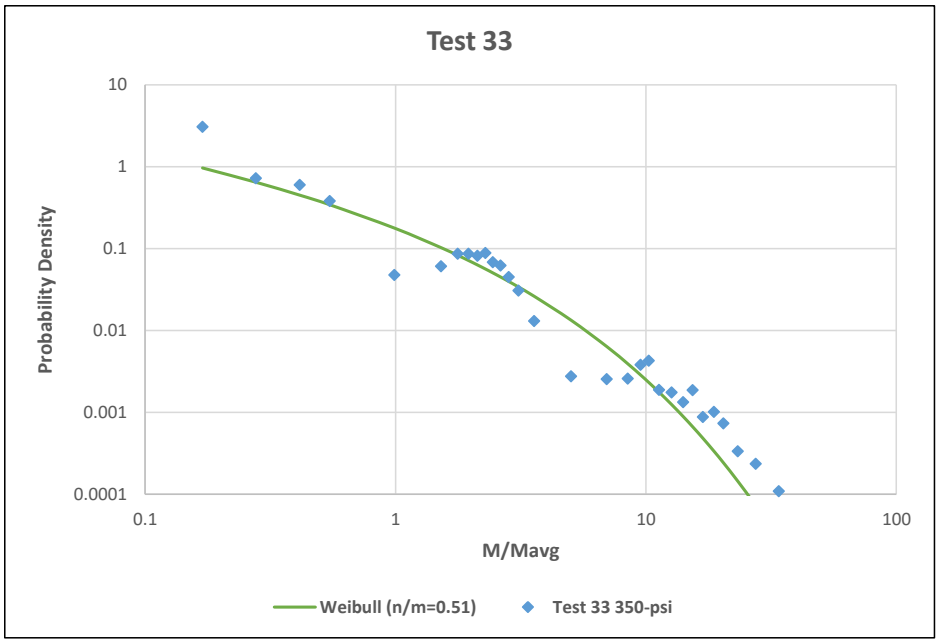

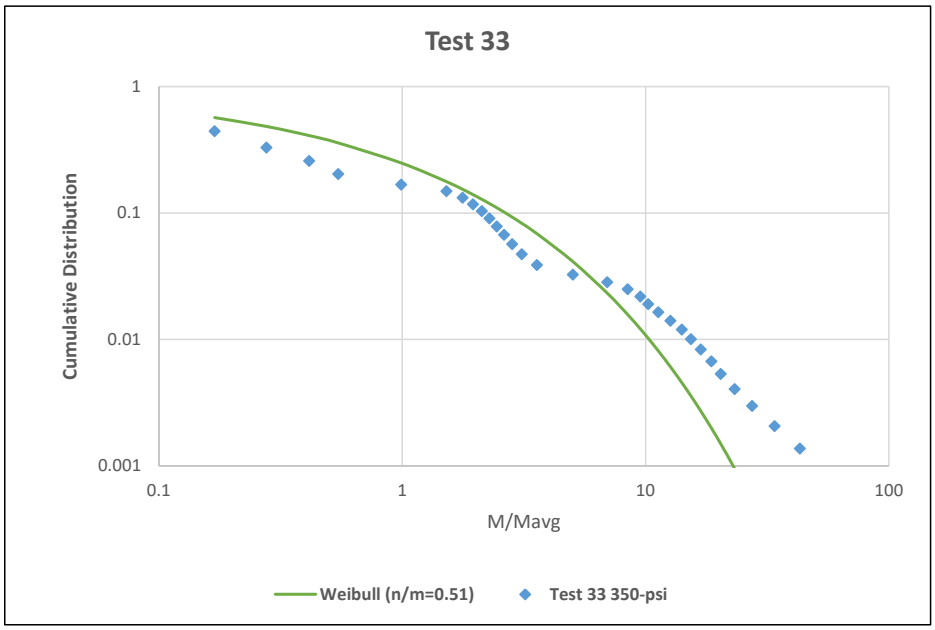

Figure 39. Best-fit Weibull mass distribution for physically-collected test data for PDF (top) and CDF (bottom) for Test 33 involving annealed glass.

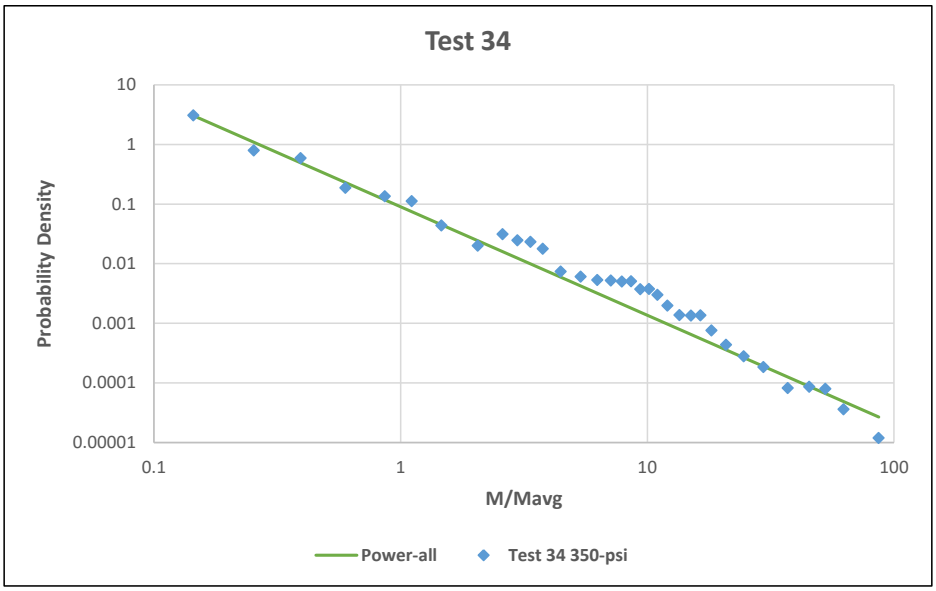

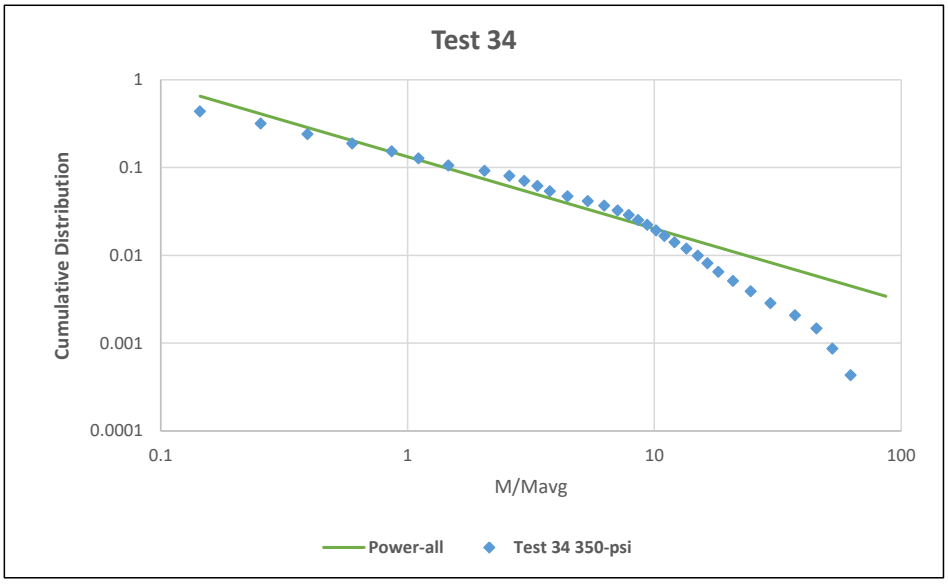

Figure 40. Best-fit power law mass distribution for physically-collected test data for PDF (top) and CDF (bottom) for Test 34 involving annealed glass

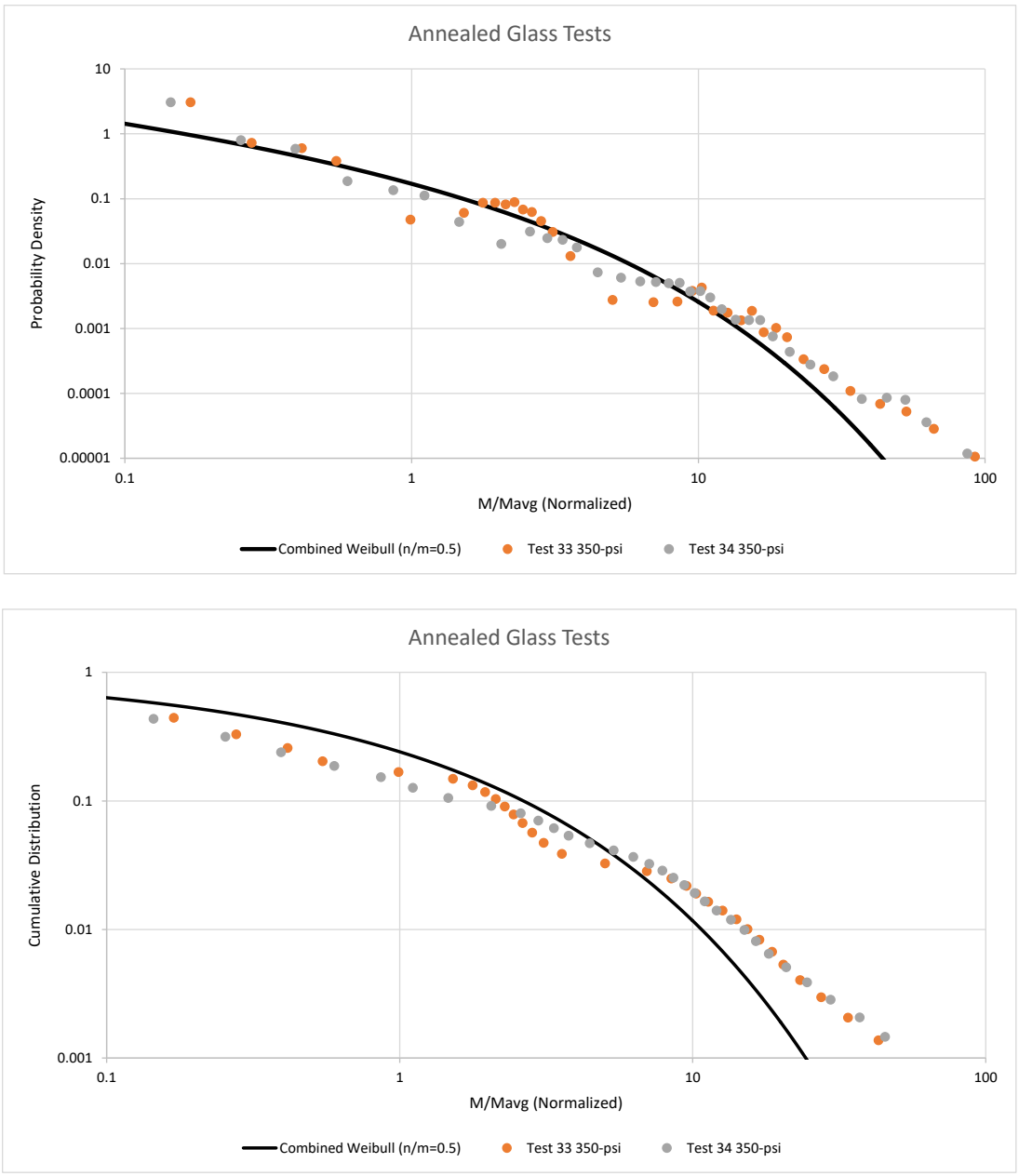

Figure 41. Best-fit Weibull mass distribution for physically-collected test data for PDF (top) and CDF (bottom) for Tests 33 and 34 involving annealed glass.

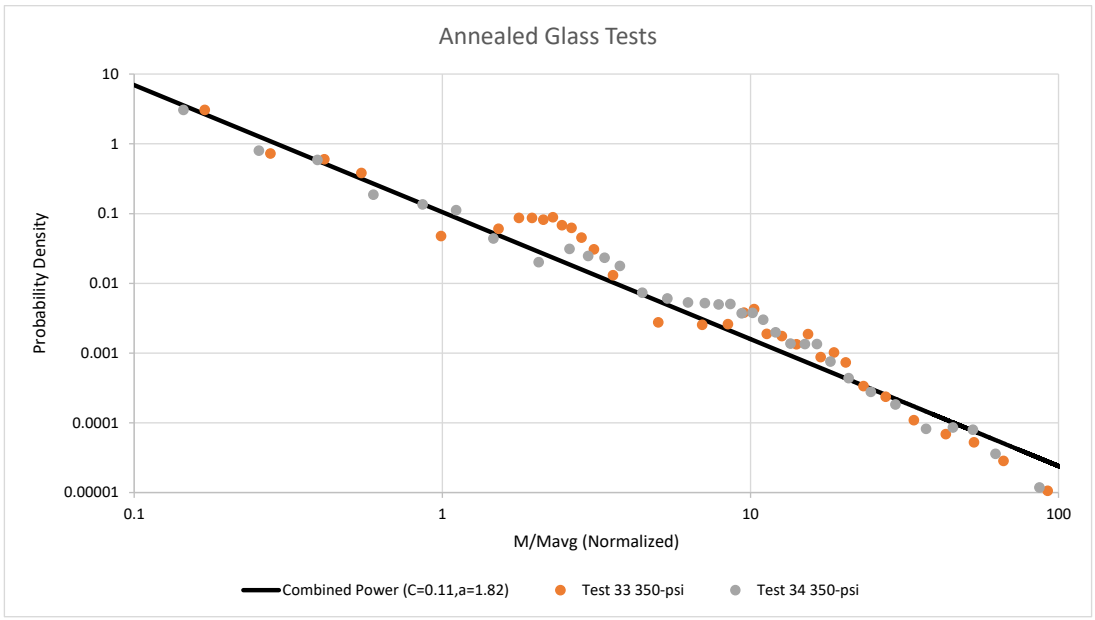

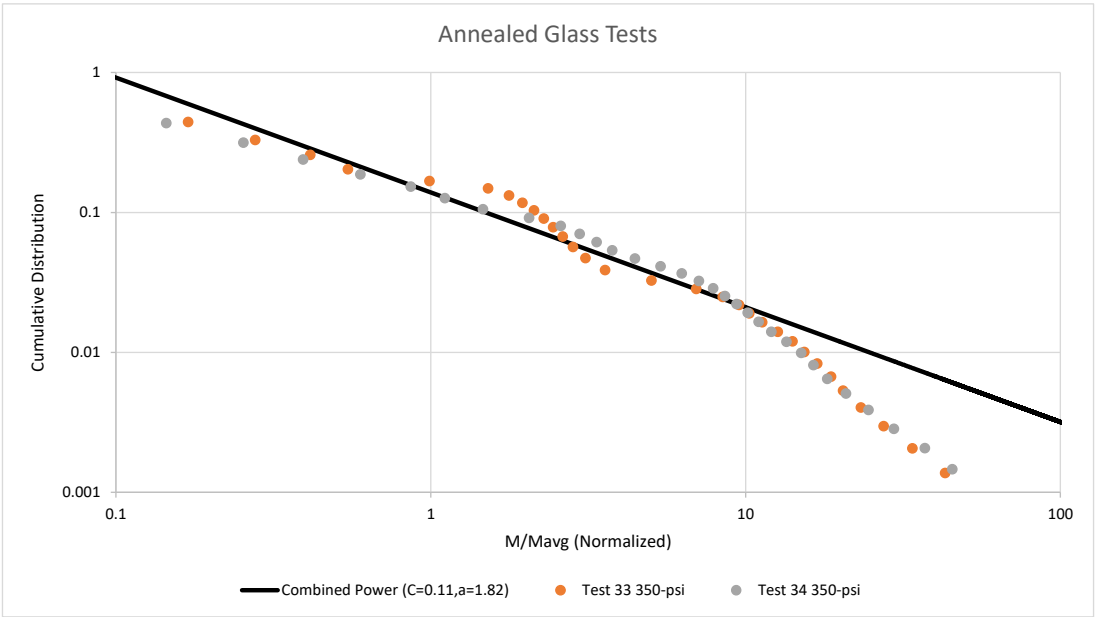

Figure 42. Best-fit power law mass distribution for physically-collected test data for PDF (top) and CDF (bottom) for Tests 33 and 34 involving annealed glass.

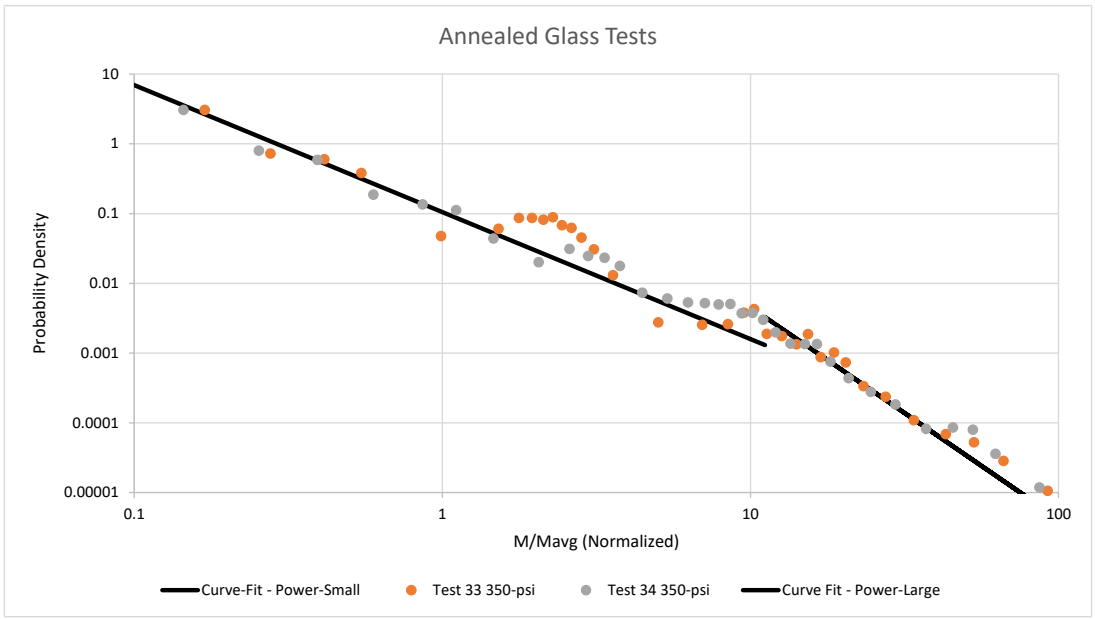

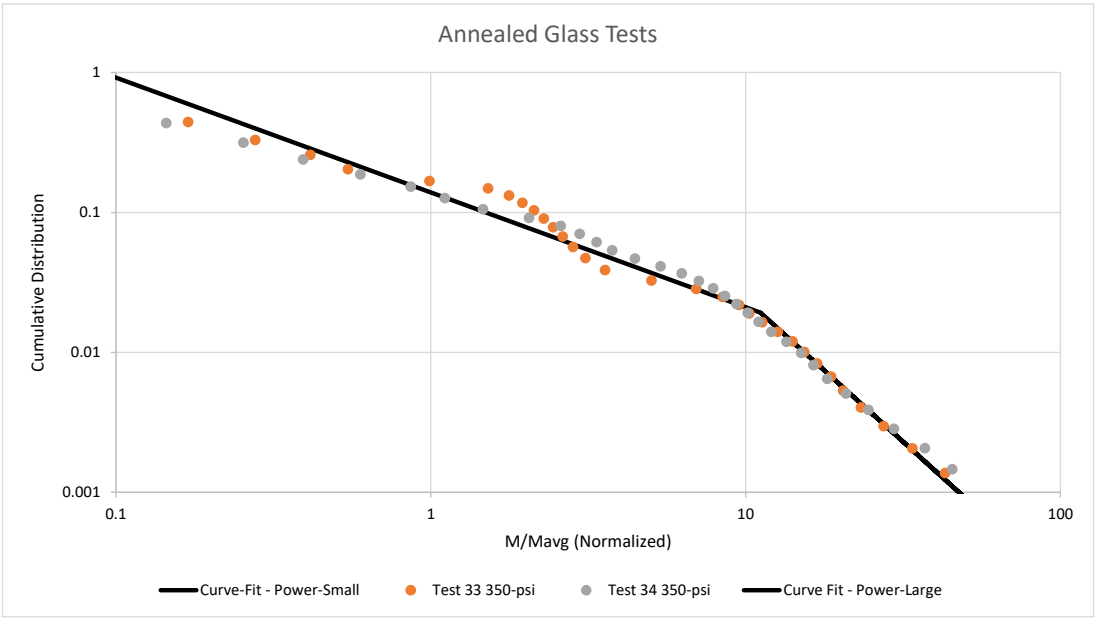

Figure 43. Best-fit bi-linear power law mass distribution for physically-collected test data for PDF (top) and CDF (bottom) for Tests 33 and 34 involving annealed glass.

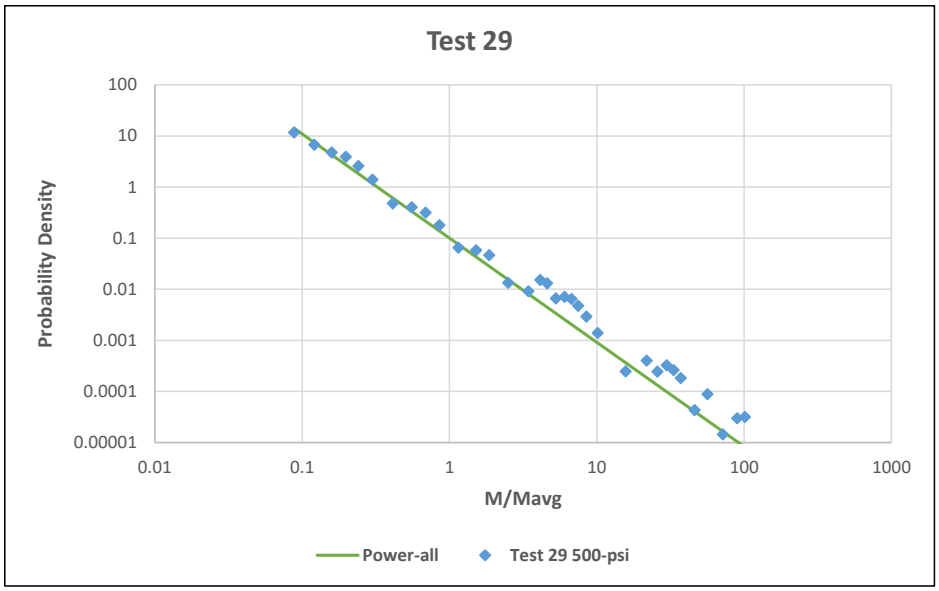

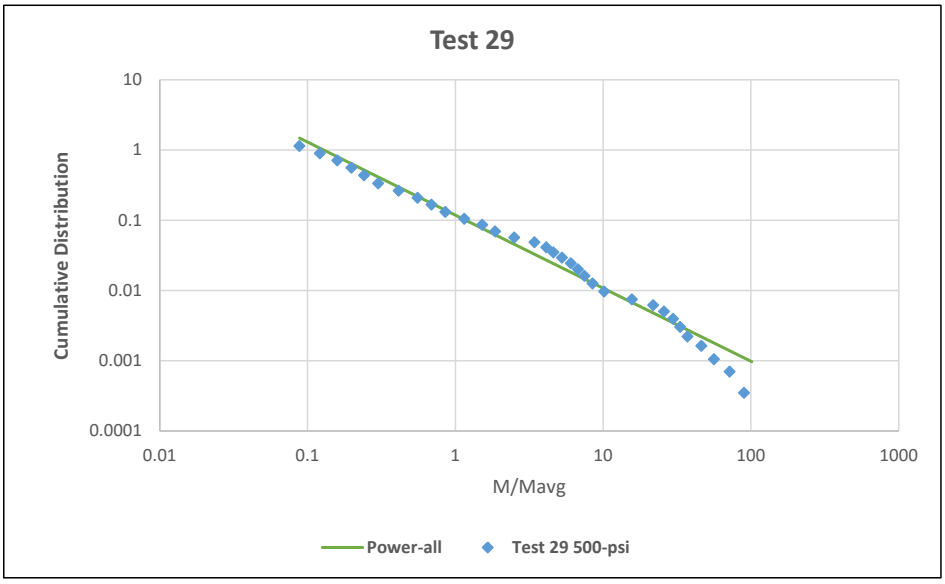

Figure 44. Best-fit power law mass distribution for physically-collected test data for PDF (top) and CDF (bottom) for Test 29 involving concrete.

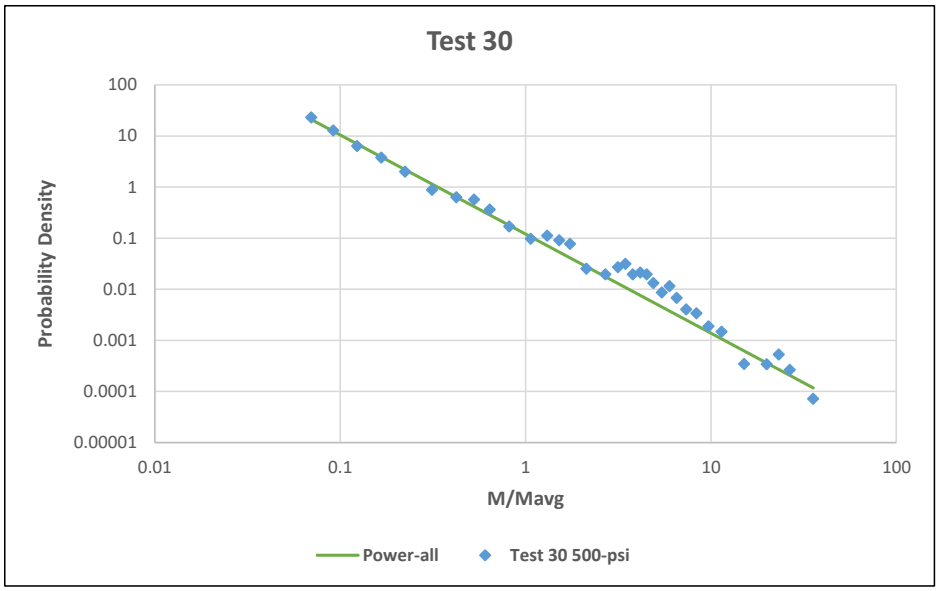

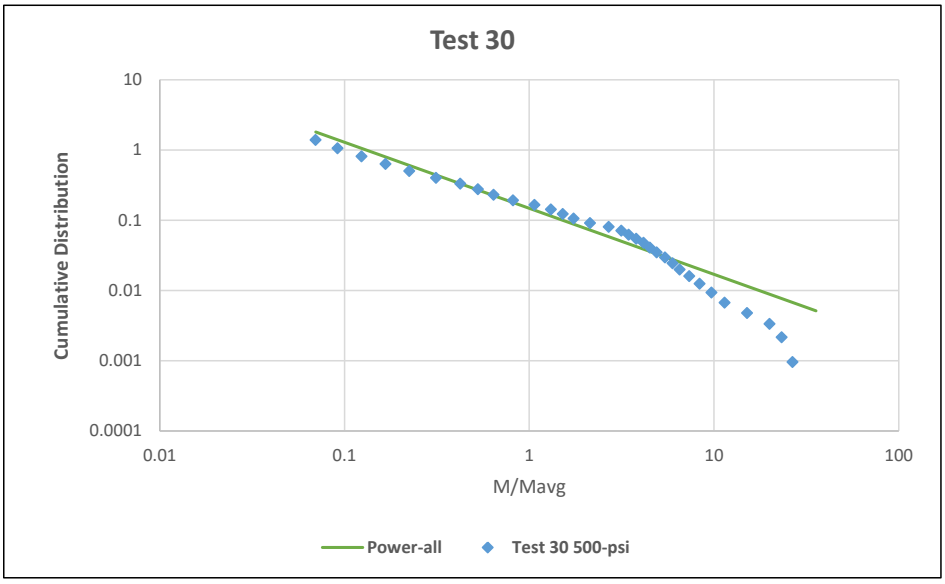

Figure 45. Best-fit power law mass distribution for physically-collected test data for PDF (top) and CDF (bottom) for Test 30 involving concrete.

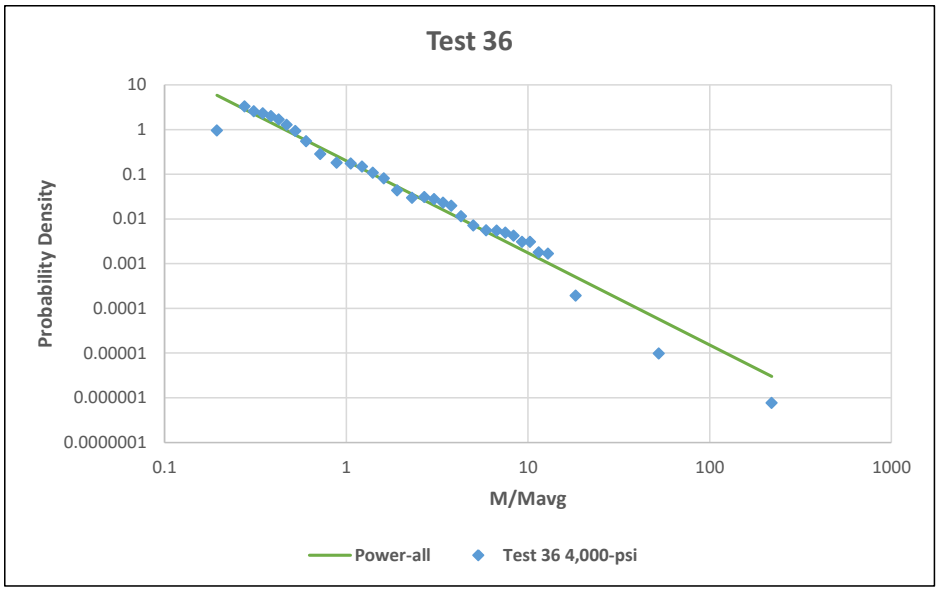

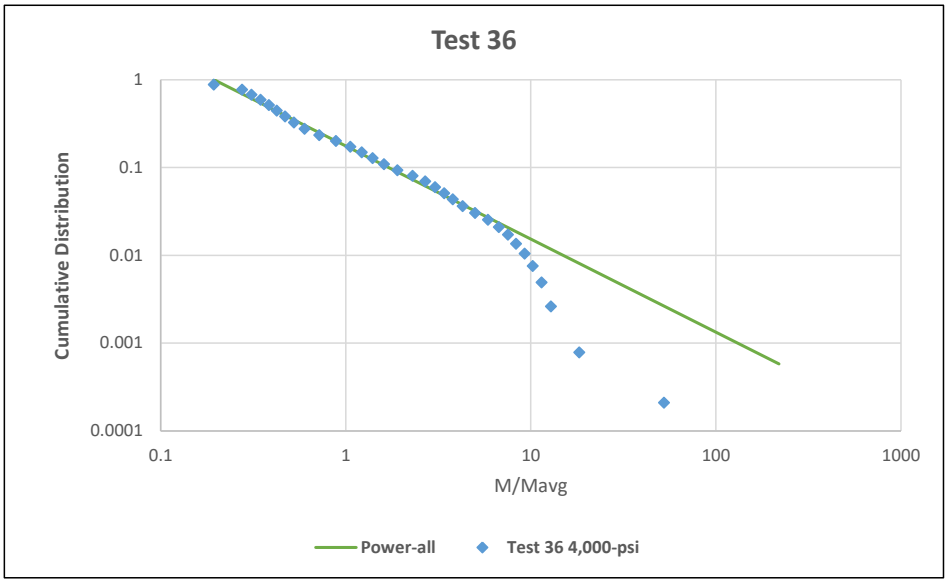

Figure 46. Best-fit power law mass distribution for physically-collected test data for PDF (top) and CDF (bottom) for Test 36 involving concrete.

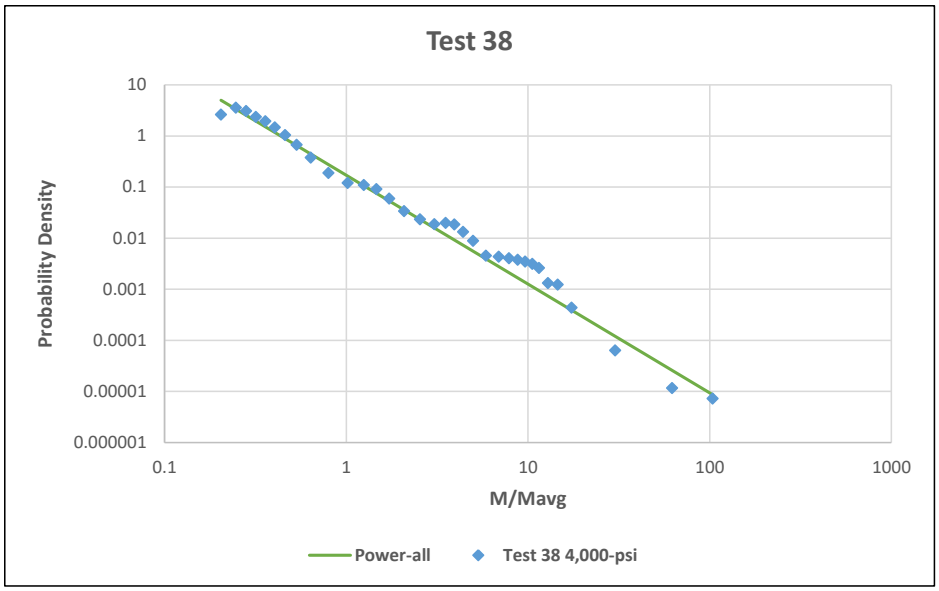

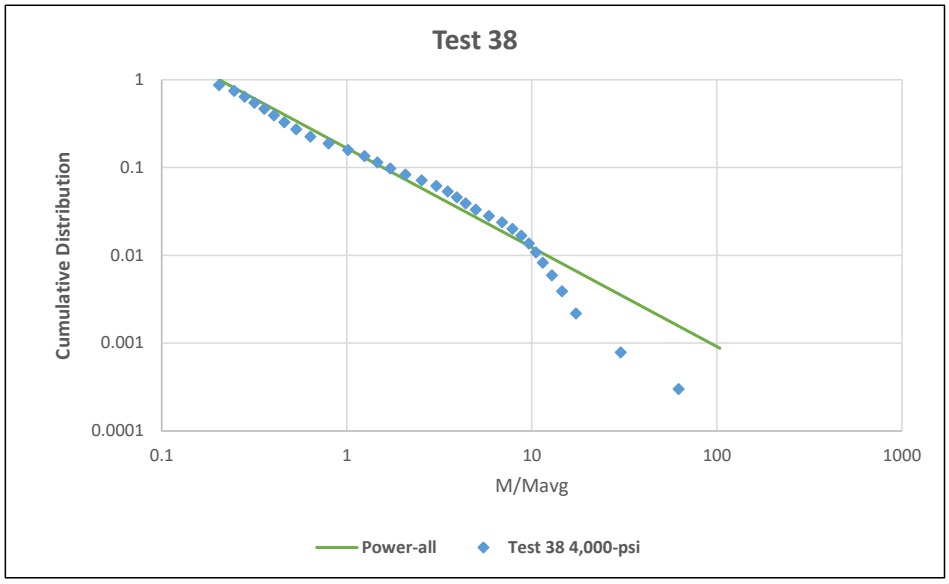

Figure 47. Best-fit power law mass distribution for physically-collected test data for PDF (top) and CDF (bottom) for Test 38 involving concrete.

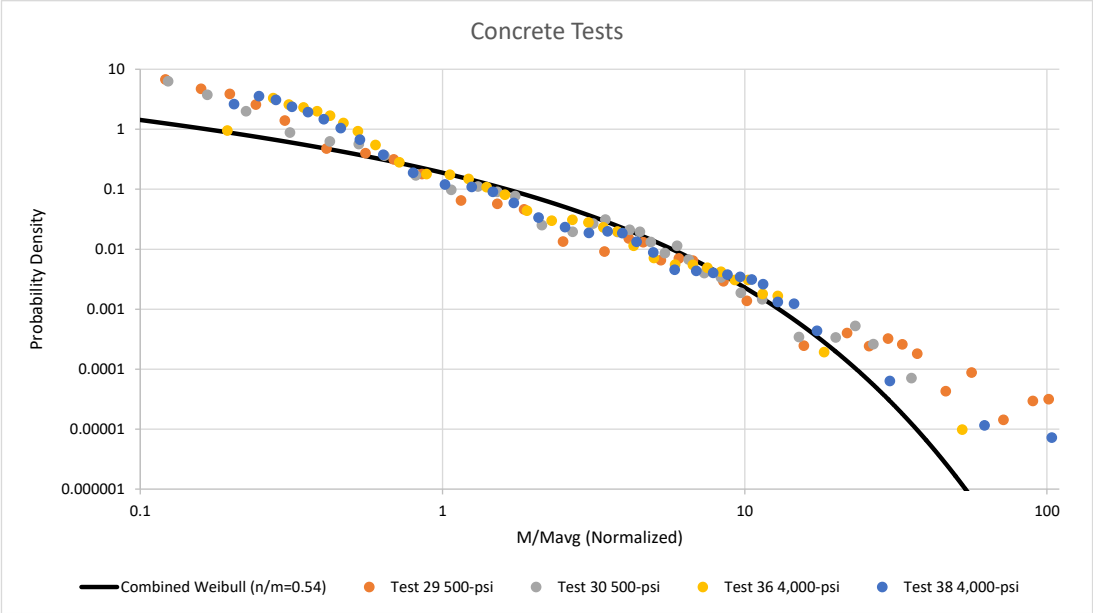

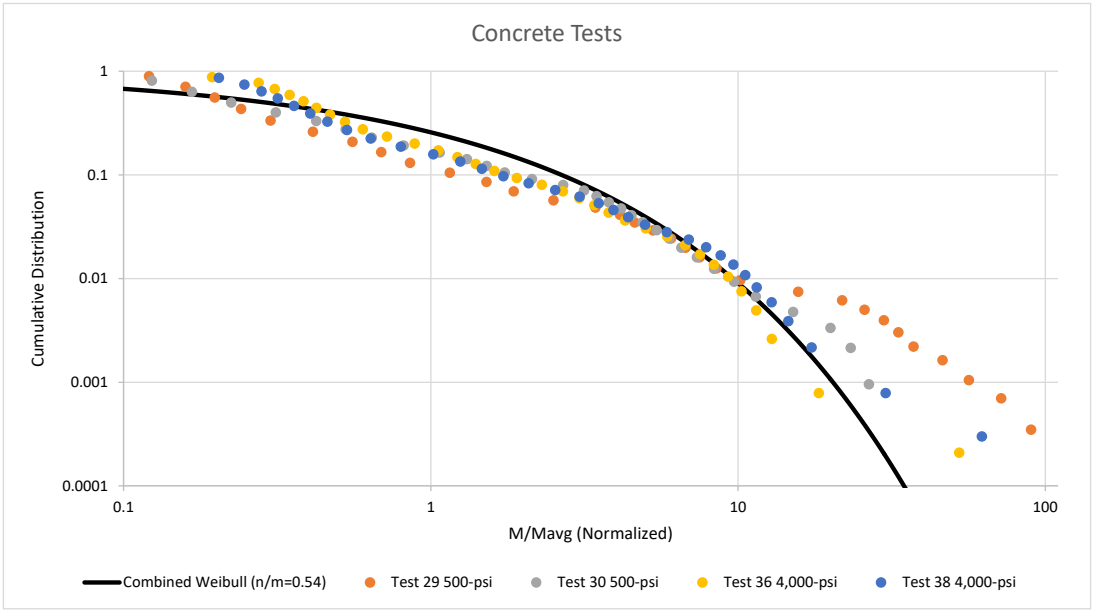

Figure 48. Best-fit Weibull mass distribution for physically-collected test data for PDF (top) and CDF (bottom) for Tests 29, 30, 36 and 38 involving concrete.

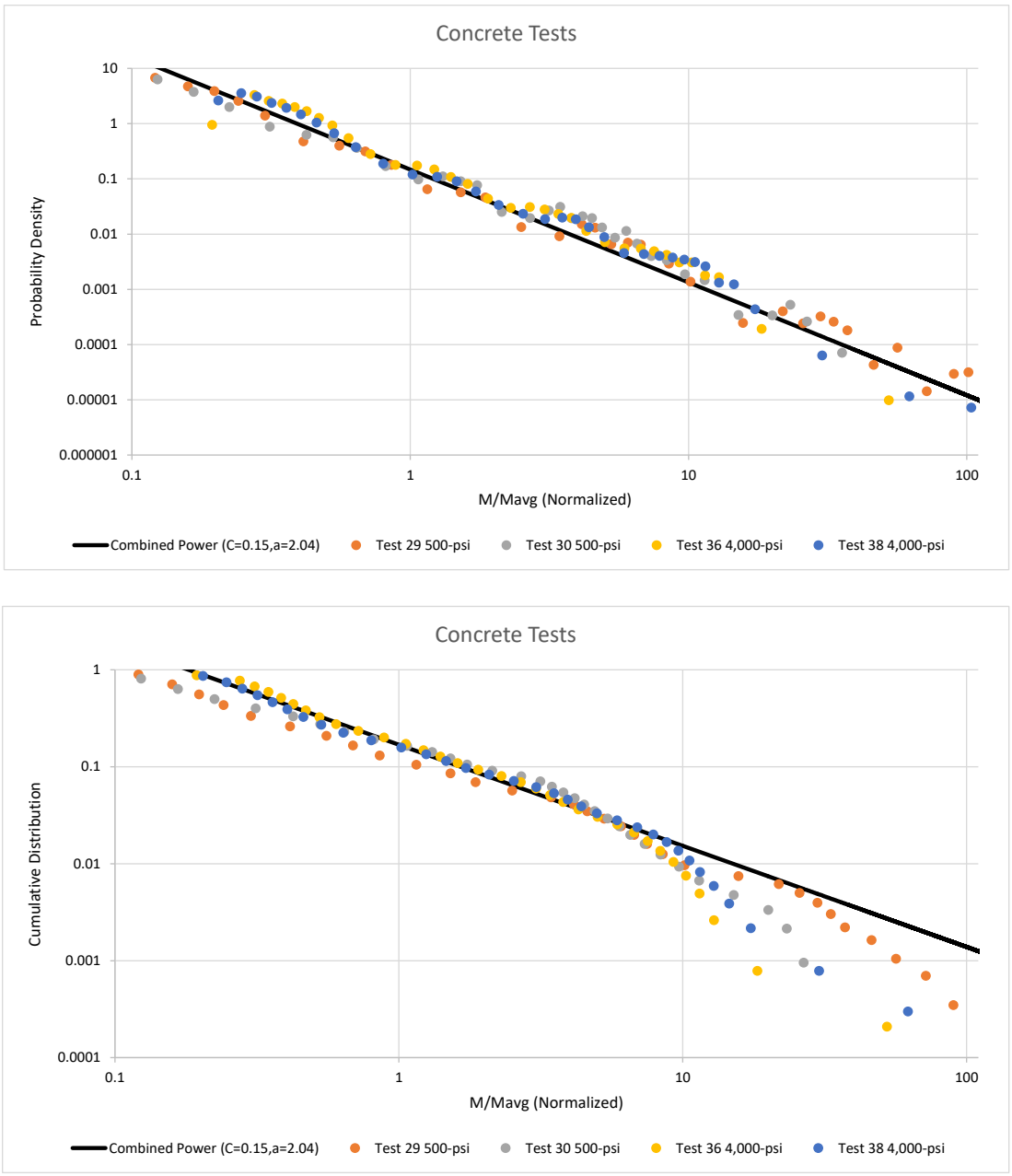

Figure 49. Best-fit power law mass distribution for physically-collected test data for PDF (top) and CDF (bottom) for Tests 29, 30, 36 and 38 involving concrete.

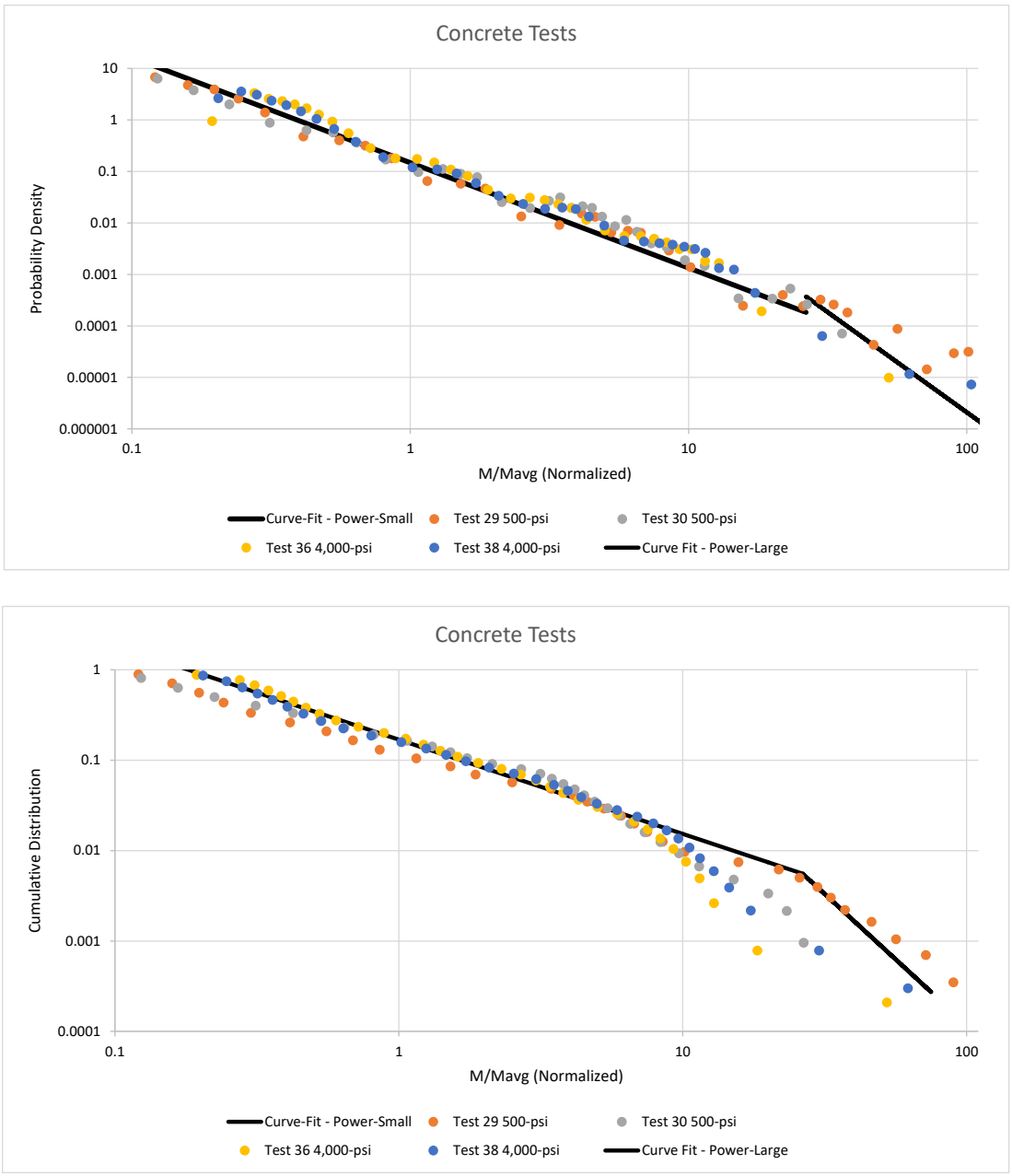

Figure 50. Best-fit bi-linear power law mass distribution for physically-collected test data for PDF (top) and CDF (bottom) for Tests 29, 30, 36 and 38 involving concrete.

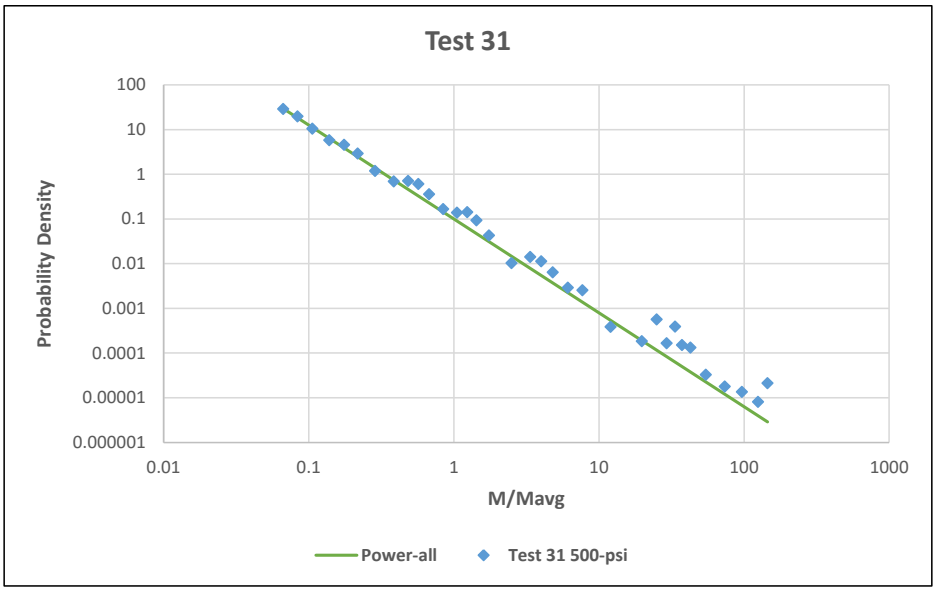

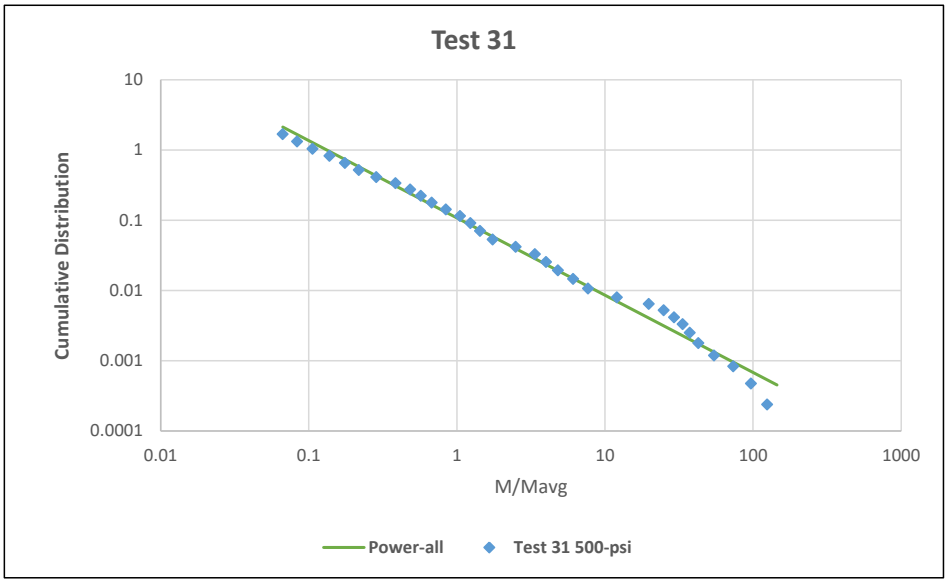

Figure 51. Best-fit power law mass distribution for physically-collected test data for PDF (top) and CDF (bottom) for Test 31 involving CMU.

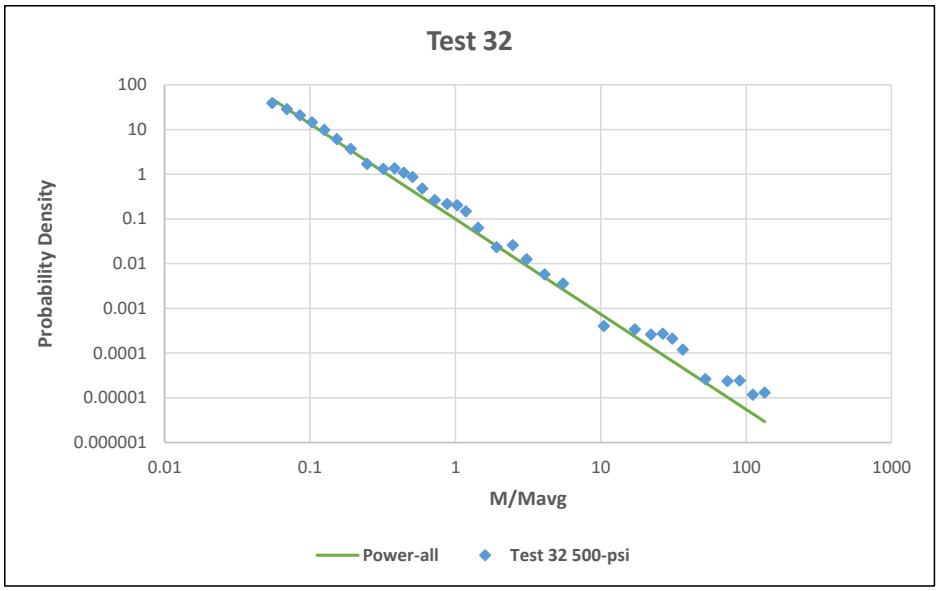

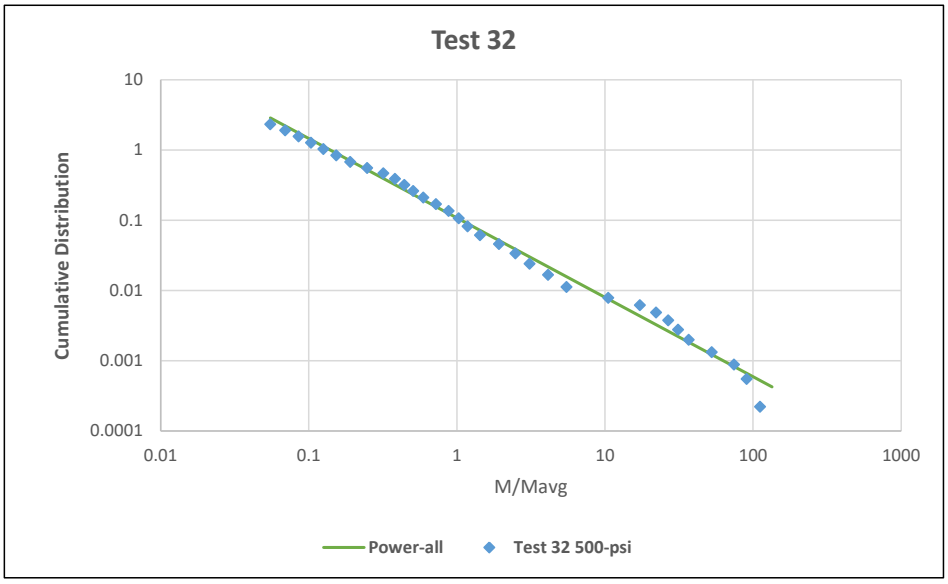

Figure 52. Best-fit power law mass distribution for physically-collected test data for PDF (top) and CDF (bottom) for Test 32 involving CMU.

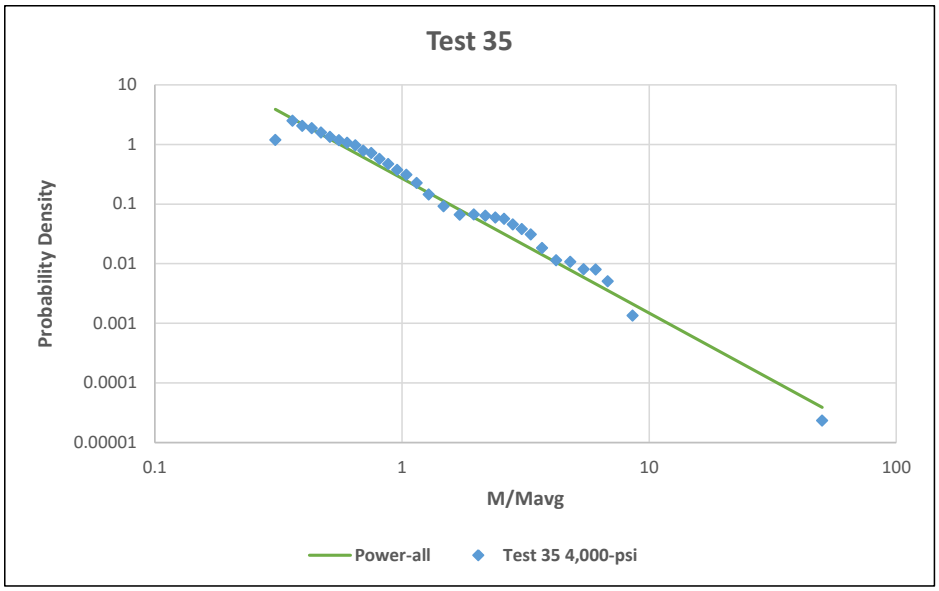

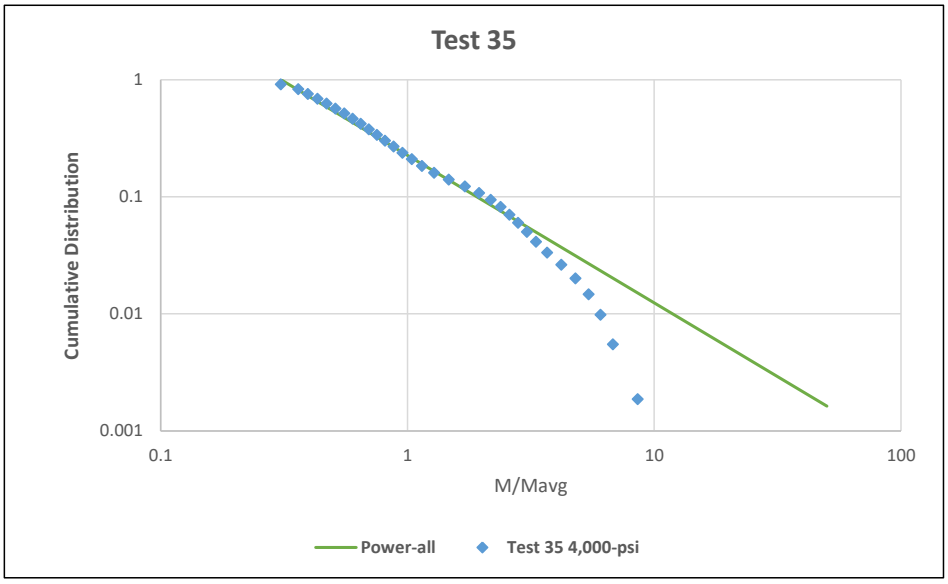

Figure 53. Best-fit power law mass distribution for physically-collected test data for PDF (top) and CDF (bottom) for Test 35 involving CMU.

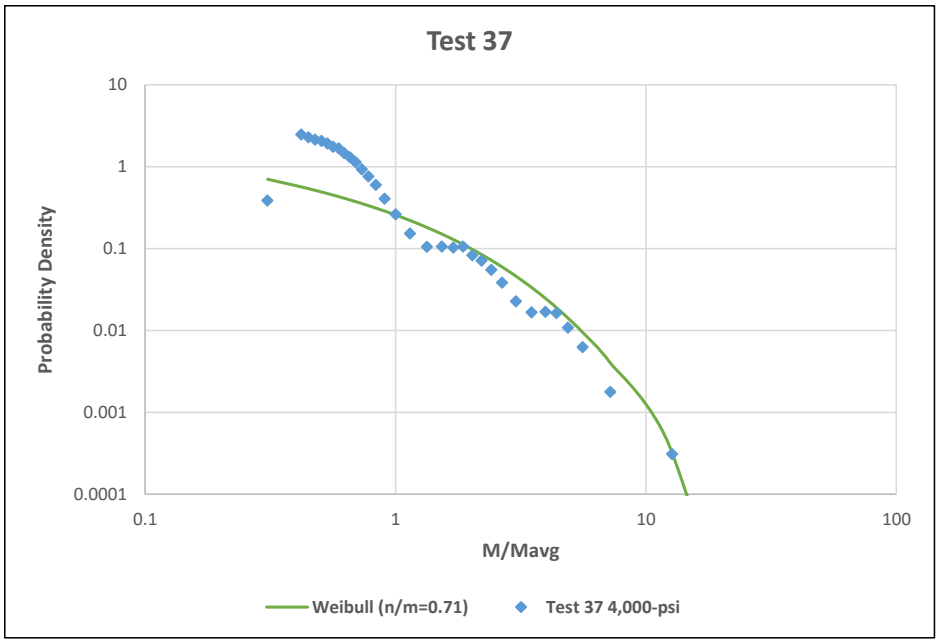

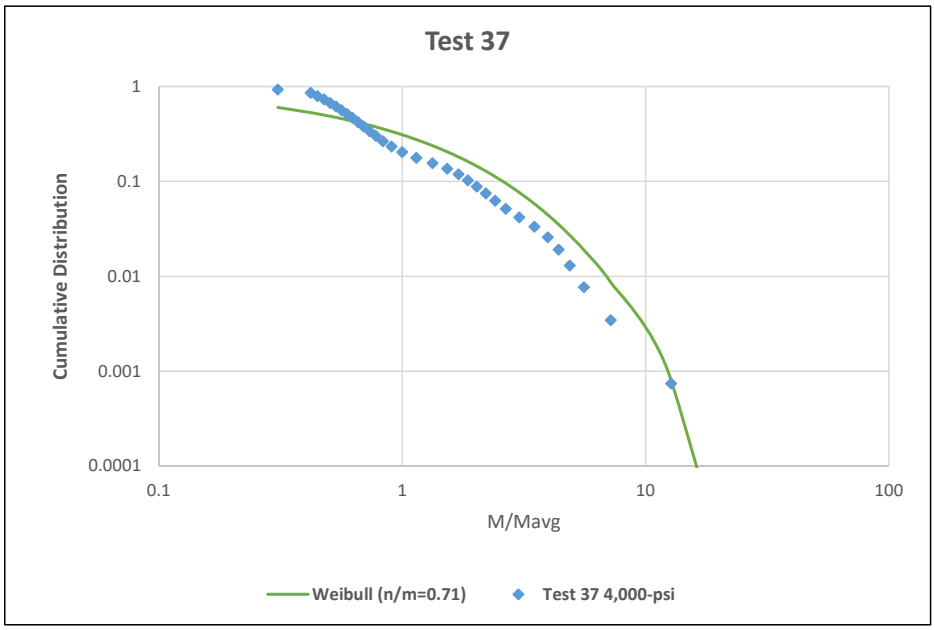

Figure 54. Best-fit Weibull mass distribution for physically-collected test data for PDF (top) and CDF (bottom) for Test 37 involving CMU.

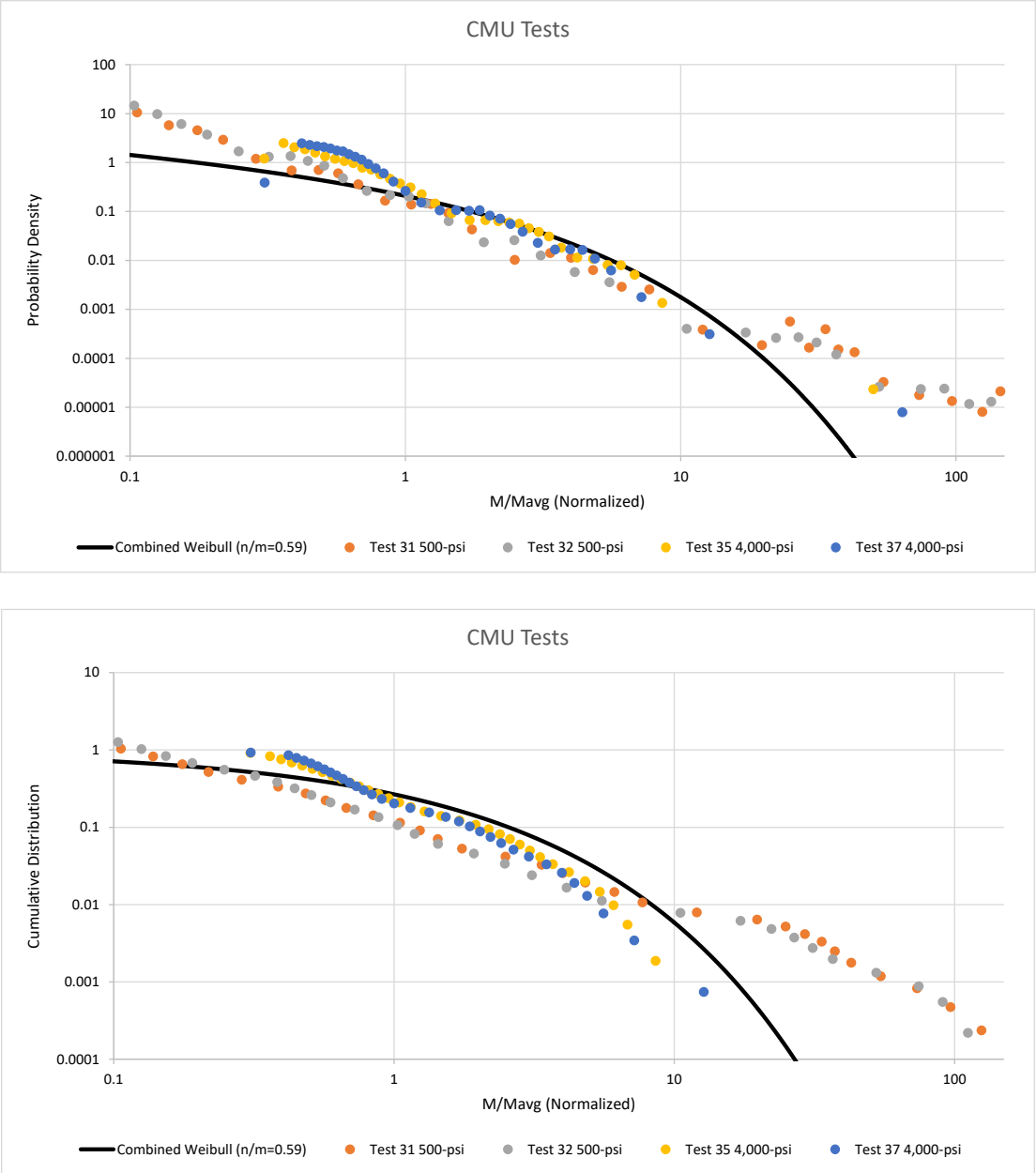

Figure 55. Best-fit Weibull mass distribution for physically-collected test data for PDF (top) and CDF (bottom) for Tests 31, 32, 35, and 37 involving CMU.

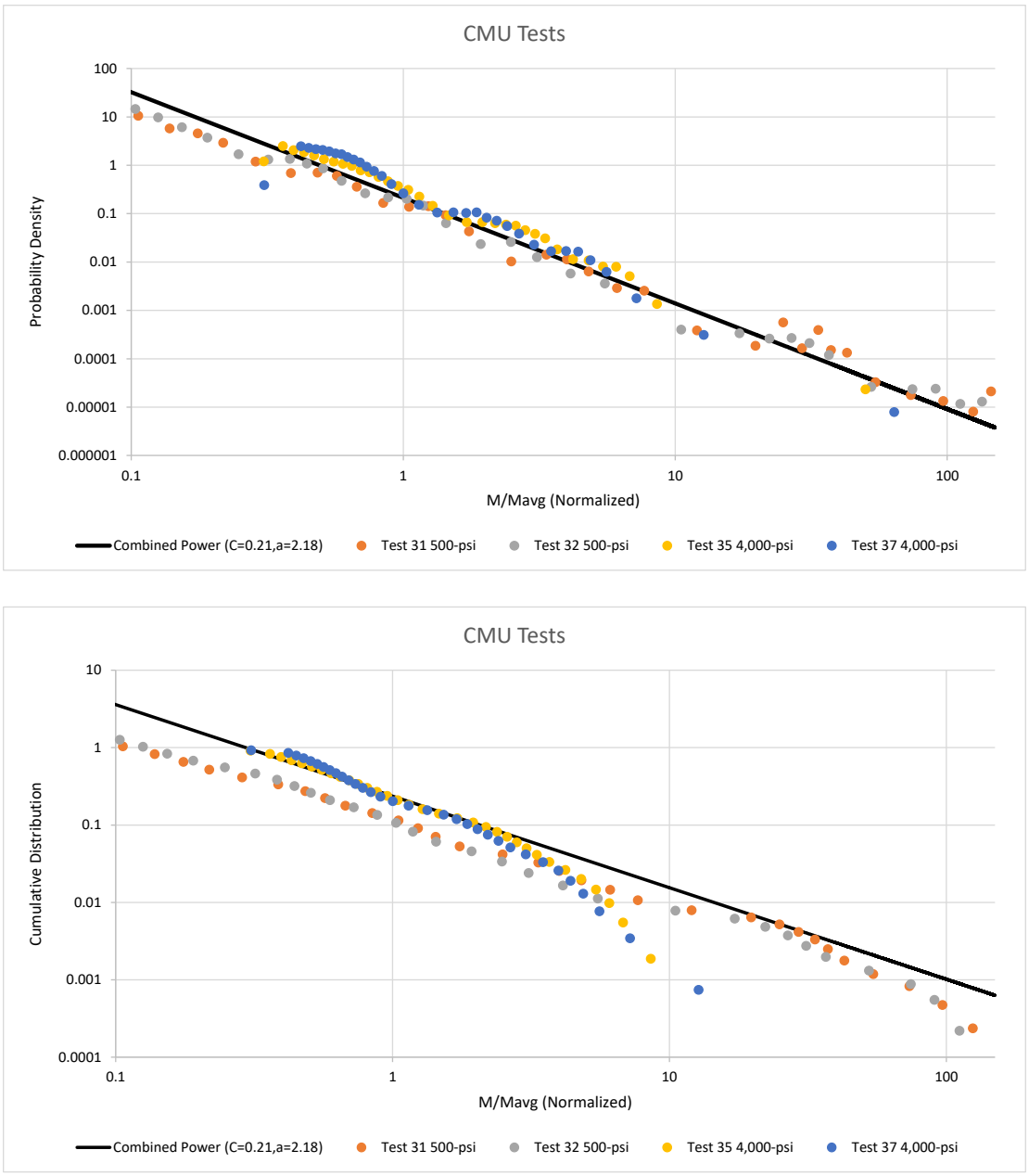

Figure 56. Best-fit power law mass distribution for physically-collected test data for PDF (top) and CDF (bottom) for Tests 31, 32, 35, and 37 involving CMU.

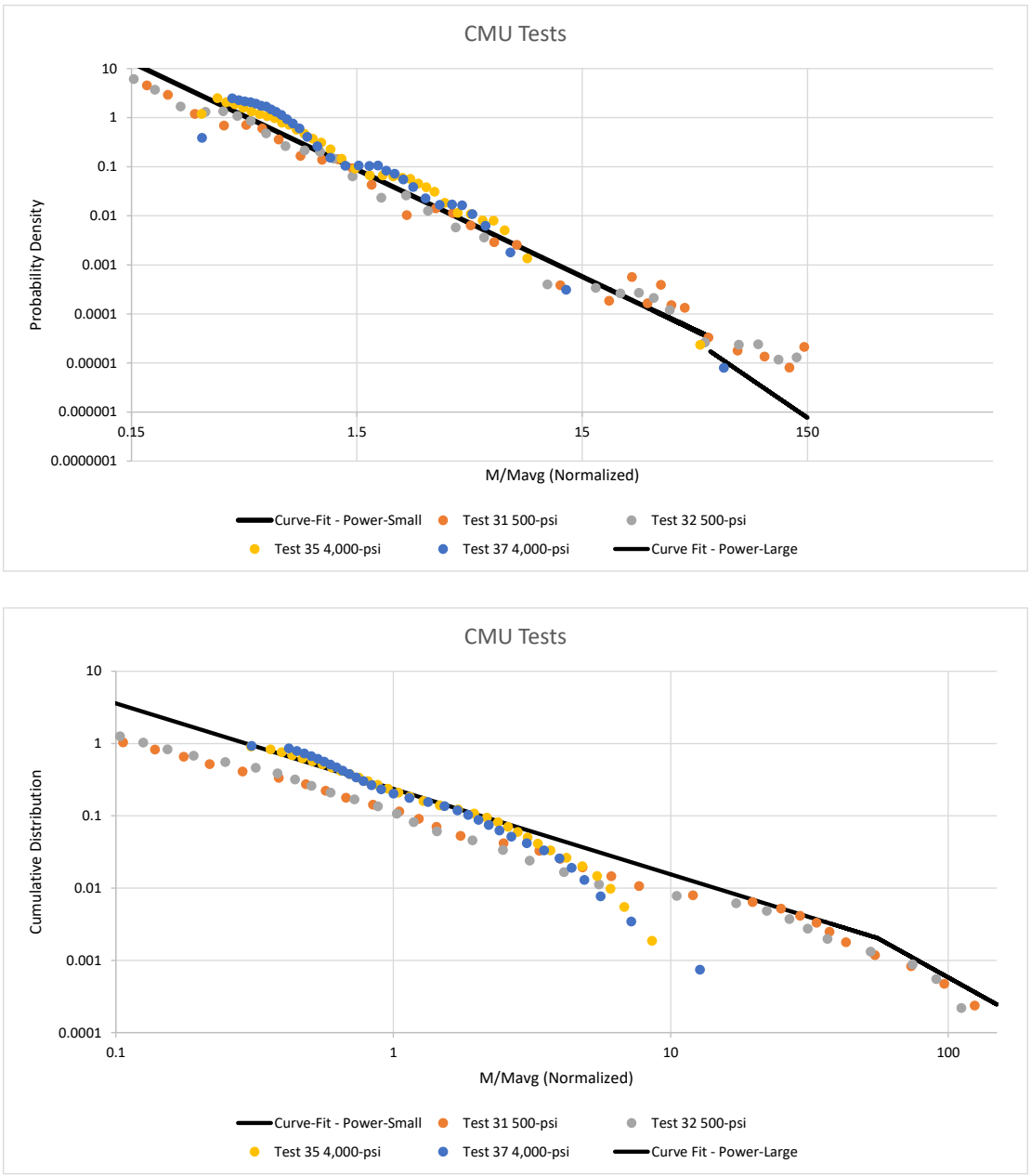

Figure 57. Best-fit bi-linear power law mass distribution for physically-collected test data for PDF (top) and CDF (bottom) for Tests 31, 32, 35, and 37 involving CMU.

For all tests, CDF and PDF distributions were fitted using Weibull and power law distributions; in most cases, piecewise (bi-linear) power law distributions were also attempted. For the Weibull fits, a $\chi 2$ approach was used to generate a single best fir (n/m) for both PDFs and CDFs. For the power law fits, CDFs were fit first using $\chi 2$, then PDFs were fit.

Figure 56, Figure 55, and Figure 57 show the best-fit power law, Weibull and bi-linear power law mass distributions, respectively, for the combination of the four tests involving CMU (Tests 31, 32, 35, and 37). Similarly, Figure 36, Figure 37, and Figure 38 show the best-fit Weibull, power law, and bi-linear power law mass distributions, respectively, for the combination of the five tests

involving tempered glass (Tests 22-25 and Test 39). Finally, Figure 42, Figure 41, and Figure 43 show the best-fit power law, Weibull and bi-linear power law mass distributions, respectively, for the combination of the four tests involving concrete (Tests 29, 30, 36 and 38).

Figure 49 through Figure 35 show the PDFs and CDFs for the individual tests. In each case, the best fit – either a power law or Weibull– is shown. show the fitting parameters.

shows the statistical parameters for each test. Peak reflected pressure values for the tests are included in show the fitting parameters.

for reference in the results discussion below. Table 8 and **Error! Reference source not found.** show the fitting parameters.

5 CONCLUSIONS

Table 9 summarizes the fragment size distributions obtained in Test Series 1 and 3. Notice that, in most cases, the Weibull and power law exponents appear to obtain rational values such as $\pm 2/3$, $\pm 5/6$, ± 1, and $\pm 7/6$. This is consistent with a large body of previous experimental and theoretical results; see, e.g. [5].

Table 9. Summary of fragment size distributions obtained in Test Series 1 and 3. Based on Table 8.

	Initial (Rear-View HSV)	**Final (Physical Collection)**	**Description**
Tempered Glass: Case 1	Weibull $r = 0.66 \pm 0.03$	Weibull $r = 0.66 \pm 0.03$	Below 500 psi peak reflected static overpressure. With or without stripper.
Tempered Glass: Case 2	*(not measured)*	Power Law $r = -1.08 \pm 0.06$	Above 1,900 psi peak reflected static overpressure. No stripper present.
Annealed Glass: Case 1 *(no Case 2)*	Weibull $r = 0.66 \pm 0.03$	Power Law $r = -0.83 \pm 0.02$	Below 500 psi peak reflected static overpressure. No stripper present.
Concrete: Case 1	*(not measured)*	Weibull $r = 0.66 \pm 0.03$	Stripper present. Does not depend on overpressure or sample thickness.
Concrete: Case 2	*(not measured)*	Power Law $r = -1.00 \pm 0.06$	No stripper present. Does not depend on overpressure or sample thickness.
CMU: Case 1	*(not measured)*	Weibull $r = 0.66 \pm 0.04$	Stripper present. Does not depend on overpressure or sample thickness.
CMU: Case 2	*(not measured)*	Power Law $r = -1.17 \pm 0.08$	No stripper present. Does not depend on overpressure or sample thickness.

For fully-tempered glass at low (<500 psi) peak reflected static overpressures, the shape of the size distribution remains unchanged over time. However, for annealed glass at low (<500 psi) peak reflected static overpressures, the shape of the size distribution shifts from a Weibull to a power law size distribution. In either case, the average fragment size decreases by a factor of ~10 to 20. This implies that the original glass fragments break up due to factors such as: (a.) delayed response to the original insult; (b.) mid-air collisions with other glass fragments; (c.) ricochet collisions with ground; (d.) collisions with the soft-capture fragment collection device; and (e.) collisions with other glass fragments following capture in the fragment collection device. The weaker annealed glass fragments are more susceptible to all of these factors than the stronger tempered glass fragments. Similarly, the faster tempered glass fragments created by higher loads are more susceptible to all of these factors than the slower tempered glass fragments created by lower loads.

With the fragment stripper in place, the concrete and CMU test articles obtain essentially the same fragment size distributions as the tempered glass test articles, i.e., Weibull size distributions with $r \approx 2/3$ [1]. However, with the fragment stripper removed, the concrete and CMU test articles obtain substantially different fragment size distributions, i.e., power law size distributions with $r \geq 1$. This probably reflects the substantial increase in the volumetric density of fragments. Eliminating the stripper increases the captured fragment number and mass by factors of 5 to 15. The greater the volumetric density, the greater the chances of collisions between fragments. The brittle materials tested here are likely to sustain damage during the initial fragmentation event (e.g., cracks/splits, localized crumbling, macro- and microscopic defects) that make them susceptible to breakup during high-speed collisions, almost regardless of their original virgin strength.

Alternatively, this could reflect that fact that, without the stripper present, there tends to be a great mixture of fragments present. In other words, the test results may be affected by fragments formed from different parts of the test article, at different times, and an under different conditions. Reference [5] describes the possible effects of mixed populations on fragment size distributions. This is most likely a significant factor in the high-pressure (>1,900 psi) tempered glass tests but a minor factor in the other tests.

6 REFERENCES

[1] B. Bewick, G. Rolater, J. Bui, M. Barsotti, K. Marchand, A. Ziemba, M. Sanai and C. Laney, "Fragmentation of Solid Materials Using Shock Tubes. Part 1: First Test Series in a Small-Diameter Shock Tube," DTRA-TR-17-21, 2017.

[2] B. Bewick, G. Rolater, K. Marchand, A. Ziemba, M. Sanai and C. Laney, "Fragmentation of Solid Materials Using Shock Tubes. Part 2: First Test Series in a Large-Diameter Shock Tube," DTRA-TR-17-50, 2017.

[3] CR Laurence, [Online]. Available: www.crlaurence.com/adv/glass_and_glazing/index_us.html. [Accessed 15 October 2015].

[4] Jim's Glass Shop, [Online]. Available: http://www.jimsglass.biz/. [Accessed October 2015].

[5] C. B. Laney, "Effects of Mixtures on Liquid and Solid Fragment Size Distributions," DTRA-TR-16-52, May 2016.

APPENDIX A: PRE-TEST MODELING

In preparation for this test series, LS-DYNA simulations were performed to estimate experimental strain rates. The simulations of the concrete test articles assumed a 16-in. (406.4-mm) square plate with a 2-in (5-cm) thickness and a 3,500-psi (27.6-MPa) compressive strength. The simulations of the glass test articles assumed a 16-in. (406.4-mm) square plate with a 1/4-in. (6.3-mm) thickness. A load of 100-psi (68.9-kPa) to 72,000-psi (496-MPa) was applied to the interior surface of the plate.

Figure 58 shows the simulation setup used for the concrete test articles. Figure 59 shows a cross-sectional view of the damage progression. Finally, Figure 60 show a three-dimensional view of the final damage.

Figure 58. Illustration of as-modeled concrete test article in LS-DYNA.

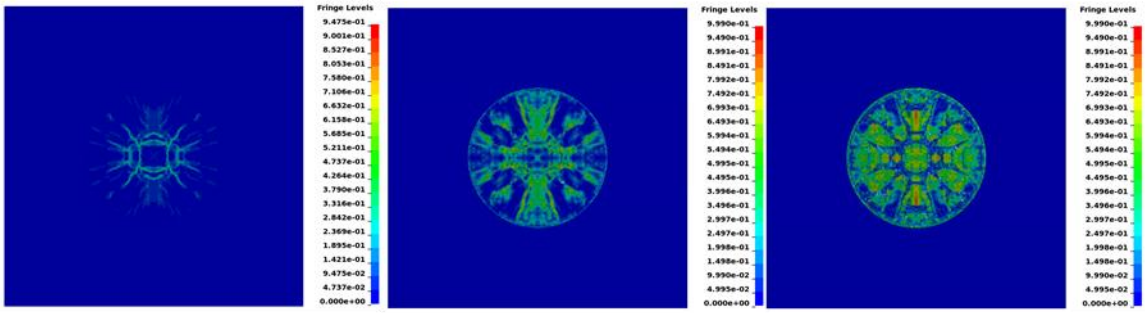

Figure 59. Progression of damage (1=fully damaged) to concrete sample in the LS-DYNA model.

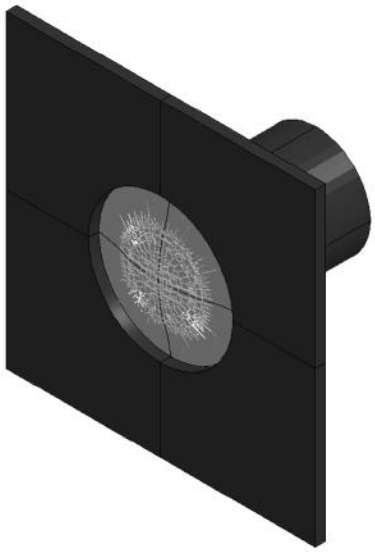

Figure 60. Visual of a damaged concrete sample in the LS-DYNA model.

For each simulation, an in-plane velocity gradient was used to determine an average strain rate through the thickness of the plate. The velocity gradient was taken over a 2-in. radius at the rear face, middle of the sample, and at the front face of the sample. The results were tabulated and plotted. The results show that the strain rates range from 10^2 up to 10^4 /s, a difference of two orders of magnitude.

APPENDIX B: CONCRETE AND MASONRY COMPRESSIVE STRENGTHS

WALLACE-KUHL & ASSOCIATES
3050 Industrial Boulevard
West Sacramento, CA 95691
Phone: (916) 372-4100
Fax: (916) 372-9065

COMPRESSION TEST REPORT

Report to: JUST AWESOME CONCRETE
ATTN: VIA EMAIL: JULIO LAGHARDIA

Date: 6/12/15

WKA Project No.: 8300.82

Project Name: 4034 W. GRANTLINE ROAD
TRACY, CA

Mix Design No.: HIGH STR. CONCRETE

Supplier: SAKRETE

Design Strength: 3,500 psi
Design Age: 28 days
Specimen: CONCRETE
Air Content:

Location in Structure:
TRIAL BATCH

Mix Temp. 59 °F Air Temp. 52 °F Measured Slump: 3.5 in.

SPECIMEN LAB NO.	64563	64564	64565
Date Cast	5/14/15	5/14/15	5/14/15
Date Received	5/15/15	5/15/15	5/15/15
Date Tested	5/21/15	5/28/15	6/11/15
Age at Test, days	7	14	28
Diameter, in.	4.00	4.00	4.00
Height, in.	8.0	8.0	8.0
Area, sq. inches	12.57	12.57	12.57
Ult. Load, lbs.	32905	41200	60630
Comp. Str., psi	2620	3280	4820
Fracture Type	2	3	3

Average strength: 4820 psi at 28 days

[X] Meets 28 day strength req. [ ] Fails to Meet 28 day str. req. [ ] No strength req. given [X] Cast by WKA [ ] Cast by others

Remarks: TEST AGES AND QUANTITY OF SPECIMENS DETERMINED BY JUST AWESOME CONCRETE

TYPES OF FRACTURE

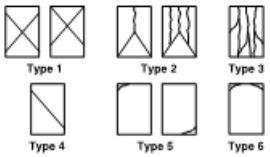

Copies to:

Reviewed by: DTH
David T. Hunn

TEST METHODS: Compressive Strength - ASTM C39, Slump - ASTM C 143, Mix Temp - ASTM C1064, Air Content - ASTM C173 or C231, Unbonded Caps - ASTM C1231

CAPITOL ENGINEERING LABORATORIES, INC.
Materials Testing • Inspection • Crane Certification

October 17, 2014
File No. 5710
Lab No. 603-1276G

Lance Vasquez
Basalite Concrete Products
605 Industrial Way
Dixon, CA 95620

Project: Q. C. Testing

Subject: ASTM C90 Testing of 09/24/14

Dear Lance,

The following is a summary of results obtained from samples received in our lab and tested beginning on 09/22/14. Testing was conducted in accordance with ASTM C140 and C426.

Unit Description:	725		
Test Date:	09/24/14		
Results:			C90 Spec
Absorption (pcf):	9.7/9.1/8.4	AVG = 9.1	13 max
Unit Weight (pcf):	128.3/129.8/131.5	AVG = 129.8	Normal Wt
Moisture Content (%):	10/11/11	AVG = 11	N/A
Compressive Strength – Coupons (PSI):	3700/4060/3730	AVG = 3830	2000 min
Linear Shrinkage (%):	0.048/0.047/0.048	AVG = 0.048	0.065 max

In summary, the specimens tested conform with ASTM C90 for the tests performed.

Respectfully submitted,

CAPITOL ENGINEERING LABORATORIES, INC.

G. Barry Lotz, C.E.

REGISTERED PROFESSIONAL ENGINEER G. BARRY LOTZ No. 33269 Exp 04/30/16 CIVIL STATE OF CALIFORNIA

101714.2538/kv

631 Commerce Drive, #200 • Roseville, CA 95678 • (916) 786-2488 • FAX (916) 786-9372
www.capitolengineeringlab.com • capeng@capitolengineeringlab.com